SEISMIC-STYLE PROCESSING OF NUMERICAL EM DATA

A Thesis Presented to

the Faculty of the Department of Earth and Atmospheric Sciences

University of Houston

In Partial Fulfillment

of the Requirements for the Degree

Master of Science

By

John W. Neese

May 2015

SEISMIC-STYLE PROCESSING OF NUMERICAL EM DATA

_____

John W. Neese

APPROVED:

_____

Dr. John P. Castagna, Chairman

_____

Dr. Evgeny Chesnokov, EAS Department

_____

Dr. David R. Jackson, ECE Department

_____

Dr. Leon Thomsen, EAS Department

_____

Dean, College of Natural Sciences and Mathematics

ACKNOWLEDGEMENTS

This thesis is the inspiration of Dr. Leon Thomsen, and the result of his tireless patience and encouragement. My gratitude goes to Dr. John P. Castagna for acting as my thesis advisor, for sticking up for me at critical junctures, and for numerous enlightening suggestions. I thank Dr. Evgeny Chesnokov for his demanding and penetrating questions. Finally, I am forever indebted to Dr. David R. Jackson from the Department of Electrical and Computer Engineering for devoting many more hours than I deserved to bring me up to speed on electromagnetics.

SEISMIC-STYLE PROCESSING OF NUMERICAL EM DATA

An Abstract of a Thesis

Presented to

the Faculty of the Department of Earth and Atmospheric Sciences

University of Houston

In Partial Fulfillment

of the Requirements for the Degree

Master of Science

By

John W. Neese

May 2015

ABSTRACT

Standard seismic-processing methods are applied to numerical simulations for several variations of a standard 1-D numerical CSEM model, calculated using seismic-style acquisition parameters: an impulsive source and many receivers, unaliased. The data are normalized to unit maximum amplitude at each offset, making the weak far-offset signal visible (seismic-style) without computation of apparent resistivity (EM-style). Hence, the amplitudes are not appropriate for inversion (EM-style), but the moveout is interpretable (seismic-style) for the presence of a reservoir layer.

Plots of normalized data exhibit distinctive moveout, similar to seismic data, but with significant dispersion. The dominant moveout is shown to be linear at a given frequency, consistent with theoretical expectation for lateral (head) waves. Conventional (semblance) velocity analyses and stacking detects a 100 Ωm reservoir on the basis of its linear moveout, but does not appear to be useful for picking stacking velocities. Standard *f-k* transforming and filtering does not appear to be promising. Linear Radon transforms also detect the reservoir.

Standard seismic processing methods are modified to account for the strong frequency-dependence of the EM data, in order to focus on the resistivity. Moveout as a function of frequency is replaced by moveout as a function of resistivity. A resistivity moveout correction is defined that indicates the existence of the reservoir, and estimates its effective resistivity. Similarly, a modified Radon transform ("EM-Radon") is defined which also indicates reservoir existence and effective resistivity. EM-Radon is shown to be robust to noise, and to decimation of the receivers, and of the time-sampling. EM-Radon's sensitivity is explored to depth, thickness, and resistivity of the reservoir; T-equivalence is confirmed.

These calculations demonstrate that, in simple cases, numerical CSEM data, appropriately acquired, and processed seismic-style, can be interpreted for subsurface effective resistivity.

CONTENTS

LIST OF FIGURES

LIST OF TABLES

1 Introduction

1.1 Deep connection between EM and seismology

Thomsen *et al.* (2007, 2009), Strack *et al.* (2008), and Thomsen (2014) lay out the case for the deep connection between EM and seismology. Thomsen (2014) is the inspiration for this thesis.

The deep connection arises in part because of similarities between the partial differential equations governing the two physical phenomena, and their plane-wave solutions, and in part because of surprising similarities in the wavenumbers parameterizing these solutions. This section explains the motivation of the first part in terms of the choices made by exploration geophysicists.

For seismic exploration, due to weak frequency dependence in the relatively narrow seismic frequency band (say, 10 to 100 Hz), the simplest physical explanation was adopted early on and has worked remarkably well. Linear Hooke's law for an elastic, homogeneous, and isotropic medium has proven able to predict particle displacement in P-waves and S-waves well enough to find oil and gas. Only three real-valued, frequency-independent material parameters are required to define a wave equation: longitudinal modulus, shear modulus, and mass density. The small amplitude inaccuracies in displacement due to "over simplification" did not matter because seismic processing was primarily based on moveout. Now that we need "true amplitude" processing, seismology has become more complex. Anelastic seismology relaxes the elasticity assumption by making the moduli complex-valued, to allow for frequency-dependent attenuation and dispersion.

On the opposite extreme, for EM exploration, the frequency bandwidth is much wider (say, .01 to 10 Hz), and velocity dispersion and attenuation are strong. A simplest physical

explanation is found by starting with the relatively involved Maxwell's equations and peeling off unnecessary complexities. I say "relatively involved" because the equations involve three complex-valued, frequency-dependent material tensors: electric conductivity, electric permittivity, and magnetic permeability. The parameters are, in principle, complex-valued because each can build in first-order loss resonances, each characterized by its magnitude, and relaxation time constant. The parameters are frequency-dependent because different loss mechanisms apply in different frequency ranges. The material parameters are tensors, because most rocks are anisotropic.

For exploration geophysicists, this level of complexity is overkill in the EM exploration frequency band and for most earth media. The loss mechanisms for non-ferromagnetic materials have magnitudes too small, and relaxation time constants too short to greatly affect the magnetic field (Keller, 1988). Consequently, if we ignore ferromagnetic materials, magnetic permeability can be considered constant, and real-valued. Complex-valued electric permittivity is thought sufficient to model both conductivity and permittivity resonances; below microwave frequencies, conductivity can be considered constant (Jackson, 1999). Thus, we can consider conductivity real-valued, and frequency-independent. Of course, conductivity introduces frequency-dependent loss without being complex-valued, via Ohm's law. And, for this thesis, I consider that the materials are isotropic, hence the parameters are scalars.

Perhaps the biggest simplification is achieved by noting that, in the EM frequency band, the "displacement current" contribution due to permittivity is sufficiently swamped by the "conduction current" due to conductivity that we can ignore the displacement current altogether. Keller (1988) terms this the "inductive" regime, where Maxwell's equations effectively degenerate to the diffusion equation. Note that if air and other gasses are considered "Earth" materials, they provides important exceptions, in that EM waves travel with essentially no

attenuation or dispersion in air, and other gasses to a lesser degree. Thus, ignoring magnetic materials, air, and other gasses, we end up with only one real-valued, frequency-independent material parameter (electrical conductivity), and one universal constant (magnetic permeability), and we wind up with the diffusion equation.

Whether working with the seismic wave equation, or the EM diffusion equation, both admit plane-wave solutions expressed as sums of Fourier basis terms parameterized by a complex-valued wavenumber.

Appendix A restates this section in mathematical terms, and explores the motivations for complex anelastic seismic moduli, and for ignoring EM displacement current.

1.2 EM and seismic parameter comparisons

This section summarizes differences and similarities to expect between seismic and EM imaging by comparing wavenumbers k, as understood through quality factors Q, phase velocities v_{phs}, skin depths δ, transmission and reflection coefficients, and critical angles. Appendix B gives backup for the following observations:

1) The wavenumber governs EM and seismic solutions. It can be expressed in terms of its quality factor Q, and its phase velocity v_{phs}:

$$k(\omega) = \frac{\omega}{v_{phs}(\omega)}\left(1 - \frac{i}{2Q(\omega)}\right) \tag{1.2.1}$$

1a) In principle, the quality factor depends on frequency; however, it is frequency-independent for both EM and seismic exploration. Its importance to EM imaging is paramount since, for EM, Q is *always* equal to ½ (Thomsen,

2014), while it is generally ignored in seismic imaging since its value differs for each material, and generally exceeds 30 (Futterman, 1962).

1b) Seismic phase velocities have a relatively narrow range that is only mildly affected by dispersion, while EM phase velocities are highly dispersive, resistivity-dependent, and have a broader range. Hence, generating an image using EM phase velocities must take frequency into account, much more so than using seismic phase velocities.

2) The imaginary part of the wavenumber governs attenuation. The skin depth δ is one measure of this attenuation and is defined as the depth at which wave amplitude has decayed to e^{-1} (about 37%) times its original value. In terms of quantities already defined, it is:

$$\delta(\omega) = \frac{-1}{\mathrm{Im}\{k(\omega)\}} = \frac{2v_{phs}(\omega)Q}{\omega} \tag{1.2.2}$$

We will see below that EM skin depths are proportional to $\sqrt{\rho}$. Since shallow strata tend toward low resistivity, EM will usually not image as deeply as seismic.

3) Seismic processing is designed to image relatively low impedance contrasts associated with reflected modes (reflection coefficients), while EM processing should image relatively high impedance contrasts associated with critically refracted modes (*cf.* Appendix B). Hence, while large reflection coefficients can be problematic in seismic imaging, they are integral to EM imaging.

4) Similarly, in seismic processing, near-vertical critical angles are problematic, while they are prospective in EM processing. Hence, critical and post-critical refracted waves which are "noise" in the seismic case, are "signal" in the EM case.

1.3 Consequences of the deep connection

Thomsen *et al.* (2007, 2009), Strack *et al.* (2008), and Thomsen (2014) argue that the deep connection between electromagnetics and seismology suggests that many *seismic* methods of acquisition and processing could be useful for *EM* data. Quoting Thomsen (2014) extensively:

1) "Both wave types may be described as a Fourier superposition of plane waves.

2) The wave vectors in both cases have both real and imaginary parts, which lead to dispersive, attenuative propagation.

3) Hence, although seismic dispersion and attenuation are weak, whereas EM dispersion and attenuation are strong, *any* seismic processing algorithm which does *not* assume weak dispersion and attenuation is, in principle, applicable to EM data processing.

4) In particular, EM data may be directly *imaged*, using seismic-like techniques, *rather than* mathematically *inverted* for subsurface physical properties; this has various advantages, including less sensitivity to source strength and orientation.

5) In both seismic and EM cases, since the signal from the subsurface is weak, it is best to detect it *without* a concurrent active source. Hence, EM data should (optimally) be Impulsive-Source (ISEM), rather than Continuous-Source (CSEM) data. Further, the EM receivers should not be spatially aliased.

6) The phase velocities of EM waves at low frequencies (~1 Hz) are *comparable* to seismic velocities (several km/s), so that seismic-style acquisition parameters are feasible, and moveout of the EM signal is a primary observable."

This thesis presents evidence supporting the above arguments. Further, I show that several seismic processing algorithms which are ineffective for EM data, due to its dispersion and

attenuation (see point 3) above, may be modified in straightforward fashion, to make them effective for processing EM exploration data.

1.4 Conventional marine CSEM acquisition

A typical survey is acquired by towing a horizontal electric dipole transmitter a few tens of meters above the seafloor, and recording fields on the seabed with independently deployed receivers. This arrangement is depicted in Figure 1.4.1.

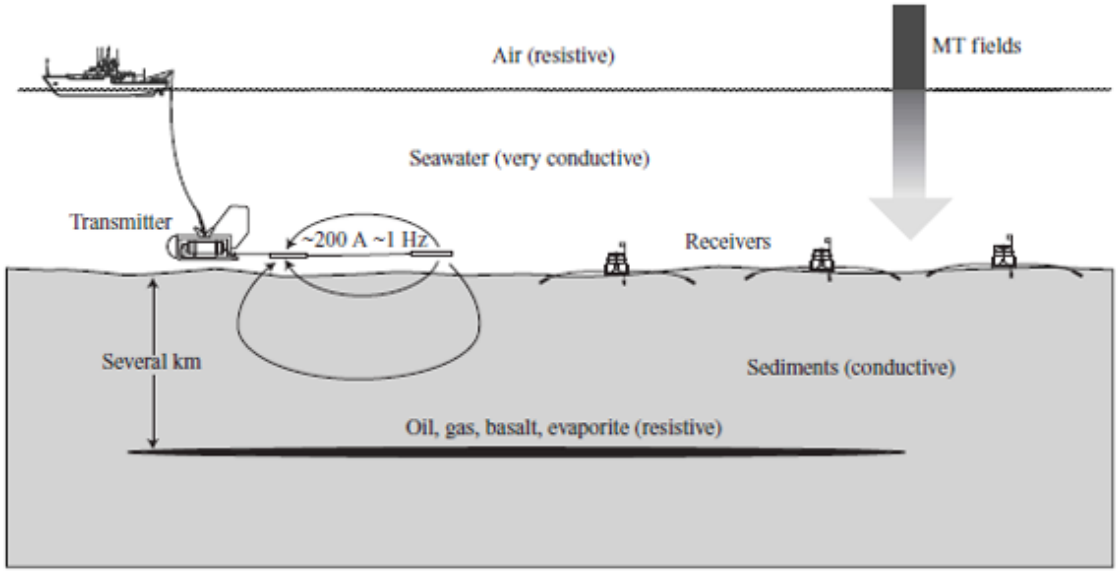

Figure 1.4.1: Conventional CSEM acquisition with towed transmitter and sea-bed receivers (from Figure 1 in Constable and Weiss, 2006)

In the cartoon, the source is specified as a 1 Hz square wave (continuously on), with maximum amplitude 200 A. The dipole length is several hundred meters long; this arrangement generates enough radiated power to image reflectors to 2 or 3 km depth, under favorable circumstances. The receivers are 2-arm (inline & crossline) horizontal dipoles, with arm lengths of about 10 m; there may also be coils measuring the magnetic field. In this thesis, only the inline horizontal component of the electric field is analyzed.

Another common arrangement replaces the sea-bed receivers with cable-based receivers towed along the sea-bed inline with the source, as depicted in Figure 1.4.2.

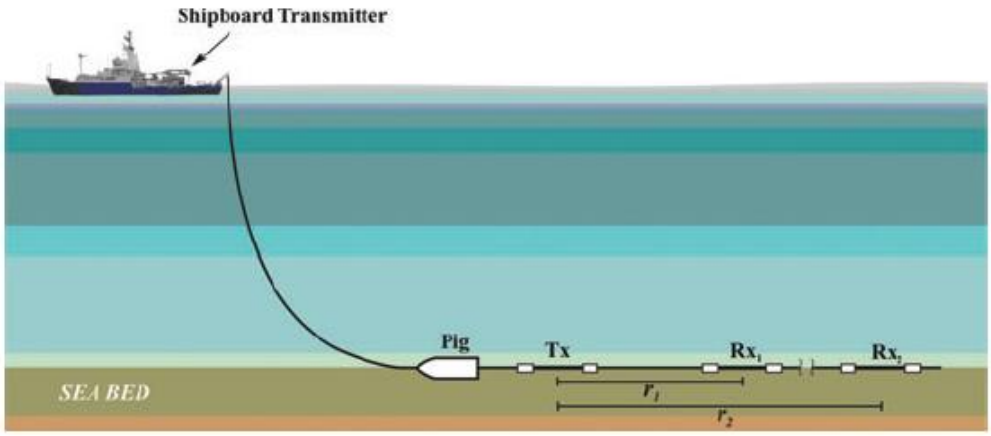

Figure 1.4.2: Conventional CSEM acquisition with sea-bed towed transmitter and inline E-field receivers (from Swidinsky and Edwards, 2009)

A newer scheme intended for simultaneous use with seismic acquisition is depicted in Figure 1.4.3. Here, the shallow transmitter and receivers enable efficient acquisition in shallow water depths.

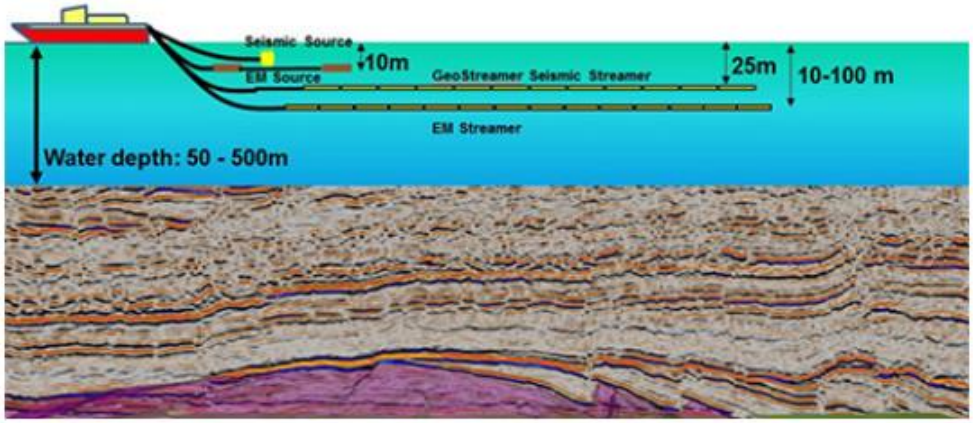

Figure 1.4.3: Conventional CSEM acquisition with shallow streamer towed transmitter and receivers (from http://www.pgs.com/Geophysical-Services/Towed-Streamer-EM/ *), (note that a seismic image has been displayed below the seafloor in this cartoon).*

1.5 Plan for this thesis

In Section 2, simulations are presented for several variations of a standard 1-D numerical EM model using seismic-style acquisition parameters – an impulsive source and many receivers. Intuition is built by exploring ray paths for the model. These ray paths include those for critically and post-critically refracted waves, described herein as "lateral waves", although, in the strictest sense, a lateral wave can only occur at the interface between semi-infinite half spaces. The importance of normalization is illustrated in seismic-style displays.

In Section 3, standard seismic processing methods are applied to the normalized simulations. Seismic methods based on moveout are applied to the data:

a) Velocity (semblance) analysis and stacking

b) *f-k* transform and filtering

c) Radon transforms

Applying these methods represents a first cut at understanding. Where practical, modifications are made to the standard algorithms to accommodate the linear moveout of lateral waves. The methods are judged as to effectiveness in detecting the reservoir, by comparing their output for models without and with the reservoir. Of these, the Radon transform is found to be the most effective. Sampling considerations for the Radon transform are discussed in Appendix D.1.

In a second cut, Section 4 reports on two efforts made to take frequency out of the EM experiment and to identify resistivity. Both efforts exploit the fact that the frequency dependence of EM moveout velocity is determined by resistivity. A resistivity moveout correction is defined and illustrated. Then this concept is applied to the Radon transform, producing an "EM-Radon" transform that is shown to transform time versus offset (t, x) space to intercept versus resistivity (τ, ρ) space, giving an indication of the reservoir's "effective

resistivity" as well as its existence. Sampling considerations for the EM-Radon transform are explored in Appendix D.2.

Sections 5 and 6 report on tests for the robustness of the EM-Radon transform to noise, to decimation of the receivers, and to sparser time-sampling.

In Section 7, the sensitivity of the EM-Radon transform is studied to variations in the depth and thickness of the reservoir, and to the resistivity of the reservoir.

Section 8 demonstrates that the EM-Radon transform produces results consistent with T-equivalence. This suggests that the "effective resistivity" indicated might better be termed "T-equivalent resistivity". The connection between T-equivalence and lateral waves is explored in Appendix C.

Section 9 presents suggestions for future work, and conclusions.

2 Numerical EM simulations

2.1 Canonical Model

In the CSEM community, a 1D "Canonical Model" (Constable and Weiss, 2006) is often used for academic studies (Figure 2.1.1). It is comprised of an upper half space of air (resistivity $\rho=10^{12}$ Ohm-m), over ocean ($\rho=0.3$) 1 km deep, over sediments ($\rho=1.0$) 1 km thick, over reservoir rock ($\rho=100.0$) 100 m thick, over a lower half space of sediments. The source is an in-line horizontal electric current dipole at 50 m above the seafloor. To create pleasing seismic-style displays, negative polarity is chosen for the source.

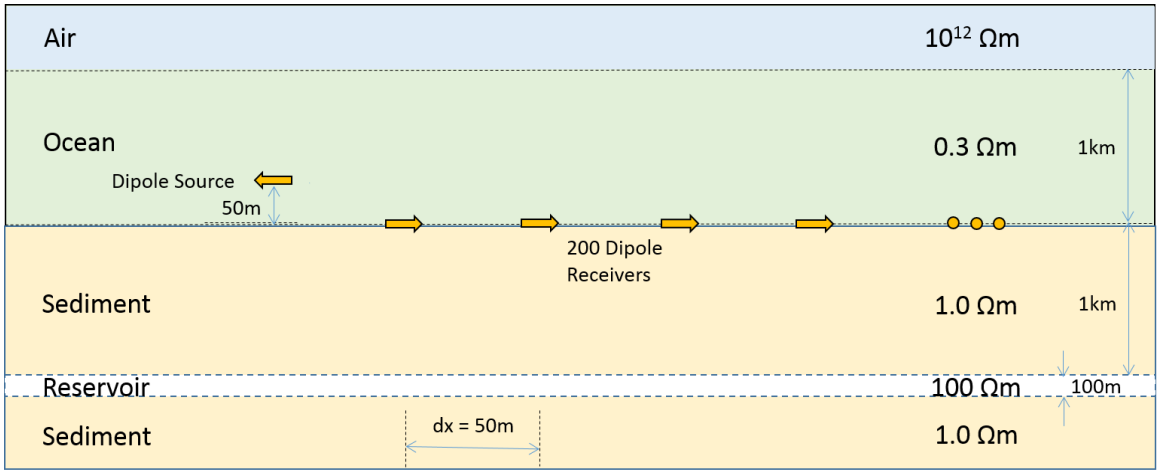

Figure 2.1.1: 1-D Canonical Model

Strictly speaking, for simulation of propagation in air, the wave equation displacement term should be included. However, the very high resistivity of air (1.30×10^{16} to 3.30×10^{16} Ωm at 20° C (Pawar *et al., 2009*)) minimizes its attendant diffusion characteristics.

Also strictly speaking, the word "sediment" normally refers to sedimentary deposits that are not indurated; while, at model depths exceeding 1 km, most sediment will have been lithified into "sedimentary rock". In deference to Constable and Weiss (2006) and to common

usage in the CSEM community, in this thesis the word “sediment” is meant to include sediments that have undergone any degree of lithification.

Data is synthesized using acquisition parameters that emphasize similarity to standard seismic acquisition: an impulsive source, receivers being 200 in-line horizontal electric dipole antennae, stationed from 50 m to 10 km offset (50 m intervals) along the ocean bottom, with a 20 second recording time at a 2 millisecond sample rate.

To explore reported problems identifying the reservoir in shallower waters, a “shallow-water model” is also simulated, identical to the Canonical Model except for a shallower (500 m) deep ocean.

2.2 Ray paths under the high-frequency approximation

Figure 2.2.1 shows ray paths for the Canonical Model. Ray tracing is only strictly valid for electromagnetic waves whose wavelengths are much shorter than the dimensions of the Canonical Model, which is not the case here. Nonetheless, the hope is that it will give a starting place for developing intuition, just as it does for seismic analysis. We must keep in mind that EM waves see identical dimensions differently at different frequencies, so that intuition valid at higher frequencies may often need to be modified for lower frequencies (*cf.* Appendix C).

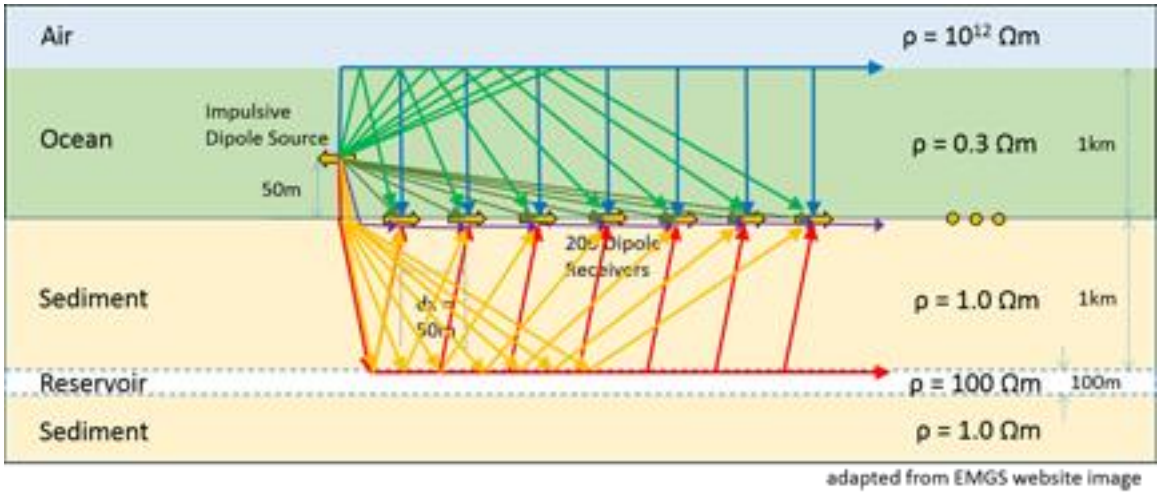

Figure 2.2.1: Ray paths for the Canonical Model

In Figure 2.2.1, lateral waves are illustrated at the air-ocean interface (the dark blue "air wave"), at the ocean-sediment interface (the purple "sediment wave") and at the sediment-reservoir interface (the red "reservoir wave"). At and beyond the critical angle of incidence, a well-developed lateral wave travels at the phase velocity of the "faster" medium, this is: for the air wave the speed of light in air, for the sediment wave the speed in sediment, and for the reservoir wave the speed in the reservoir. Except for the air wave, these velocities are frequency-dependent, but the critical angle of incidence at which the lateral wave develops is not frequency-dependent (*cf.* Appendix B). In this Canonical Model, the air wave critical angle is nearly 0°, for the sediment wave it is nearly 34°, and for the reservoir wave it is about 7°. Each of these lateral waves develops after a frequency-dependent time lag determined by the pathlength and the medium (or media) traversed between the source dipole and the subject interface. At sufficiently far offset, all three lateral waves will exhibit nearly linear moveout. Also, the faster media will exhibit less attenuation at a given frequency, since their wavelengths are longer. For the air wave, there is no attenuation.

Beyond the critical angle of incidence, each lateral wave travels at a lesser phase velocity given by the phase velocity of the "slower" medium divided by the sine of the incidence angle (Balanis, 1989). Therefore, components of these waves travel at a spectrum of phase velocities lying between that of the faster and slower media, with phase velocity decreasing as the post-critical angle of incidence increases.

As mentioned above, in the strictest sense, a lateral wave can only occur at the interface between semi-infinite half spaces. Since this condition never applies for the Canonical Model, we need to look out for the effect of finite bed thicknesses, especially of the reservoir.

Figure 2.2.1 also illustrates the direct ocean wave (olive green) which will also exhibit nearly linear moveout. Reflected waves in the ocean (yellow) and sediment (orange) will exhibit hyperbolic (known as "normal") moveout, at each frequency.

2.3 Simulations in layered media

A MATLAB code written by Kerry Key (UCSD: Key, 2012) is available from the SEG at http://software.seg.org/2012/0003 to perform EM simulations of the diffusion equation for propagation in layered media. This code includes options for time- and frequency-domain output for electric and magnetic field components recorded in the same horizontal layer as an impulsive horizontal electric source. It uses numerical techniques which are conventional, within the EM community. Bessel function frequency-domain integral solutions are computed via Fast Hankel Transform (FHT) digital filters or via the sum of partial integrals evaluated using quadrature. Time-domain solutions are assembled from a range of frequency-domain solutions using sine and cosine digital filters. For this study, 201 point FHT filters and 201 point cosine filters produce a satisfactory result in about 24 minutes of compute time on an HP Pavilion Notebook PC with a Dual-Core 2.5 GHz processor.

2.4 Un-normalized versus normalized seismic-style displays

For seismic-style processing, simulations are imported into the Seismic Un*x ("SU") seismic processing package (Stockwell and Cohen, 2008). Since my PC is Windows-based, the UNIX-emulator CYGWIN is used to set up the appropriate environment. SU uses numerical techniques which are conventional, within the seismic community.

Seismic-style displays (SUXIMAGE routine in SU) of the simulations are presented in Figure 2.4.1. In keeping with seismic practice, time traces are plotted against receiver offset. In Figure 2.4.1, the Canonical Model is built up progressively, with the first four images showing simulations with a) whole space seawater, and adding in b) sediment, in c) air, and in d) the reservoir. Parts e) and f) are the equivalent of c) and d), but for a shallow-water model (with water depth 0.5 km, all other parameters identical).

We see how quickly trace amplitude decays in time and offset, showing that it is difficult to discern moveout at true amplitude. This decay is much more severe than for seismic data, since the Q factor for EM data is so low. The standard EM practice to deal with this decay is to compute at each (t, x) from the data, an "apparent resistivity" (i.e., the resistivity of a homogeneous full-space which would yield the same amplitude, given the known source strength).

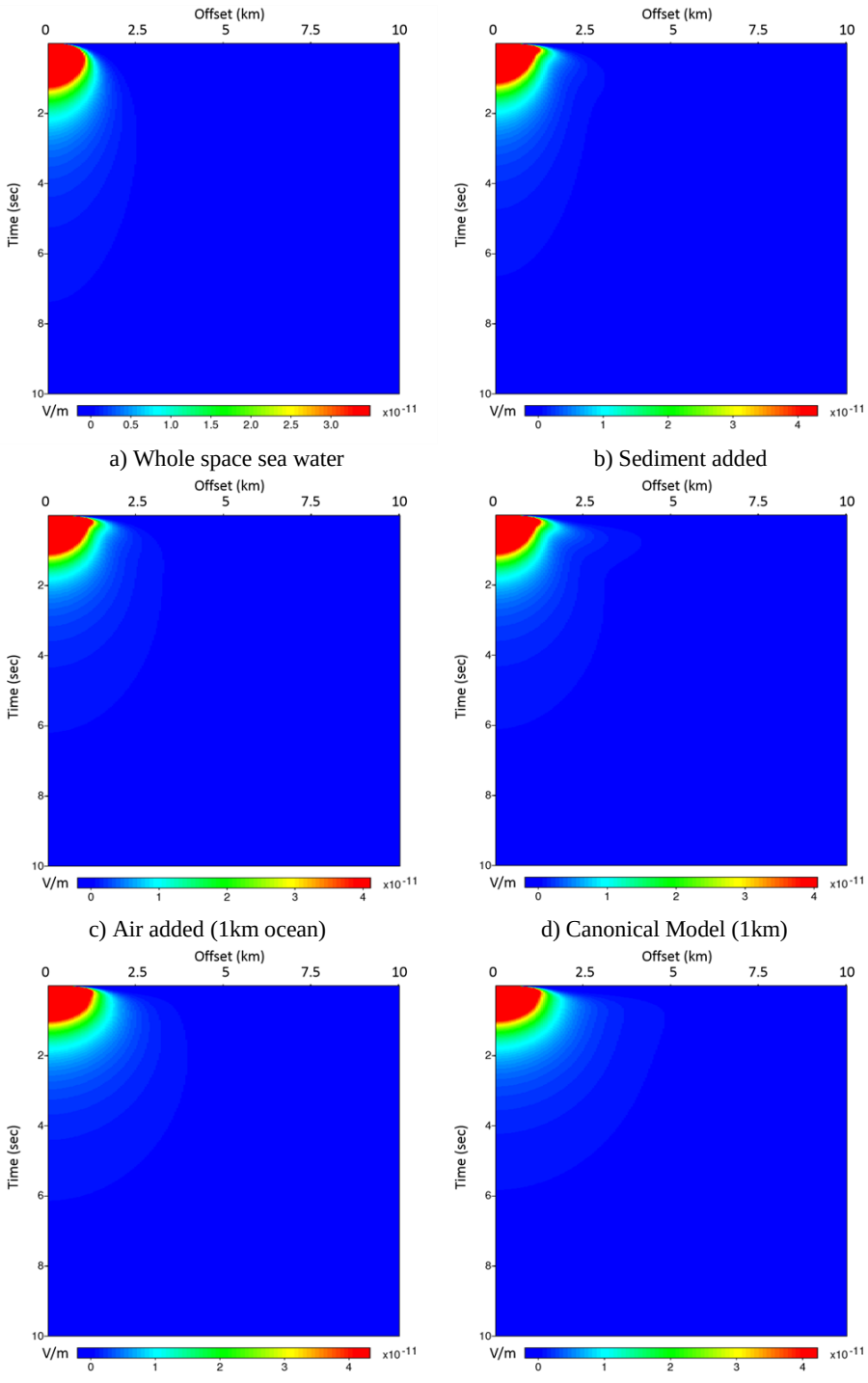

a) Whole space sea water

b) Sediment added

c) Air added (1km ocean)

d) Canonical Model (1km)

e) Shallow-water w/o res.

f) Shallow-water Model

Figure 2.4.1: Un-normalized seismic-style displays of inline horizontal electric field component [volts/meter].

Here, however, each trace is instead normalized to unit amplitude, seismic-style. Figure 2.4.2 shows that, with such display, the moveout is readily apparent. This simple normalization makes the weak far-offset signal visible (seismic-style) without computation of apparent resistivity (EM-style). Compare each of these plots with the corresponding plot in Figure 2.4.1. Each element possesses a distinctive moveout, similar to seismic data, but with significant dispersion. In particular, the presence of the reservoir arrival is obvious (in Figure 2.4.2d), compared to the same model without reservoir (in Figure 2.4.2c). In this way, the apparently trivial act of normalization and display becomes a non-trivial aspect of the analysis (Strack *et al.*, 2007). The corresponding differences for the shallow-water model (in Figures 2.4.2ef) are also clear, but with a different character. The shallow-water model without reservoir (Figure 2.4.2e) shows a region at moderate-to-large offset with a prominent arrival with very rapid moveout, arriving before 1 second. This is the air wave, which causes problems with conventional CSEM (amplitude-based) analysis by interfering strongly with the reservoir wave. But using the present seismic-style acquisition (impulsive source, many receivers), when the reservoir is present (Figure 2.4.2f), the character of the moveout is different (slower than air, but faster than sediment), even to the eye.

It is critical that these velocities are comparable to seismic velocities (a few km/s), many orders of magnitude less than the EM velocity in these same materials at high frequency (*cf.* further discussion in Appendix A). Hence, they are measurable with seismic-style acquisition.

A further critical point is that the gain factors applied in the normalization procedure are much larger (see Section 2.5) than those in seismic practice. However, conventional EM acquisition is able to detect the very small signals at large offsets (which have been amplified so strongly); the robustness (of the present analysis) to noise is discussed in Section 5.

I will seek to quantify these differences via seismic-style processing.

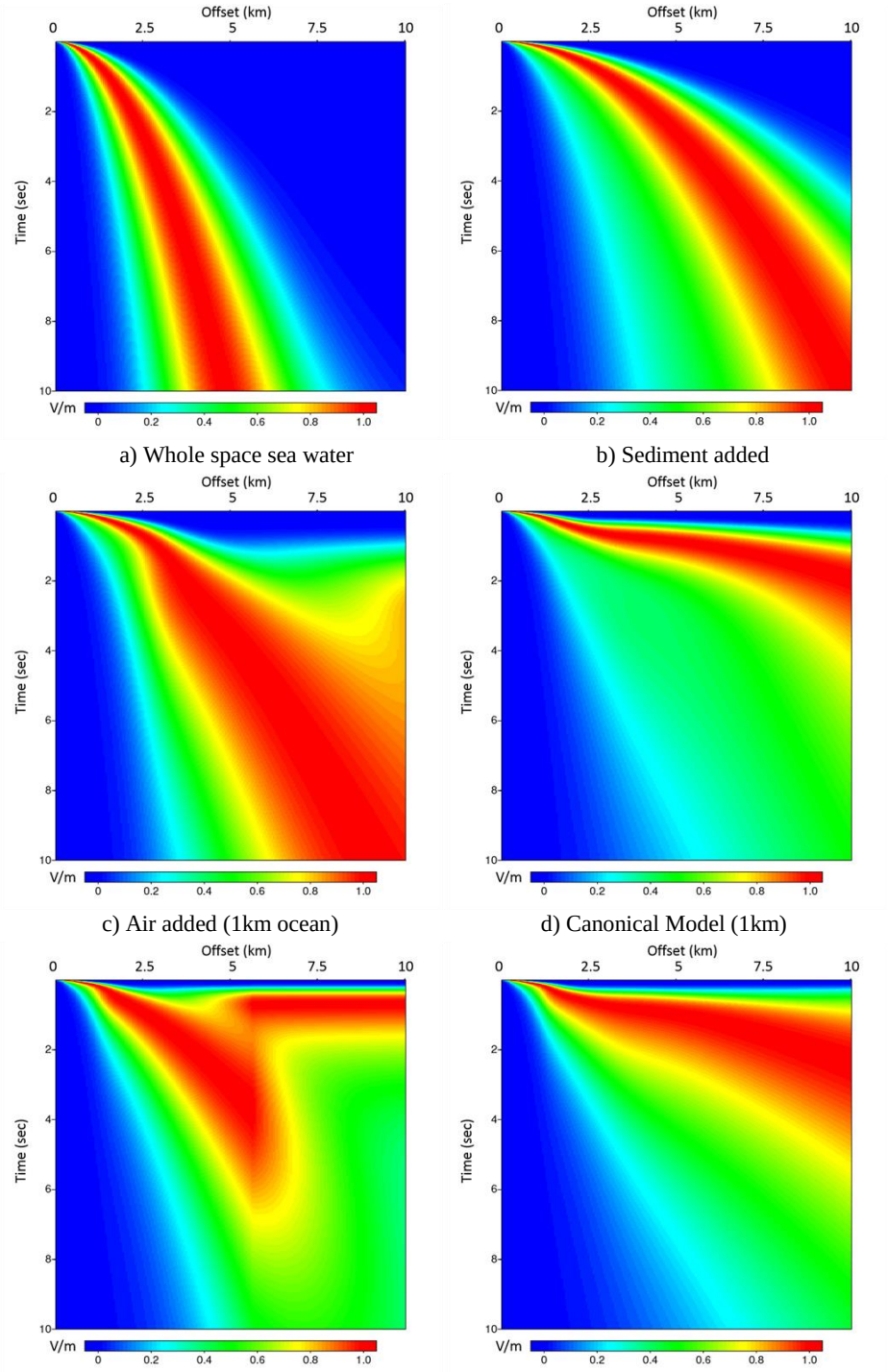

a) Whole space sea water

b) Sediment added

c) Air added (1km ocean)

d) Canonical Model (1km)

e) Shallow-water w/o res.

f) Shallow-water Model

Figure 2.4.2: Normalized seismic-style displays of inline horizontal electric field component [volts/meter (normalized to unit maximum value at each offset)].

The low-frequency EM body-wave phase slowness (inverse of velocity) for a homogeneous non-magnetic isotropic body has real part given by (*cf.* Appendix A):

$$p(\omega) = \frac{1}{v_{phs}(\omega)} \equiv \frac{\mathrm{Re}\{k(\omega)\}}{\omega} = \sqrt{\frac{\mu_0}{2\rho\omega}} \tag{2.4.1}$$

Here $\boldsymbol{\mu}_0$ is the magnetic permeability of free space ($4\pi \cdot 10^{-7}$ H/m). This formula, along with the analysis of Thomsen (2014) for a body wave at an interface, leads to the following description of these plots. The "air wave" propagates slowly up through the seawater, refracts horizontally through the air at the speed of light in air, then propagates slowly back down to the receivers. This is evident in the early arrival at far offsets, which is obvious in part c), and even more obvious in part e), with its shallower water layer.

Similarly the reservoir wave propagates slowly down to the reservoir though the sediments, refracts rapidly along the reservoir, then propagates slowly back up to the receivers.

The above behavior suggests that identifying the reservoir by means of conventional seismic processing tools via the different *moveouts* of various modes, rather than via their amplitudes, may be feasible (Thomsen *et al.*, 2009). Because the air wave is excited impulsively, rather than continuously, it arrives late and fast, and is easily distinguished from the signal (Thomsen *et al.*, 2009).

2.5 Use of normalized data

The applied normalization is simply an offset-variable, time-independent scalar gain:

$$\vec{u}_{norm}(x,t) = s(x)\vec{u}(x,t) \tag{2.5.1}$$

Here:

$$s(x) \equiv [\max \left\| \vec{u}(x,t) \right\|]^{-1} (over\ all\ t, given\ x) \qquad (2.5.2)$$

This thesis considers normalized data instead of the original un-normalized data. The use of the normalized data means that seismic processing of the EM data will seek to interpret the moveout of the data, not its amplitude; this is a major difference from conventional EM analysis. This normalization is also not frequency-dependent, unlike computation of apparent resistivity (EM-style). Of course, the original data may be recovered at any time, since the gain factors $s(x)$ are retained (Figure 2.5.1, below).

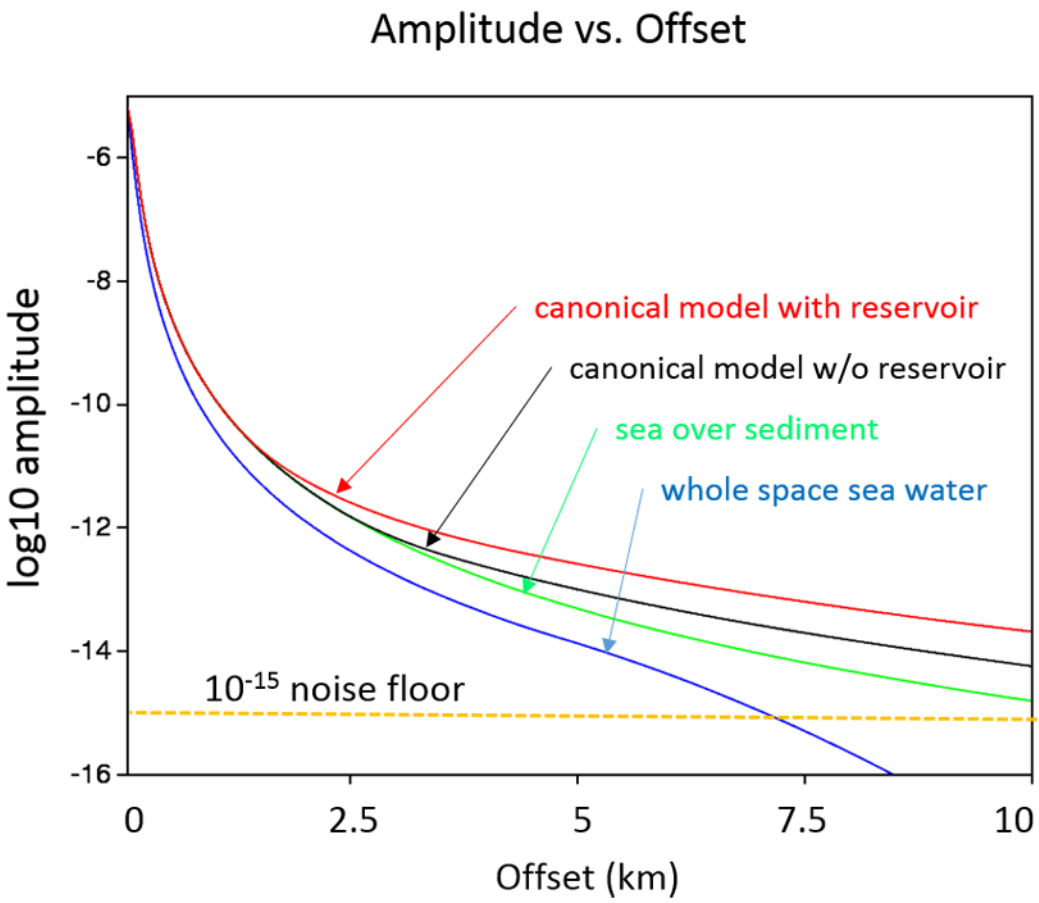

Figure 2.5.1: Inline horizontal electric field amplitude vs. offset [volts/meter] → inverse of gain factors used for numerical data normalization

3 Application of standard seismic moveout algorithms

3.1 Frequency content

Figure 3.1.1 shows a frequency spectrum (SUSPECFX in SU) for the Canonical Model, Figure 2.4.1d. Notable is the loss of high frequency with offset, despite the trace normalization. Further, note that the refracted waves (air, reservoir) re-introduce higher frequency content at the longer offsets.

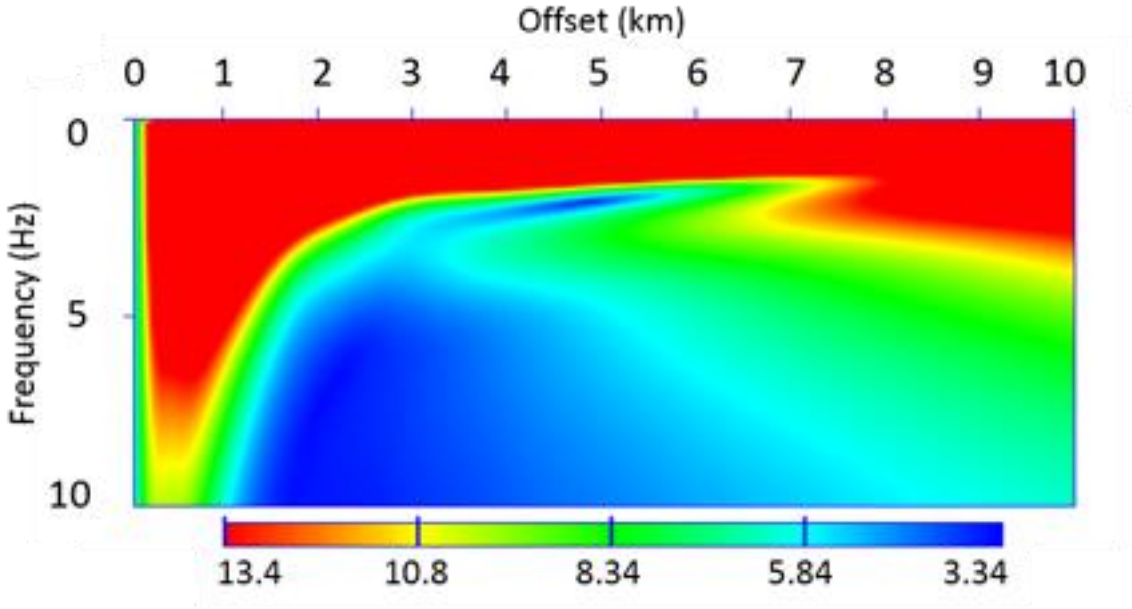

Figure 3.1.1: Frequency content of normalized inline horizontal electric field component for Canonical Model [volts/meter (scaled by Fourier transform algorithm)]

3.2 Velocity (semblance) analysis and stacking

Semblance is computed with a modified version of SU's SUVELAN program embedded in a UNIX script adapted from iva.sh (Forel *et al.*, 2005). The SUVELAN program is converted from hyperbolic moveout (NMO) to linear moveout, due to the expectation that sediment, reservoir, and air lateral waves are dominant. Figure 3.2.1 shows output from the script for the

Canonical Model with and without the reservoir. Velocities run from 500 m/s up to 38000 m/s in 150 increments.

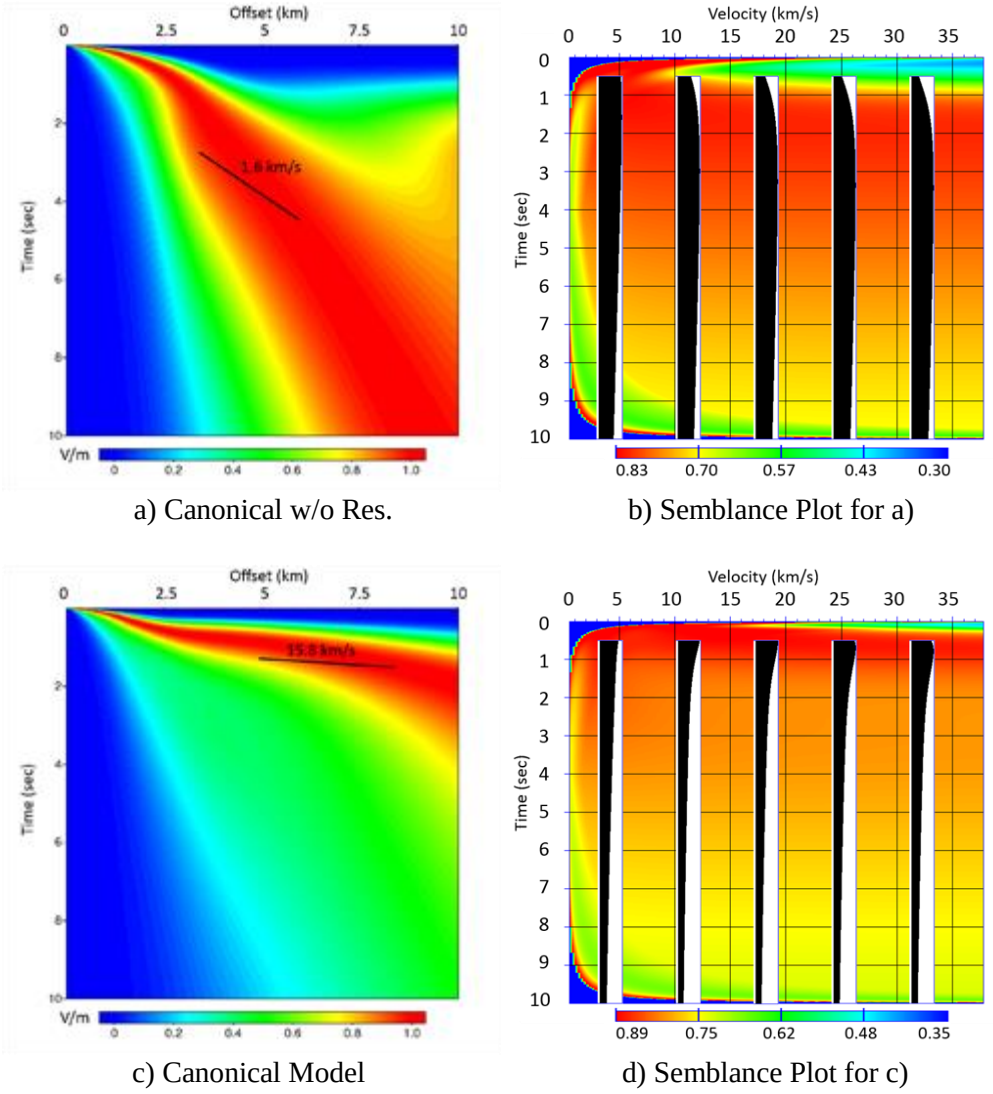

a) Canonical w/o Res. b) Semblance Plot for a)

c) Canonical Model d) Semblance Plot for c)

Figure 3.2.1: Semblance plots with constant velocity CMP stacks overlaid on the right [semblance units are normalized volts/meter (see legend), CMP stacks are normalized volts/meter wiggle plots] (@ 0.25 Hz: sediment wave velocity 1.6 km/s, reservoir wave velocity 15.8 km/s). Normalized horizontal inline electric field amplitudes on the left [normalized volts/meter] are input into the semblance and CMP stack routines.

Overlaid on the semblance plots (Figures 3.2.1bd) are limited-range (1-10km) Constant Velocity CMP Stacks computed at 3, 10, 17, 24, and 31 km/s. One sees notable differences in

the semblance plots and stacks; differences which suggest the ability to detect the reservoir on the basis of its moveout, rather than its amplitude (as in CSEM). Note that the detection does not rely upon forming the numerical difference between on-reservoir and off-reservoir datasets, as is commonly done is conventional CSEM analysis. However, the plots do not appear to be useful for picking stacking velocities; this is presumably because EM data arrives with a spectrum of lateral and dispersive phase velocities, and this seismic process does not take these into account.

3.3 *f-k* transform and filtering

The UNIX script ifk.sh (Forel *et al.*, 2005) studies the *f-k* amplitude spectrum produced by the SU program SUSPECFK. Figures 3.3.1ab show output from the script, for the simulations without and with reservoir, respectively. It is remarkable how similar are the two *f-k* plots, given the differences in the input data. It is not clear from the *f-k* plots what strategy would be promising for identifying the reservoir. It is possible that offset-dependent normalization obscures what is going on.

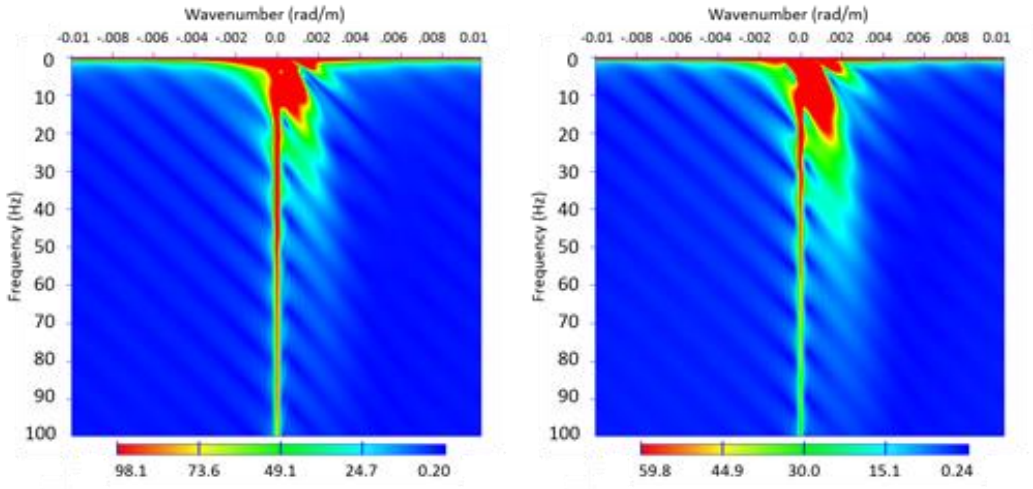

a) without reservoir b) with reservoir

Figure 3.3.1: Comparison of f-k plots for the normalized inline horizontal electric field for the Canonical Model without and with the reservoir [normalized volts/meter scaled by the Fourier transform algorithm].

3.4 Radon transforms

Radon transforms (SURADON in SU) for the Canonical Model are presented in Figure 3.4.1. In the absence of dispersion, an arrival refracted along the reservoir would appear as a straight *line* in time-offset space. We restrict ourselves to linear "tau-p" transforms here, so that the refracted reservoir arrival should, in the absence of dispersion, and at a given angle of incidence, approximate a *point* in the tau-p (vertical time – slowness) domain. Dispersion and varying incidence smear this point considerably, as shown in Figure 3.4.1b.

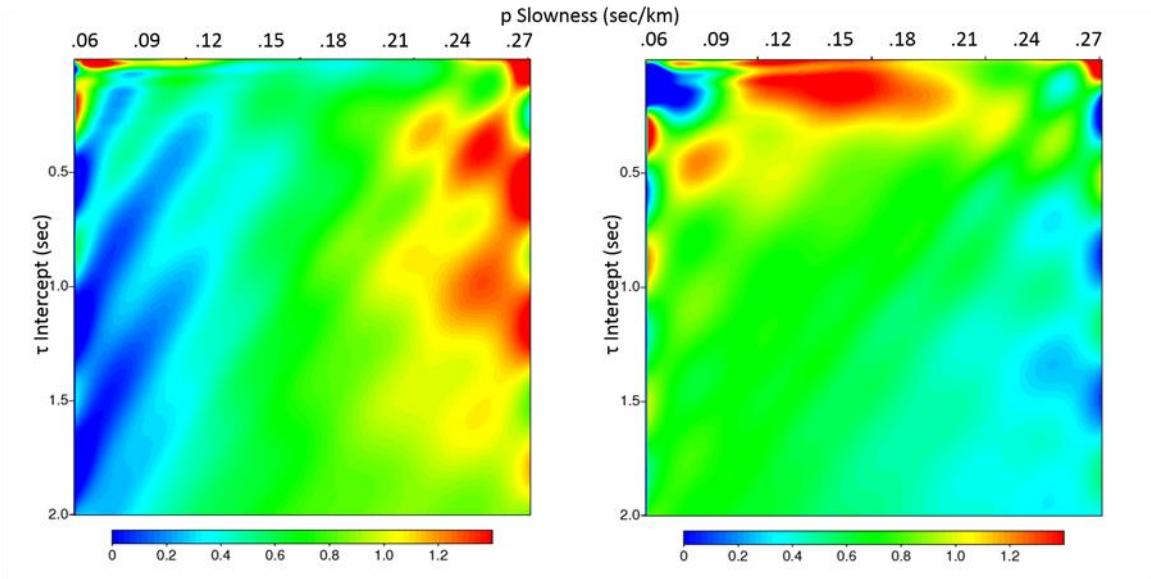

a) Canonical w/o reservoir *b) Canonical Model*

Figure 3.4.1: Comparison of Radon transforms of the normalized inline horizontal electric field for the Canonical Model without and with reservoir [normalized volts/meter].

Following experiential guidelines (Yilmaz, 2001), the number of p values is set equal to the number of offsets (200), and the p range is chosen to bracket slownesses of interest: (.03-.27) s/km (33-4 km/s). These p values satisfy the theoretical Turner (1990) anti-aliasing criteria presented in Appendix D.1. Strong energy is present (at early tau) for slowness between 0.1 and 0.2 s/km (velocity: 5-10 km/s) when the reservoir is present. By contrast, when the reservoir is absent, the early energy is arriving diffusely, and with much larger slowness (> 0.2

s/km (low velocity: 5 km/s)). The phase velocity 10 km/s corresponds to a wave refracting along the reservoir (100 Ωm) at about 0.1 Hz.

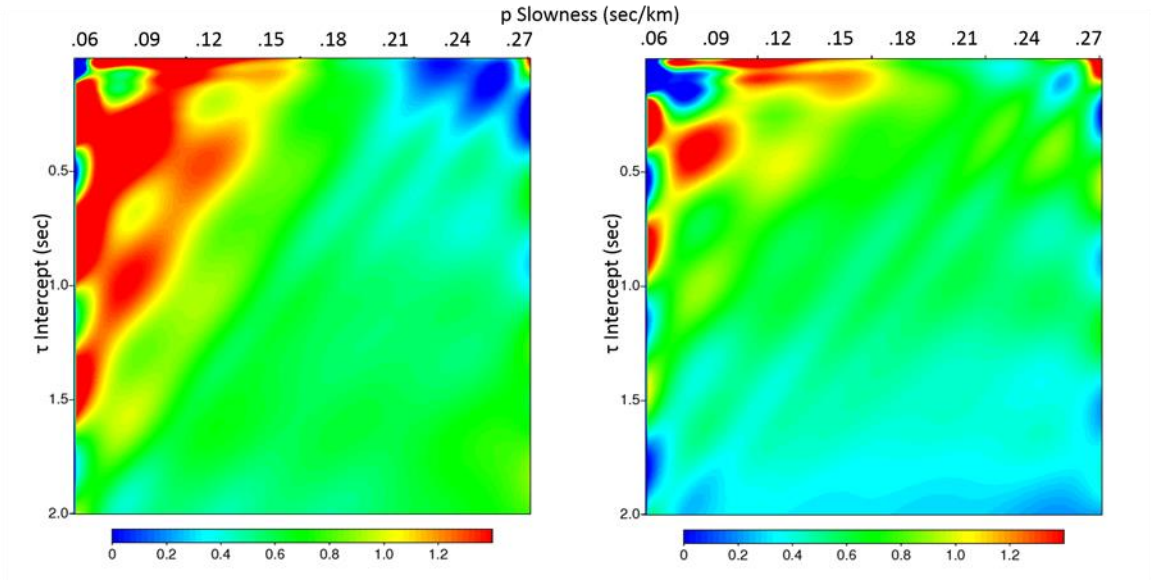

a) Canonical w/o reservoir *b) Canonical Model*

Figure 3.4.2: Comparison of Radon transforms of the normalized inline horizontal electric field for the Shallow Model without and with reservoir [normalized volts/meter].

The result is less clear for the shallow-water model, Figures 3.4.2ab. At early tau, the reservoir slowness between 0.1 and 0.17 s/km only dominates when the reservoir is present Figure 3.4.2b. This shows that the Radon transform, is affected, but not completely frustrated by air wave interference.

It is worth mentioning that filtering via the Radon transform should be able to remove any noise that moves out very rapidly and without dispersion, like the air wave. Similarly, Radon transform filtering should be able to remove any noise that does not move out at all, like environmental noise (not present in our simulations, but discussed in Section 5).

4 Taking frequency out of the EM experiment and identifying resistivity

4.1 Resistivity moveout correction

The first effort to account for the strong frequency-dependence of EM data, and to focus on resistivity, is a resistivity moveout correction. This correction simply shifts the data's phase according to the Fourier transform's shift theorem (Bracewell, 1978). The linear moveout correction can be expressed as:

$$\vec{u}(t,x) \rightarrow \vec{u}(t-px,x) = \vec{u}(\tau,x,p) \tag{4.1.1}$$

where $\tau = t - px$ is the reduced or intercept time, and the slowness $\boldsymbol{p}$ may vary with frequency. Taking the Fourier transform F of the right-hand side, applying the shift theorem (choosing negative for the sign of the forward Fourier exponent), and using Equation (2.4.1) to relate slowness to resistivity:

$$F\{\vec{u}(t-px,x),\omega\} = e^{-i\omega p(\omega)x} F\{\vec{u}(t,x,\omega)\} = e^{-i\sqrt{\frac{\omega\mu_0}{2\rho}}x} F\{\vec{u}(t,x,\omega)\} \tag{4.1.2}$$

Thus, we can define the moveout correction for a given resistivity ρ (replacing the slowness):

$$\vec{u}(\tau,x,\rho) = F^{-1}\{e^{-i\sqrt{\frac{\omega\mu_0}{2\rho}}x} F\{\vec{u}(\tau+px,x,\omega)\}\} \tag{4.1.3}$$

4.2 Examples of resistivity moveout correction

Figure 4.2.1 shows a 100 Ωm resistivity moveout correction applied to the Canonical Model. We see that the moveout of the lateral reservoir wave is flattened considerably, and gives confidence that this resistivity value (which was input in the forward modeling) is consistent with the observed moveout.

Figure 4.2.2 shows a 10 Ωm resistivity moveout correction applied to the Canonical Model. We see that the moveout of the lateral reservoir wave is bent beyond flat – to negative (non-causal) moveout, suggesting that this resistivity value is not consistent with observed moveout.

Figure 4.2.3 shows a 1 Ωm resistivity moveout correction applied to the Canonical Model. We see that the moveout of the lateral reservoir wave is even more non-causal.

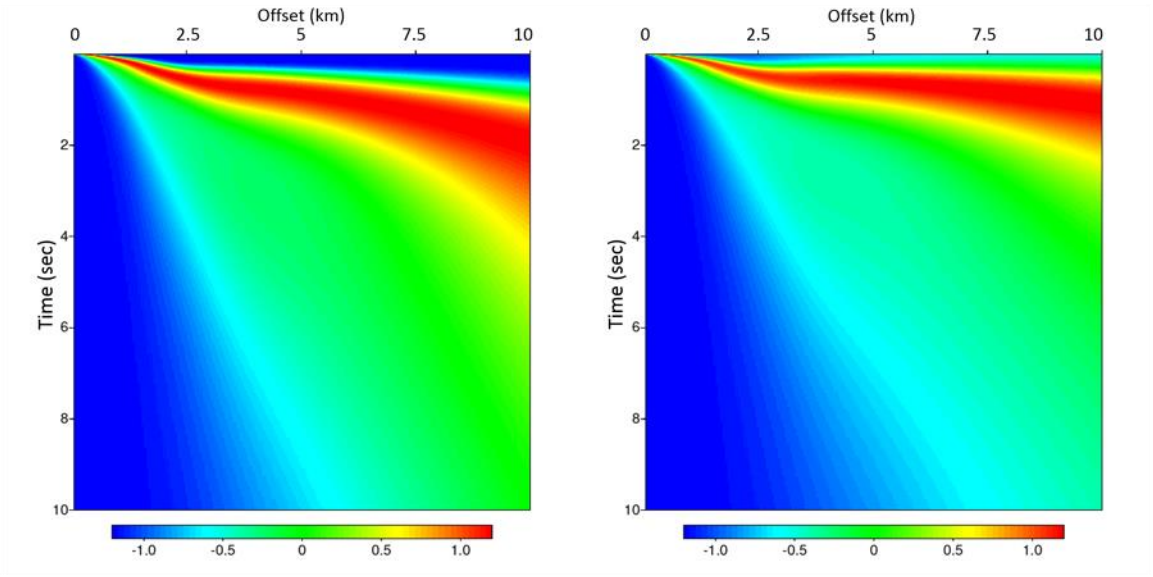

On left: Canonical Model *On right: Canonical @ 100 Ωm correction*

Figure 4.2.1: 100 Ωm moveout correction of normalized inline horizontal electric field amplitude for Canonical Model [normalized volts/meter].

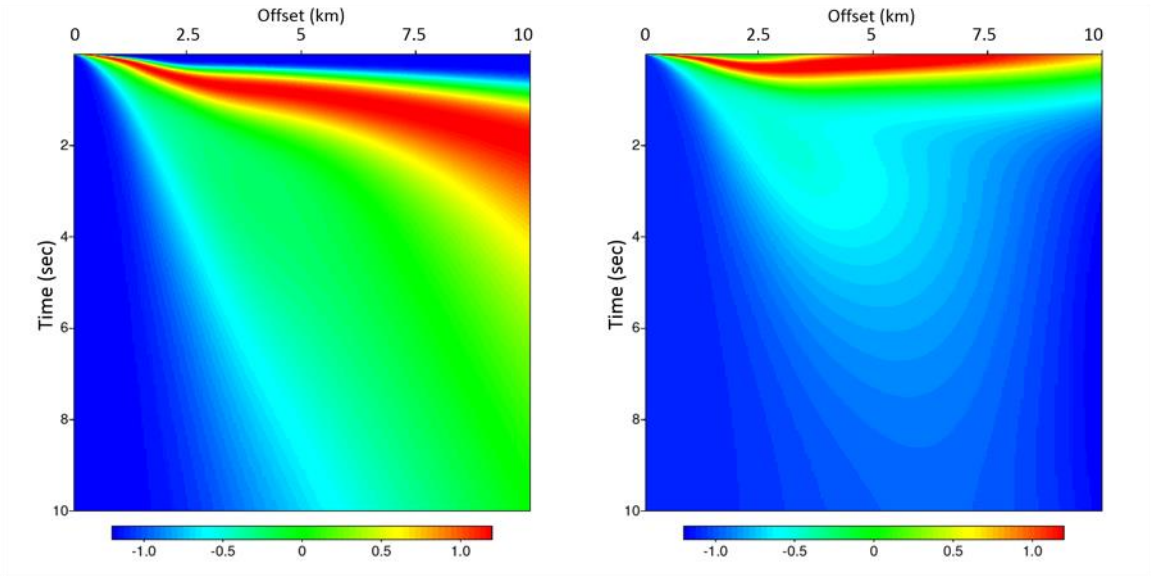

On left: Canonical Model *On right: Canonical @ 10 Ωm correction*

Figure 4.2.2: 10 Ωm moveout correction of normalized inline horizontal electric field amplitude for Canonical Model [normalized volts/meter].

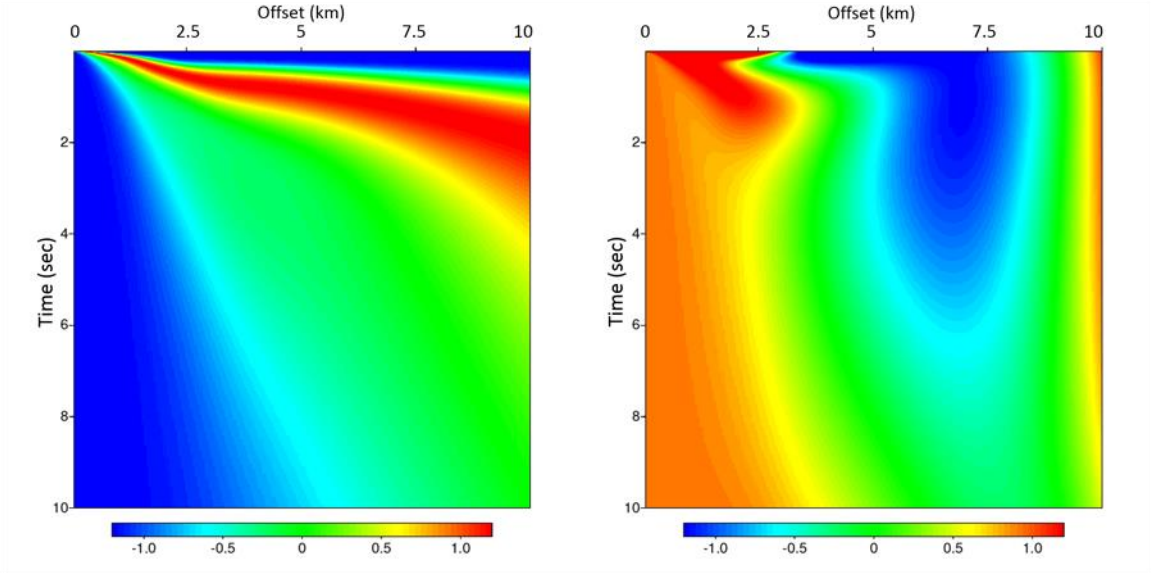

On left: Canonical Model *On right: Canonical @ 1 Ωm correction*

Figure 4.2.3: 1 Ωm moveout correction of normalized inline electric field amplitude for Canonical Model [normalized volts/meter].

Figures 4.2.4, 4.2.5, and 4.2.6 show, respectively, 100, 10, and 1 Ωm resistivity moveout corrections applied to the Canonical Model without reservoir. Beyond 2.5 km offset, none of

these data are flattened, even approximately; *i.e.*, there is little evidence of linear lateral moveout. At 1 Ωm resistivity, the moveout is predominately non-causal.

In sum, these Figures show that this simple version of resistivity moveout is able to indicate the existence of a reservoir and to estimate the reservoir's effective resistivity.

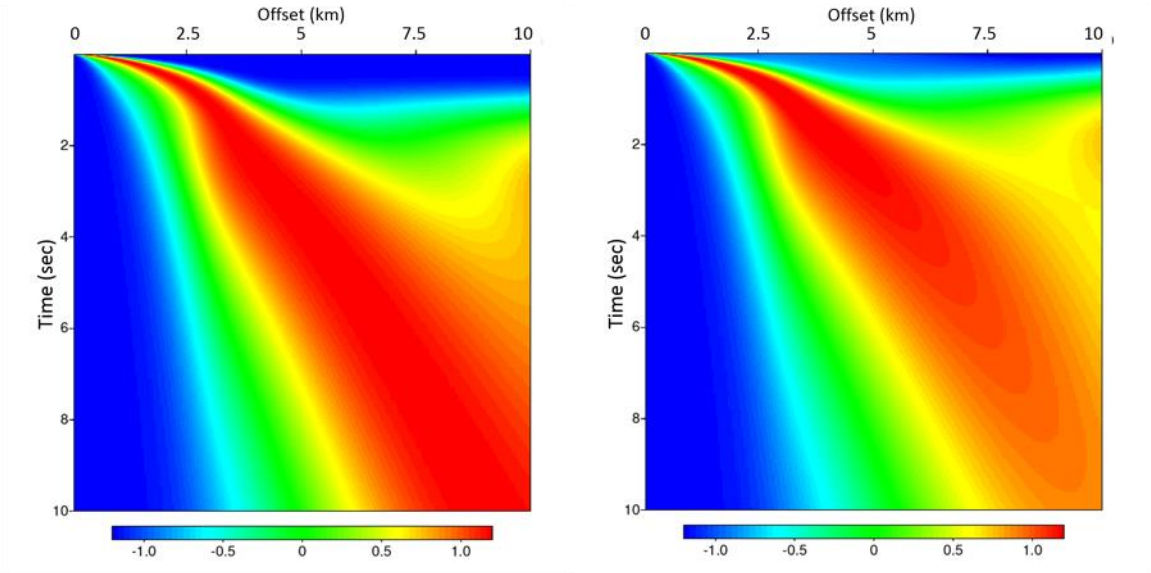

a) Canonical w/o reservoir *b) Canonical Model*

Figure 4.2.4: 100 Ωm moveout correction of normalized inline horizontal electric field amplitude for Canonical Model w/o reservoir [normalized volts/meter].

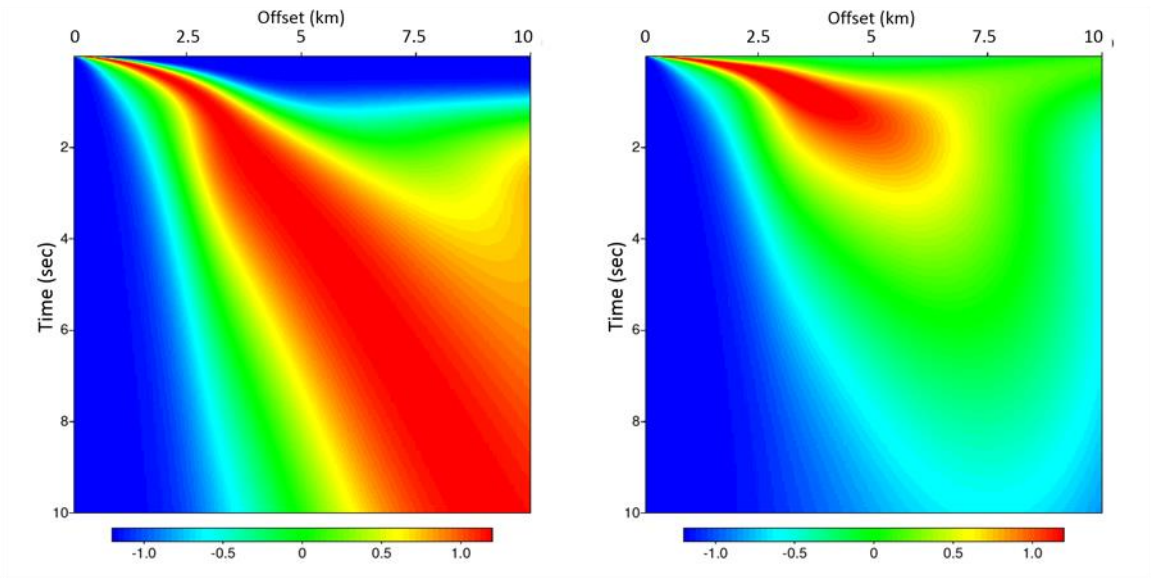

a) Canonical w/o reservoir *b) Canonical Model*

Figure 4.2.5: 10 Ωm moveout correction of normalized inline horizontal electric field amplitude for Canonical Model w/o reservoir [normalized volts/meter].

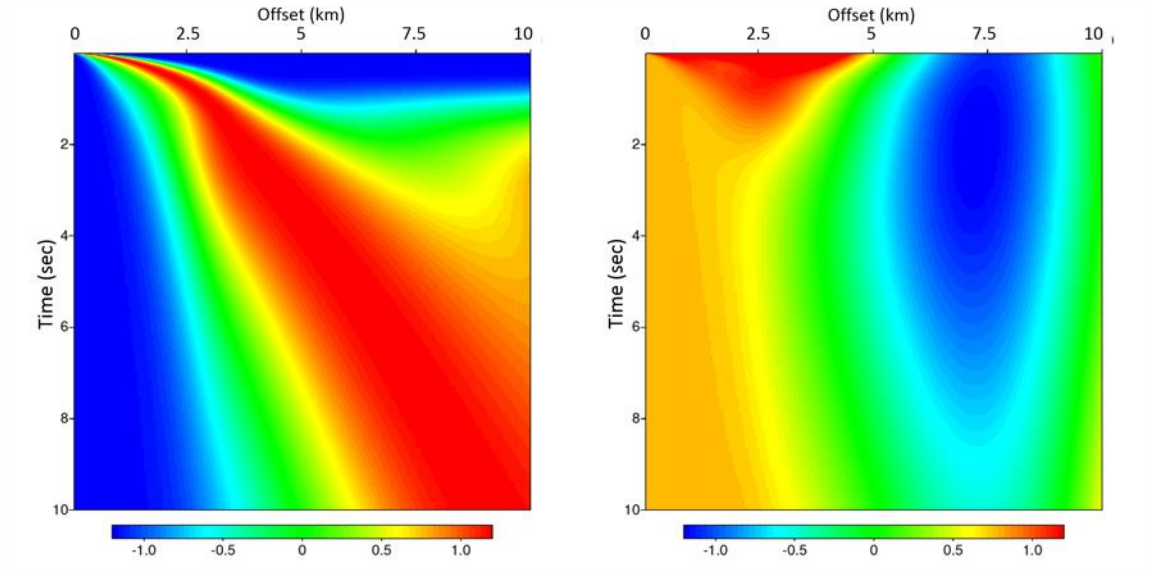

a) Canonical w/o reservoir b) Canonical Model

Figure 4.2.6: 1 Ωm moveout correction of normalized inline horizontal electric field amplitude for Canonical Model w/o reservoir [normalized volts/meter].

4.3 Radon resistivity transform

The second effort to account for the strong frequency-dependence of EM data, and to focus on resistivity, modifies the Radon transform using Equation (2.4.1) in a similar way and produces a Radon resistivity transform ("EM-Radon").

The SU code SURADON (Anderson, 1993) performs the bulk of its Radon transform computations in the frequency domain. This approach is particularly well-suited to EM, because it enables a natural allowance for the high dispersion of EM waves. After converting the data from the time domain to the frequency domain, SURADON computes slowness, one frequency at a time. Slowness can be converted to the square root of conductivity (inverse of resistivity) at each frequency, simply by dividing each slowness by $\sqrt{(\boldsymbol{\mu_0}/2\boldsymbol{\omega})}$ (cf. Equation (2.4.1)). Upon conversion back into the time domain, the output is intercept $\boldsymbol{\tau}$ versus the square root of conductivity $\sqrt{(1/\boldsymbol{\rho})}$, and can be displayed as $\boldsymbol{\tau}$ versus $\boldsymbol{\rho}$.

Since EM-Radon is a modification of SURADON, I will start by describing the computations in SURADON. In order to reduce computational effort, Anderson (1993) configures the transform so that the least-squares equations for the discrete inverse Radon transform form a Hermitian Toeplitz (shift invariant) system, solvable by a complex form of Levinson recursion.

Following Foster and Mosher (1992), this is not always true for a forward transform unless the receiver positions are regular. Therefore we begin with an expression for the discrete inverse Radon transform:

$$f\left(x_l,t\right)=\sum_{k=0}^{n_p-1}F\left(p_k,t-p_k g\left(x_l\right)\right)\delta p \qquad \left\{l=0,...,n_x-1\right\} \tag{4.3.1}$$

where f is the input data, F is the forward Radon transform of f, p is slowness, $t-pg\left(x\right)\equiv\tau$ is the time-intercept value, n_p is the number of slownesses p_k, n_x is the

number of offsets x_l, and δp is the (regular) offset spacing so that $p_k = p_0 + k\delta p$. The function $g(x)$ is user-defined: for linear transforms $g(x) = x$, for parabolic transforms $g(x) = x^2$, etc.

In the frequency domain, Equation (4.3.1) becomes a set of independent equations for each frequency. Applying the Fourier time transform with shift theorem (Bracewell, 1978):

$$\tilde{f}(x_l, \omega) = \sum_{l=0}^{n_x - 1} \tilde{F}(p_k, \omega) e^{i\omega p_k g(x_l)} \delta p \quad \{l = 0, ..., n_x - 1\} \tag{4.3.2}$$

where tildes denote Fourier transforms ($+i\omega t$ has been used in the Fourier transform). Expressing this in matrix form:

$$\underset{\rightarrow}{\tilde{f}}(x, \omega) = \underline{B}(\omega) \underset{\rightarrow}{\tilde{F}}(p, \omega) \tag{4.3.3}$$

where, at each frequency, $\underline{B}$ is an n_p by n_x matrix with elements $B_{kl} = e^{i\omega p_k g(x_l)} \delta p$, $\underset{\rightarrow}{\tilde{f}}$ is a vector with n_x elements, $\underset{\rightarrow}{\tilde{F}}$ is a vector with n_p elements, and the summation in Equation (4.3.2) is accomplished by the implied sum over the repeated index l in the matrix multiplication. Then the least-squares inversion formula for the frequency-domain Radon transform is:

$$\underset{\rightarrow}{\tilde{F}}(p, \omega) = \left(\underline{B}^{\dagger} \underline{B}\right)^{-1} \underline{B}^{\dagger} \underset{\rightarrow}{\tilde{f}}(x, \omega) \tag{4.3.4}$$

where the † denotes complex conjugate transpose. Since the slowness increment δp is constant, $\underline{C} \equiv \left(\underline{B}^{\dagger} \underline{B}\right)$ is shift invariant (Toeplitz), and can be written (Anderson, 1993):

$$C_{mk} = \sum_{l=0}^{n_x - 1} e^{i\omega(p_k - p_m) g(x_l)} = \sum_{l=0}^{n_x - 1} e^{i\omega(k-m)\delta p g(x_l)} \tag{4.3.5}$$

SURADON utilizes Equation (4.3.5) to compute $\tilde{\vec{F}}$ in Equation (4.3.4), and then forms the desired Radon transform by taking the inverse Fourier time transform of $\tilde{\vec{F}}$ (using $-i\omega t$ in the inverse Fourier transform).

To produce EM-Radon, SURADON is modified by replacing slowness, at each frequency, with the formula for EM plane-wave phase slowness (*cf.* equation (2.4.1), above):

$$p_k = \sqrt{\frac{\mu_0}{2\omega\rho_k}} \tag{4.3.6}$$

where the n_p user-input resistivity values $\sqrt{(1/\rho_k)}$ now replace the slowness values and a uniform increment $\delta\sqrt{\frac{1}{\rho}}$ replaces the slowness increment, through a simple division by $\sqrt{\frac{\mu_0}{2\omega}}$. Applying the uniform increment restriction:

$$\sqrt{\frac{1}{\rho_k}} = \sqrt{\frac{1}{\rho_{\max}}} + k\cdot\delta\sqrt{\frac{1}{\rho}} \tag{4.3.7}$$

the components of C become:

$$C_{mk} = \sum_{l=0}^{n_x-1} e^{i\sqrt{\frac{\mu_0\omega}{2}}\left(\sqrt{\frac{1}{p_k}}-\sqrt{\frac{1}{p_m}}\right)g(x_l)} = \sum_{l=0}^{n_x-1} e^{i\sqrt{\frac{\mu_0\omega}{2}}(k-m)\delta\sqrt{\frac{1}{\rho}}g(x_l)} \tag{4.3.8}$$

Of course, this makes a non-uniform decrement in resistivity, which is accommodated in the displays, following the computation.

Now, utilizing Equation (4.3.5) to compute $\tilde{\vec{F}}$, and taking its inverse Fourier time transform, produces a Radon $\tau-\sqrt{1/\rho}$ transform, replacing the Radon $\tau-p$ transform familiar in seismology; hence, we call it the EM-Radon transform.

4.4 Example of Radon resistivity transforms

Figure 4.4.1 presents a comparison of Radon resistivity (called "EM-Radon") transforms for the Canonical Model without and with reservoir.

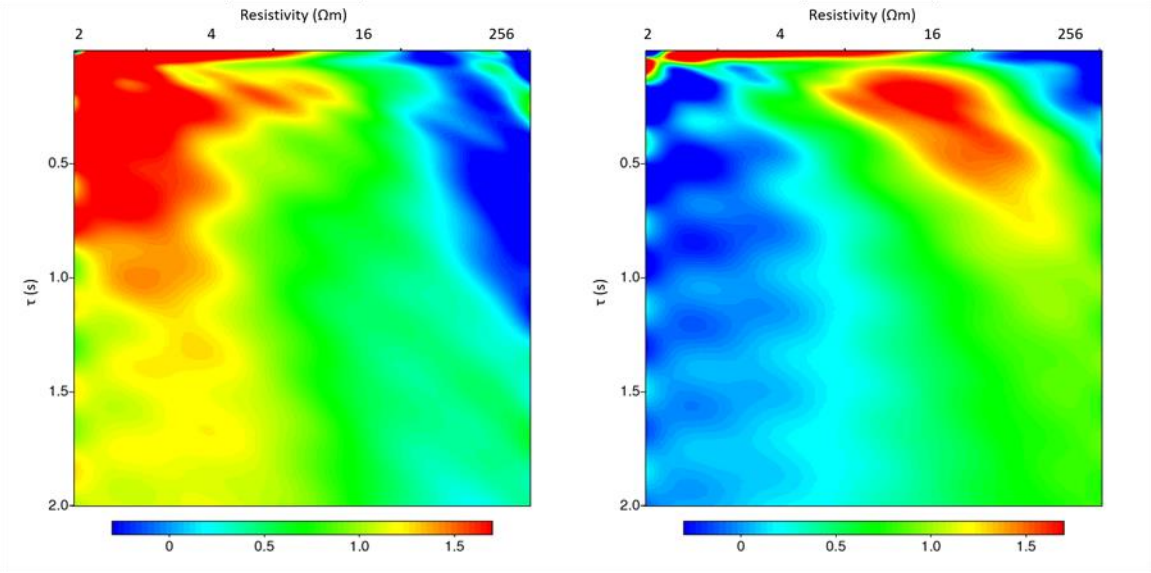

a) Canonical w/o reservoir *b) Canonical Model*

Figure 4.4.1: Comparison of EM-Radon of normalized inline horizontal electric field amplitude for Canonical Model w/o and with reservoir [normalized volts/meter].

The Canonical Model transform (on the right) shows resistivities at early times in the 8 to 100 Ωm range, while the model without reservoir (on the left) does not. Smearing of the 100 Ωm resistivity amplitude probably results from the spectrum of incidence angles as well as spreading of the reservoir lateral wavelet with offset. Note that the Turner (1990) anti-aliasing criteria (see Appendix D.2) suggest a low level of resistivity resolution, on the order of 10 Ωm at 1 Hz.

4.5 Time and offset gating of Radon resistivity transform

The EM-Radon transform may be more effective when applied to data that is offset-gated to exclude the near-field response where the reservoir lateral wave has not yet become

dominant, and to exclude the very far-field where the air wave becomes dominant. Similarly, it may be helpful to exclude early times when the reservoir lateral wave is dominated by the ocean-bottom sediment lateral wave. Figure 4.5.1 shows the time and offset gates overlaid on plots of the base model without and with the reservoir. These gates are easily identified on this model data, and may also be identifiable in field data.

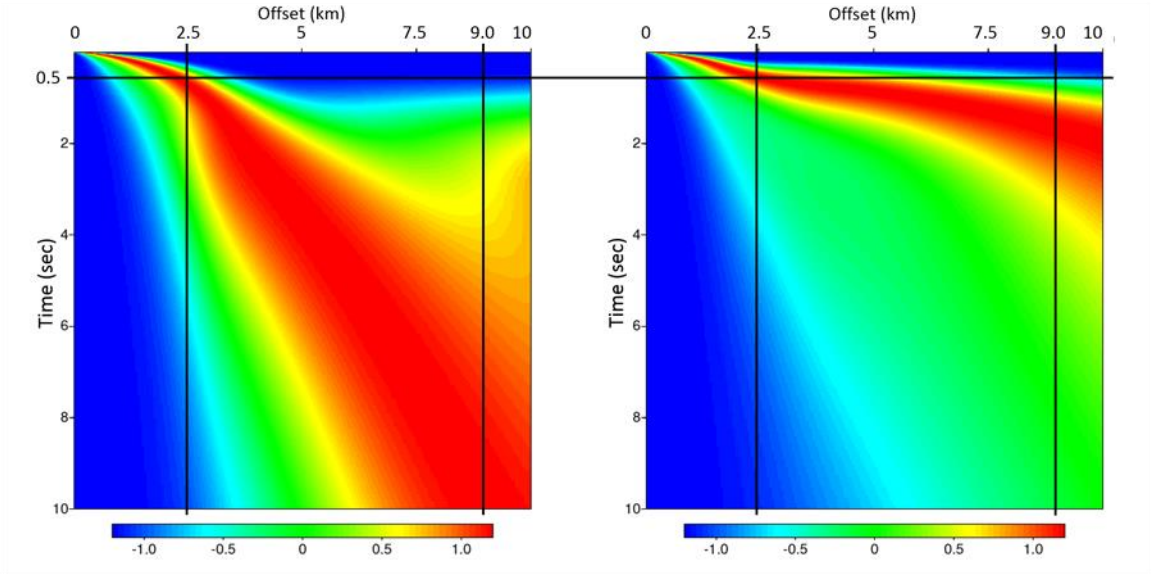

a) Canonical w/o reservoir *b) Canonical Model*

Figure 4.5.1: Time and offset gating of normalized inline horizontal electric field amplitude for Canonical Model without and with reservoir [normalized volts/meter].

Figure 4.5.2 shows the EM-Radon comparison for the time- and offset-gated models. It appears that the resistivity in the model with reservoir (Figure 4.5.1b) is now closer to the 100 Ωm of the input model, than without gating (Figure 4.4.1b). For the model without reservoir, resistivity is low and relatively diffuse, in either case.

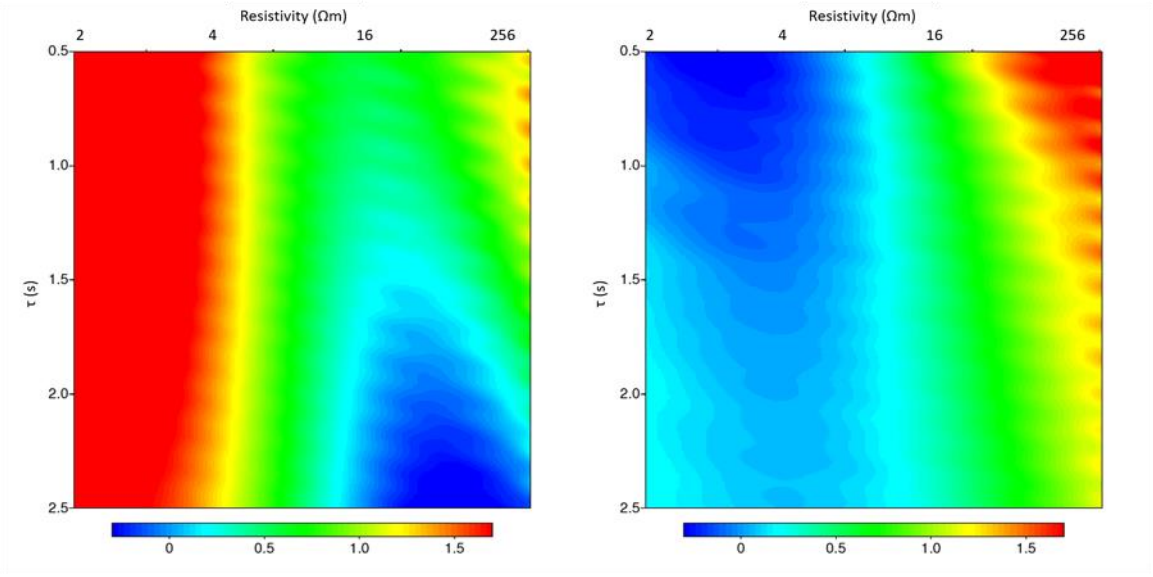

a) Canonical w/o reservoir *b) Canonical Model*

Figure 4.5.2: Comparison of EM-Radon of normalized inline horizontal electric field amplitude for time- and offset-gated Canonical Model without and with reservoir [normalized volts/meter].

5 Robustness of EM-Radon transform to noise

5.1 Noise in CSEM surveys

A recent overview of noise in CSEM surveys is provided by Connell and Key (2013) where complete noisy electric field data $\tilde{E}$ is comprised of relative and additive noise components:

$$\tilde{E} = E_r E + E_a \tag{5.1.1}$$

Here, errors in transmitter and receiver orientations and locations, and variable sensor calibrations are often said to scale with measurement; hence, they are modeled as relative to the field intensity E via the multiplicative constant E_r. The additive component E_a is termed the "absolute electric field response noise" and is frequency-dependent:

$$E_a(f) = \frac{E_i(f) + \frac{V_r(f)}{l_r}}{l_s IS(f)\sqrt{N}} \tag{5.1.2}$$

where E_i is the environmental noise induced by magnetotelluric signal, water currents, and tides, V_r is the voltage noise spectrum for the recording system, l_r is the length of the receiver antenna, l_s is the length of the transmitter antenna, IS is the current intensity of the transmitter, and N is the window stack length.

In order to test the robustness of EM-Radon to noise, the complete noisy electric field is simplified by ignoring the relative noise E_r and environmental noise E_i components. N is set to unity since there is no stacking involved in this thesis. Equation (5.1.2) simplifies to:

$$E_a(f) = \frac{V_r(f)}{l_r l_s IS(f)} \tag{5.1.3}$$

This is the electric-field noise floor given by Constable and Weiss (2006). According to Mittet and Morten (2012), at frequencies above 0.1 Hz, recording system technology can currently limit receiver self-noise fluctuations to amplitudes below 10^{-10} V/m. Following the lead of Houck *et al.* (2013), the receiver and transmitter lengths are assumed to be 8 m and 300 m, respectively, and the transmitter current intensity is assumed to be 3 kA, over all relevant frequencies. These assumptions produce the oft-employed noise floor $E_a = 10^{-15}$ V/m.

5.2 Robustness to additive noise

Figure 5.2.1a where there is no additive noise, is to be compared to Figure 5.2.1b where noise of amplitude 10^{-15} V/m has been added, to Figure 5.2.1c where 10^{-14} V/m noise has been added, and to Figure 5.2.1d where 10^{-13} V/m noise has been added. The noise is added to the raw synthetic data, prior to the trace normalization. Ability to identify the reservoir deteriorates when the magnitude of random additive noise exceeds 10^{-13} V/m, well above the noise floor discussed in Section 5.1; see Figure 2.5.1d.

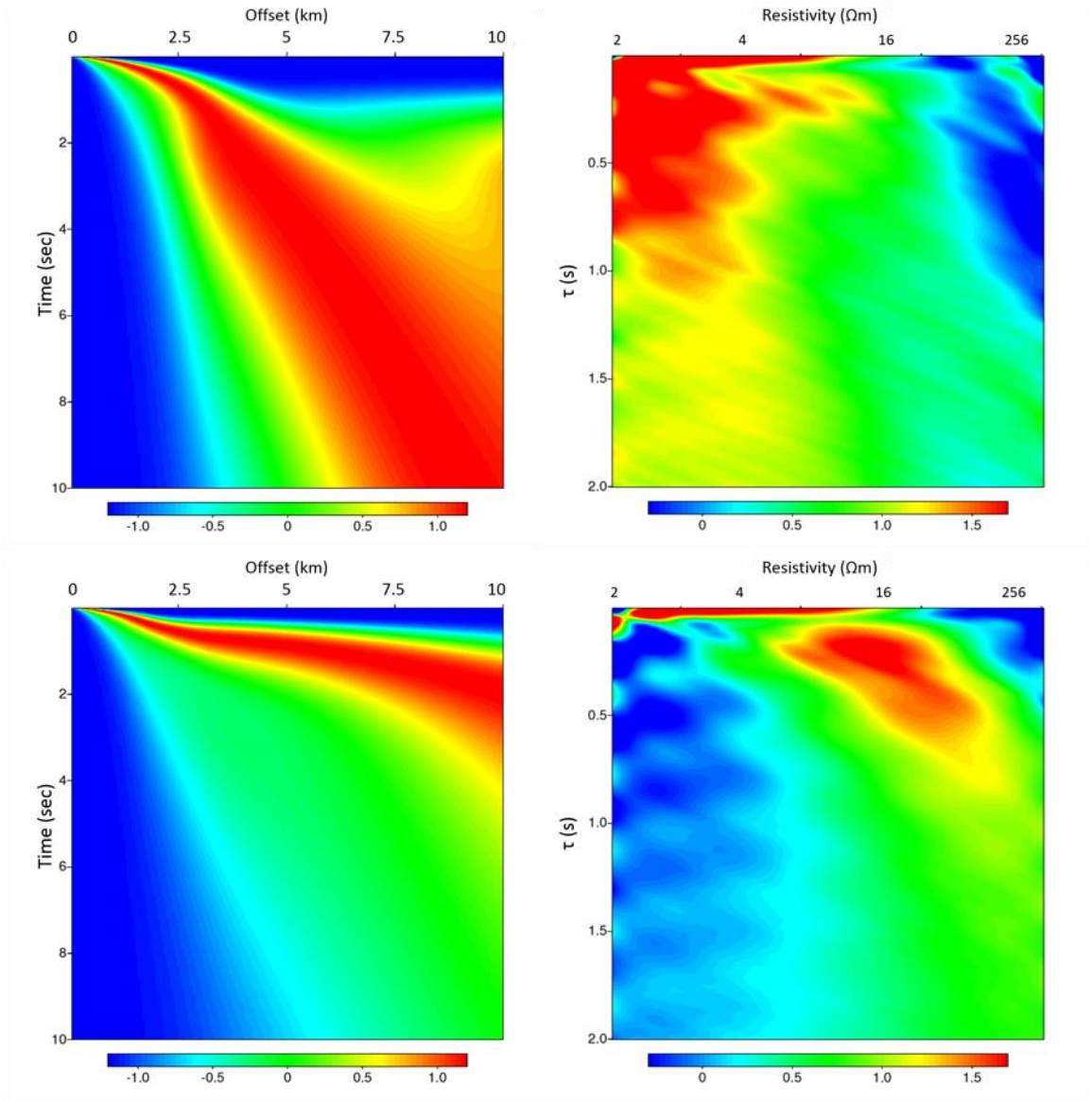

a) Base Model (no noise)

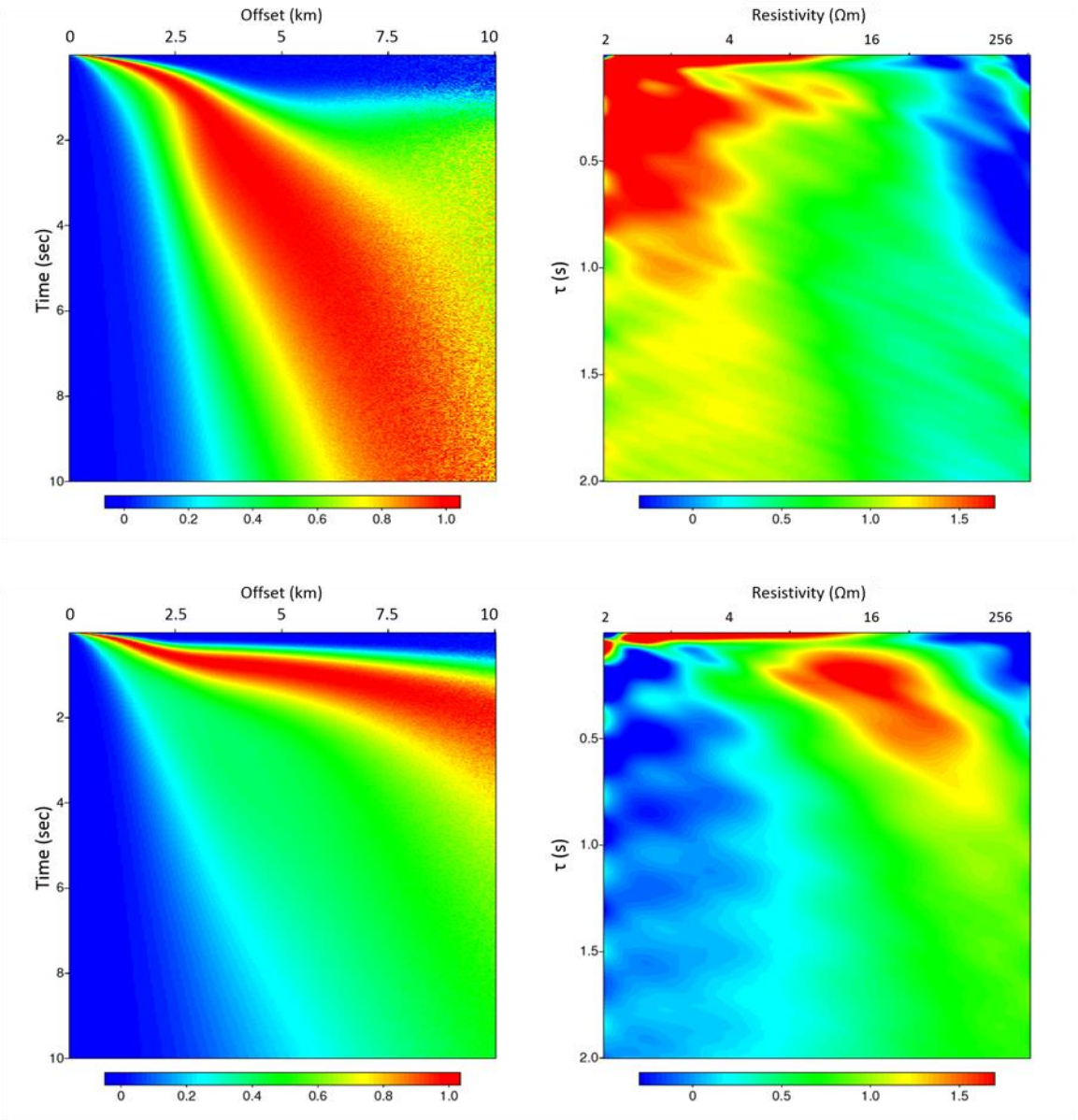

b) 10^{-15} V/m noise added

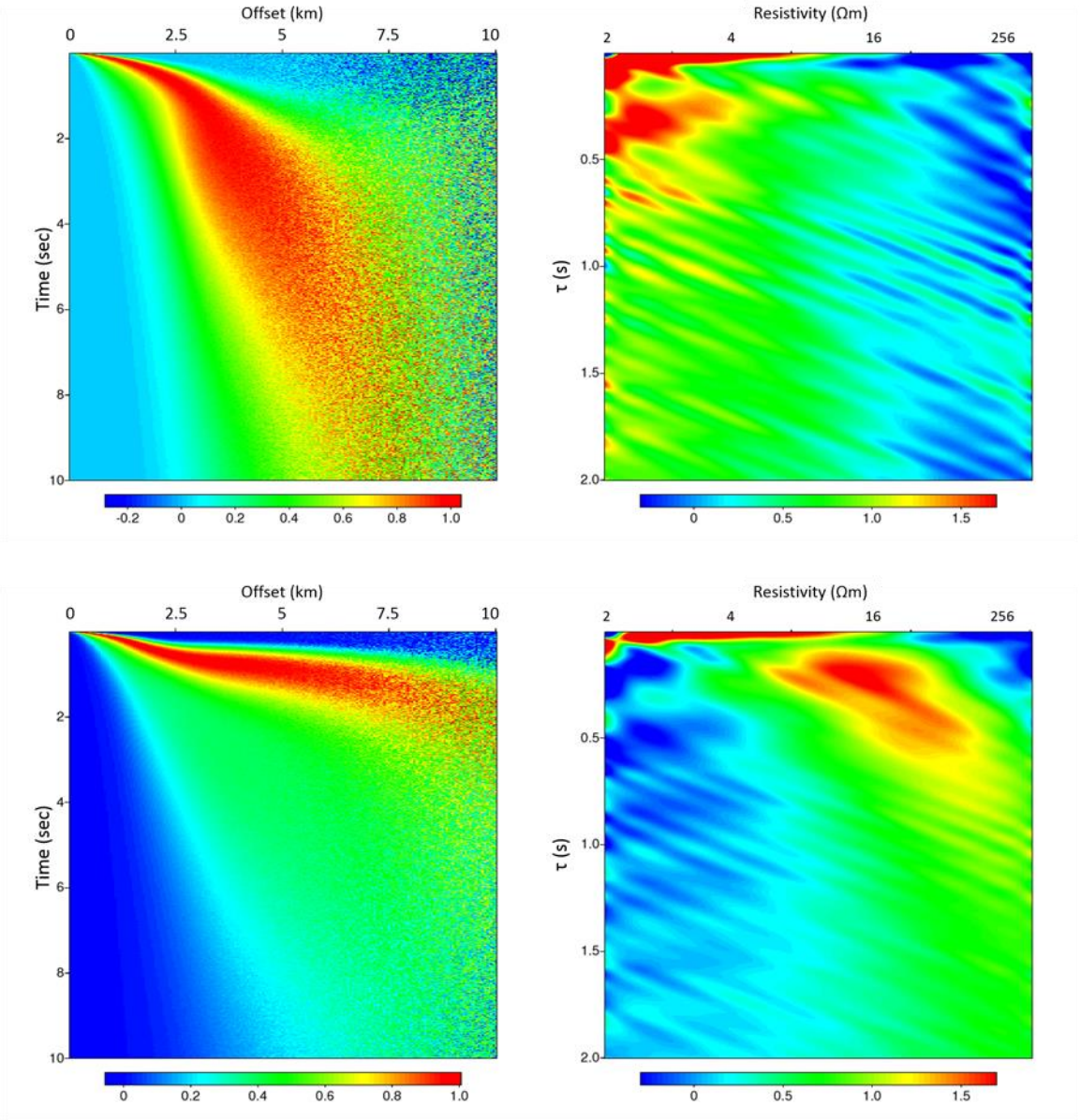

c) 10^{-14} V/m noise added

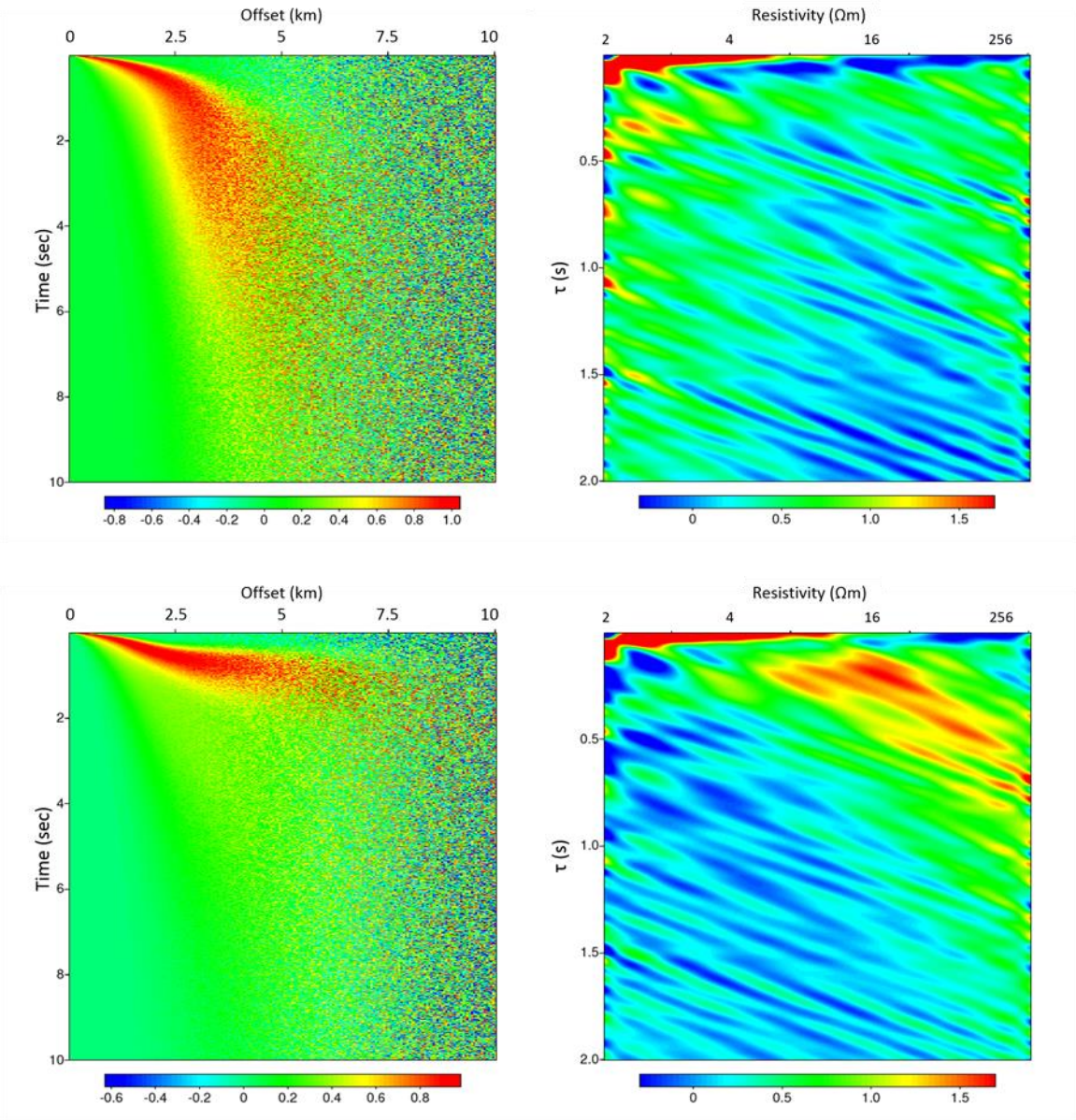

d) 10^{-13} V/m noise added

(For each image set: top left – normalized inline horizontal electric field amplitude for Canonical Model w/o reservoir, top right – EM-Radon for Canonical model w/o reservoir; bottom left – normalized inline horizontal electric field amplitude for Canonical Model, bottom right – EM-Radon for Canonical Model [normalized volts/meter for all images].)

Figure 5.2.1: Noise study EM-Radon Plots

6 EM-Radon decimation tests

6.1 Robustness to fewer receivers

Figure 6.1.1a (Canonical Model) with 200 receivers at 50 m spacing, is to be compared to Figure 6.1.1b where the data are spatially decimated with 100 receivers at 100 m spacing, to Figure 6.1.1c with 50 receivers at 200 m spacing, to Figure 6.1.1d with 25 receivers at 400 m spacing, to Figure 6.1.1e with 12 receivers at 800 m spacing, and to Figure 6.1.1f with 6 receivers at 1600 m spacing. Ability to identify the reservoir and its resistivity is not very sensitive to receiver spacing since wavelengths in the reservoir are long enough relative to the tested spacing range. This is an important conclusion because the density of spacing of the receivers is an issue of some economic importance in real data acquisition. However, it may well be modified for more realistic models with finite lateral dimensions.

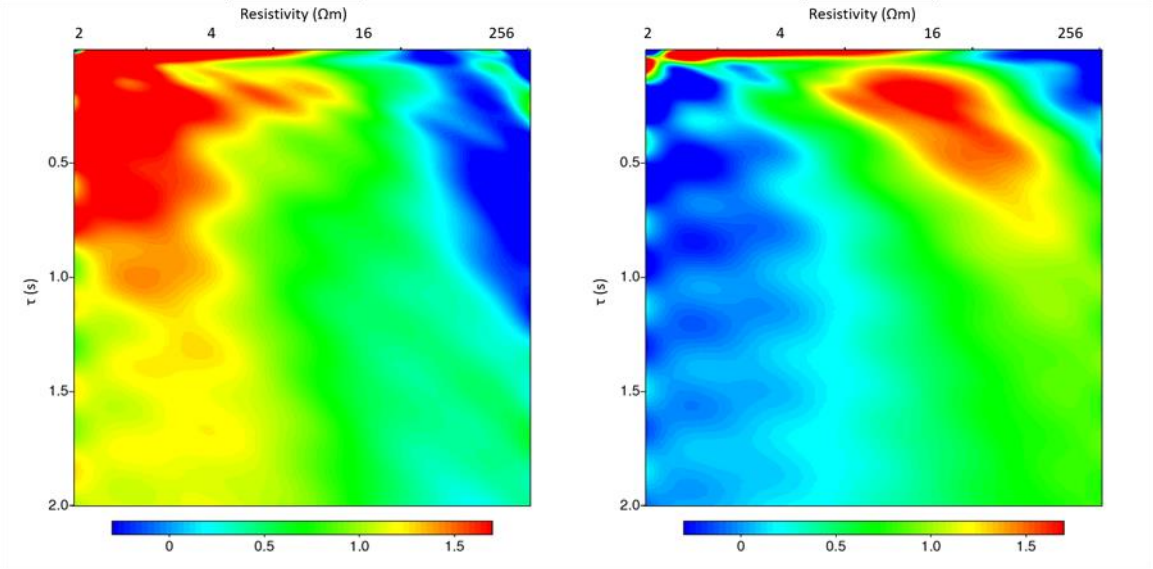

a) Base Model – 50 m receiver spacing

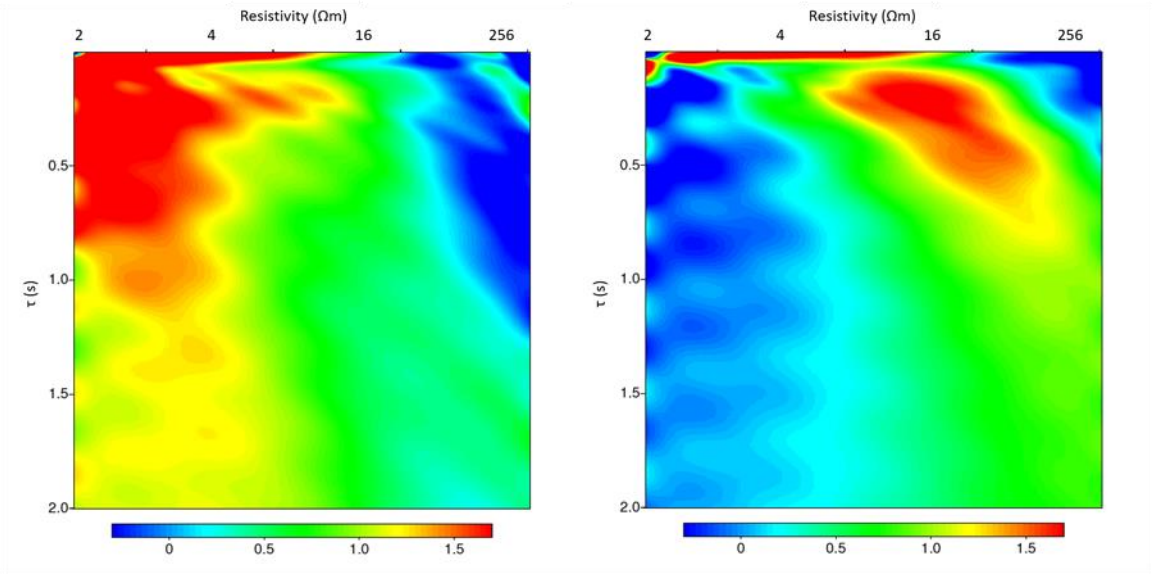

b) 100 m receiver spacing

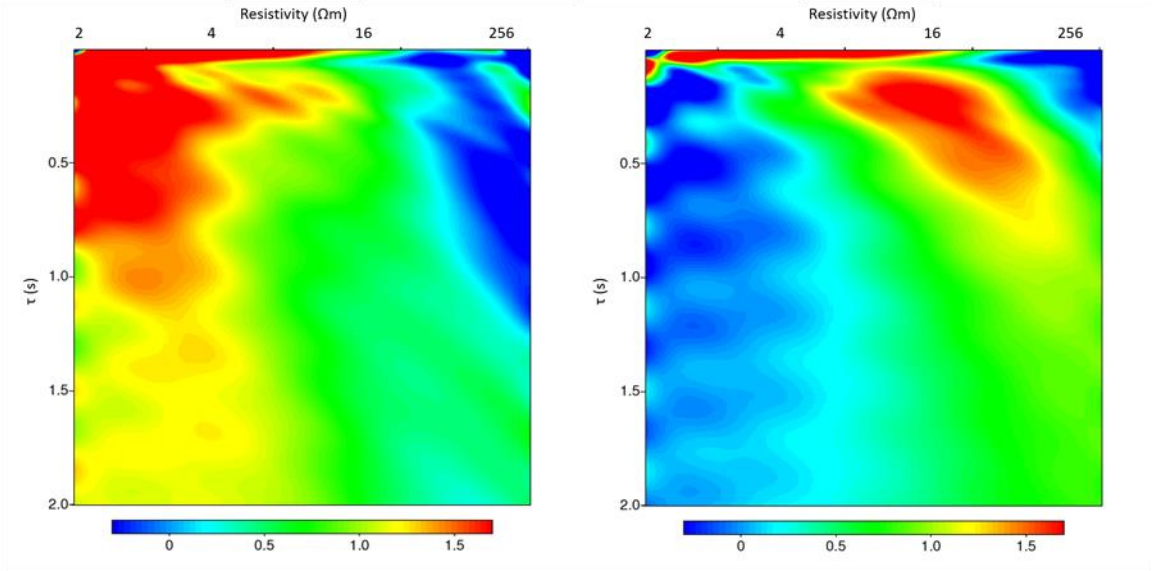

c) 200 m receiver spacing

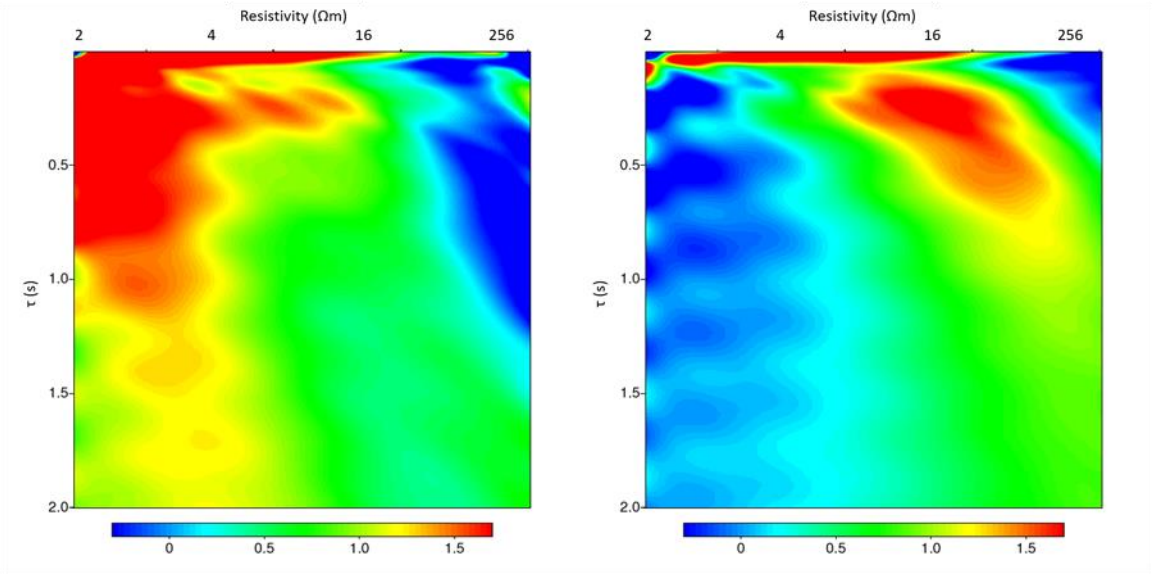

d) 400 m receiver spacing

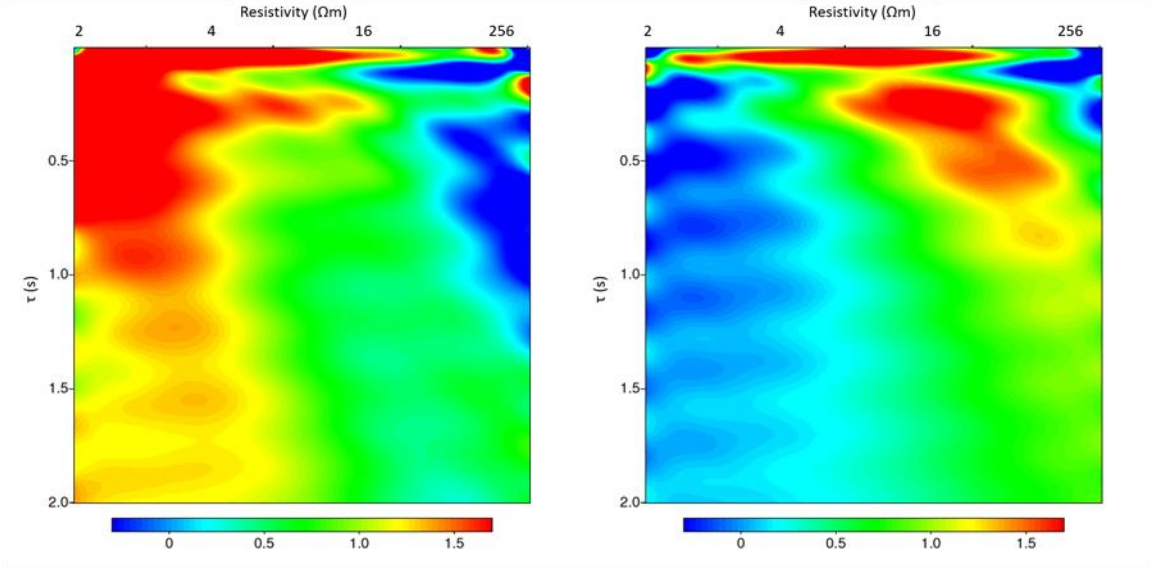

e) 800 m receiver spacing

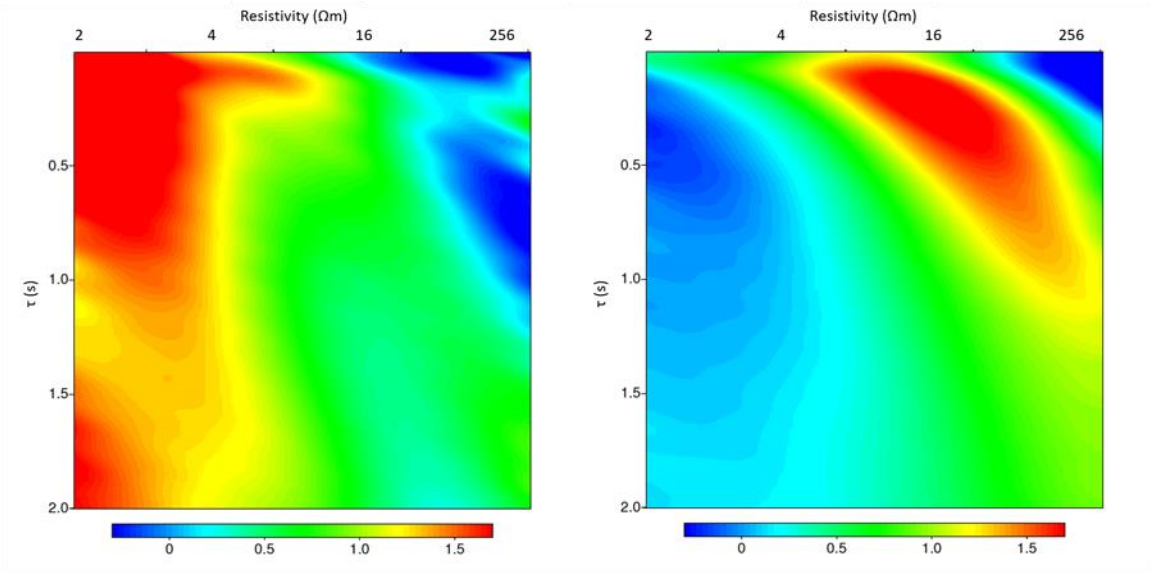

f) 1600 m receiver spacing

(For each image set: left – EM-Radon of normalized inline horizontal electric field amplitude for Canonical model w/o reservoir; right – EM-Radon of normalized inline electric field amplitude for Canonical Model [normalized volts/meter for all images].)

Figure 6.1.1: EM-Radon plots for various receiver spacings

6.2 Robustness to sparser time samples

Figure 6.2.1a (Canonical Model) with a 2 ms sampling interval, is to be compared to Figure 6.2.1b where the data are temporally decimated with sampling interval 4 ms, to Figure 6.2.1c where the sampling interval is 8 ms, to Figure 6.2.1d where the sampling interval is 16 ms, to Figure 6.2.1e where the sampling interval is 32 ms, and to Figure 6.2.1f where the sampling interval is 64 ms. Reservoir resistivity is not adversely affected at these sampling intervals since, even at 64 ms, Nyquist frequency (7.8 Hz) is at the upper range of frequency content in the data.

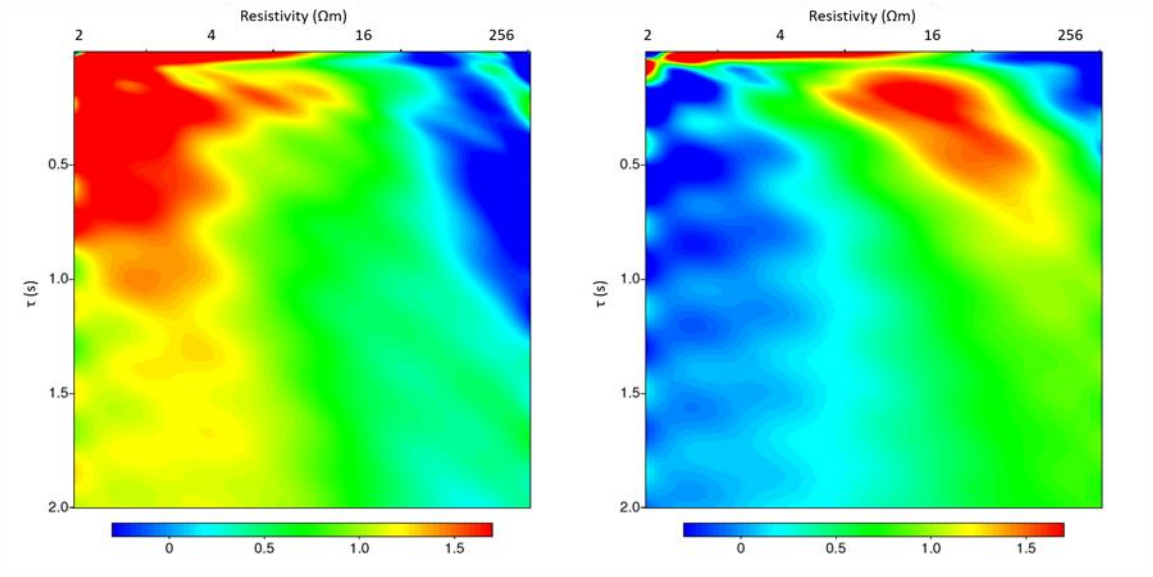

a) Base Model – 2 ms sampling interval

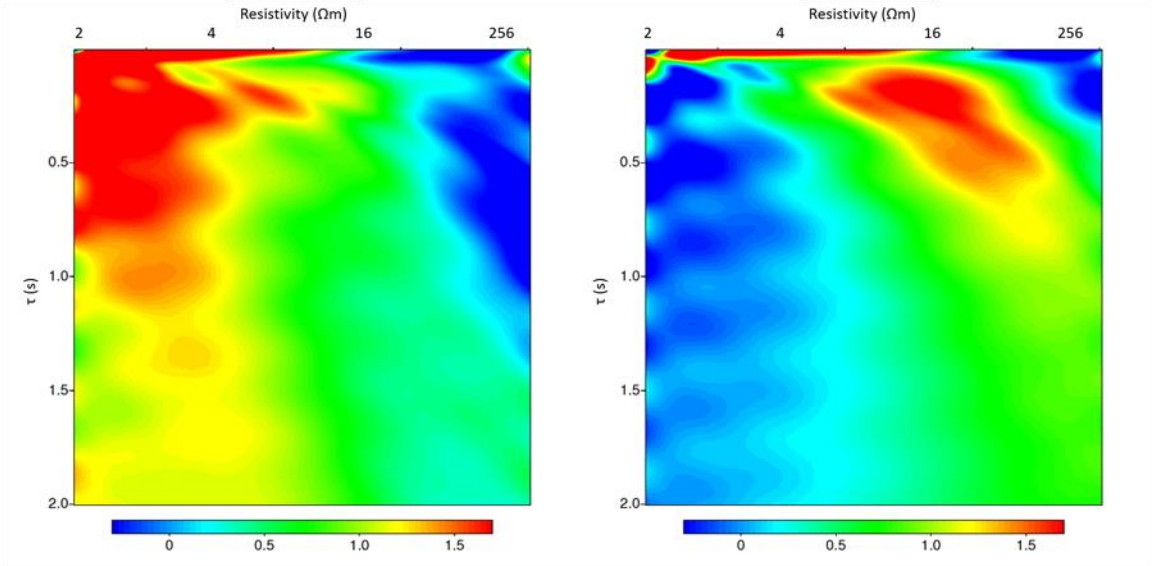

b) 4 ms sampling interval

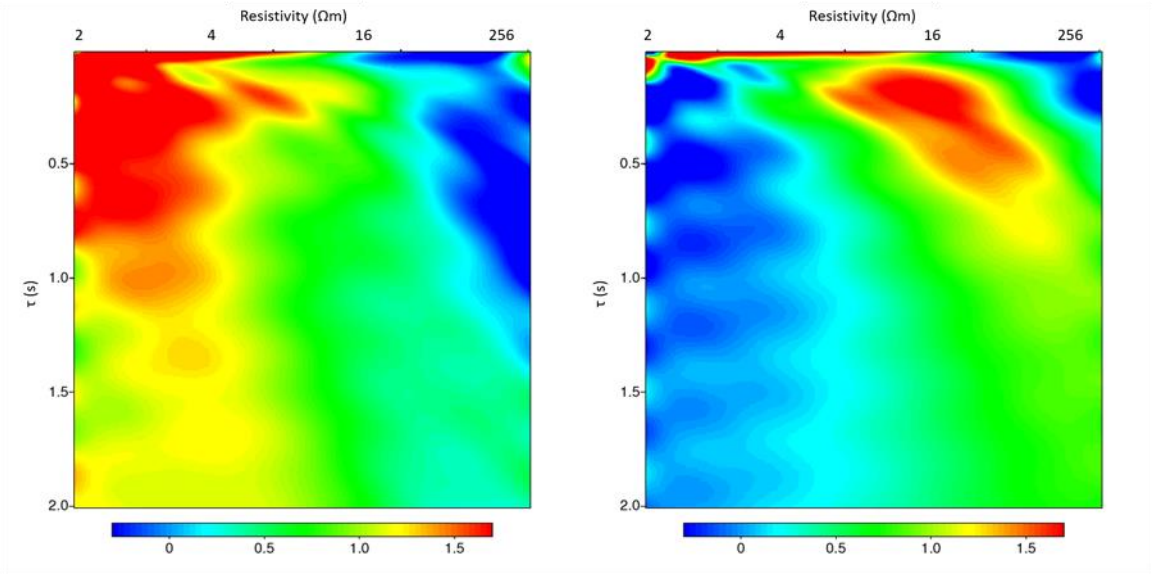

c) 8 ms sampling interval

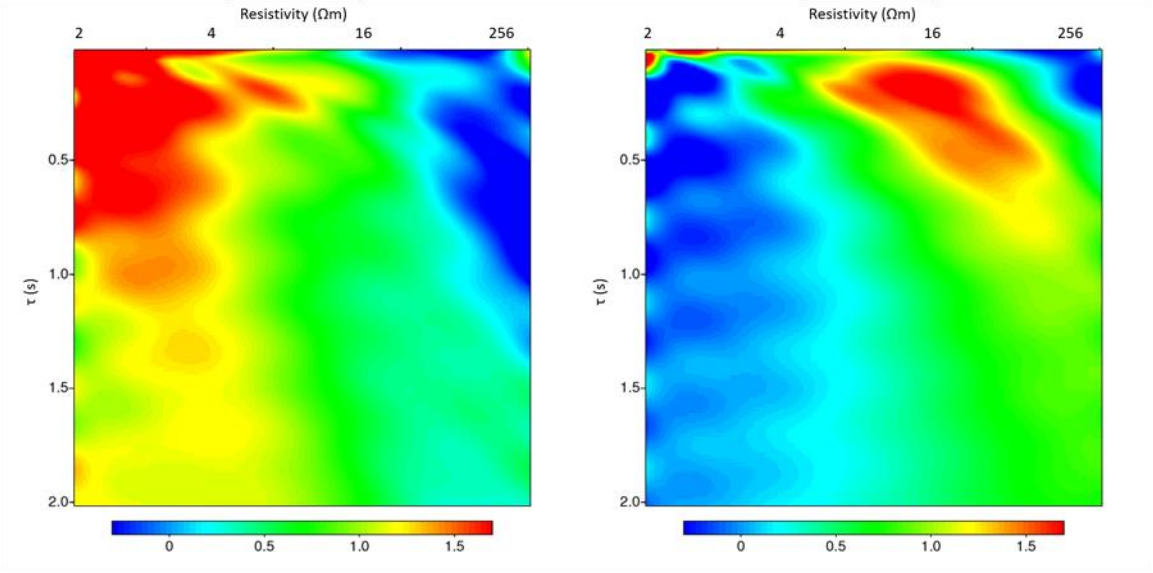

d) 16 ms sampling interval

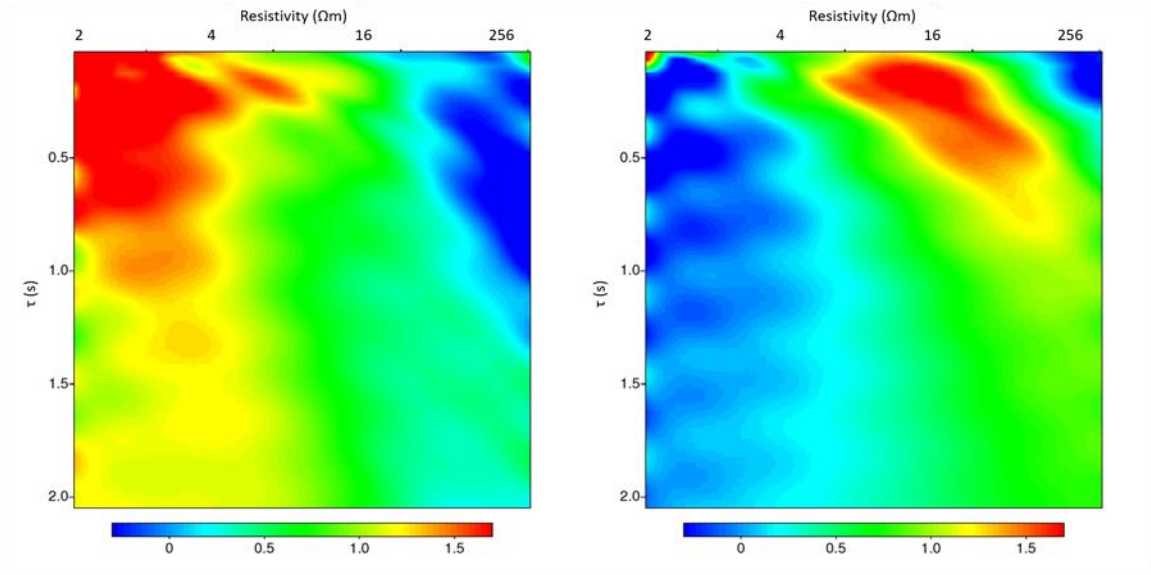

e) 32 ms sampling interval

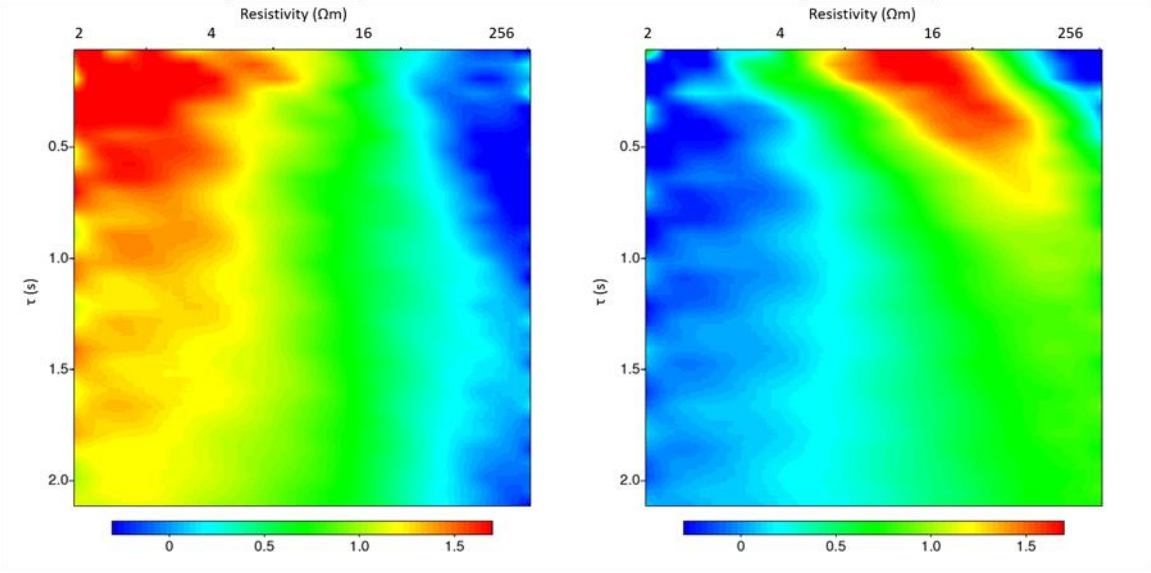

f) 64 ms sampling interval

(For each image set: left – EM-Radon of normalized inline horizontal electric field amplitude for Canonical model w/o reservoir; right – EM-Radon of normalized inline electric field amplitude for Canonical Model [normalized volts/meter for all images].)

Figure 6.2.1: EM-Radon plots for various sampling intervals

7 Sensitivity of EM-Radon transform to model variations

7.1 Sensitivity to depth of reservoir

Figure 7.1.1a (Canonical Model) where the reservoir lies below 1 km of sediment, is to be compared to Figure 7.1.1b where the model is modified such that the reservoir lies below 1.5 km of sediment, to Figure 7.1.1c where the reservoir lies below 2 km of sediment, and to Figure 7.1.1d where the reservoir lies below 2.5 km of sediment. Ability to identify the reservoir and its resistivity is preserved to 1.5 km but degrades fairly quickly thereafter.

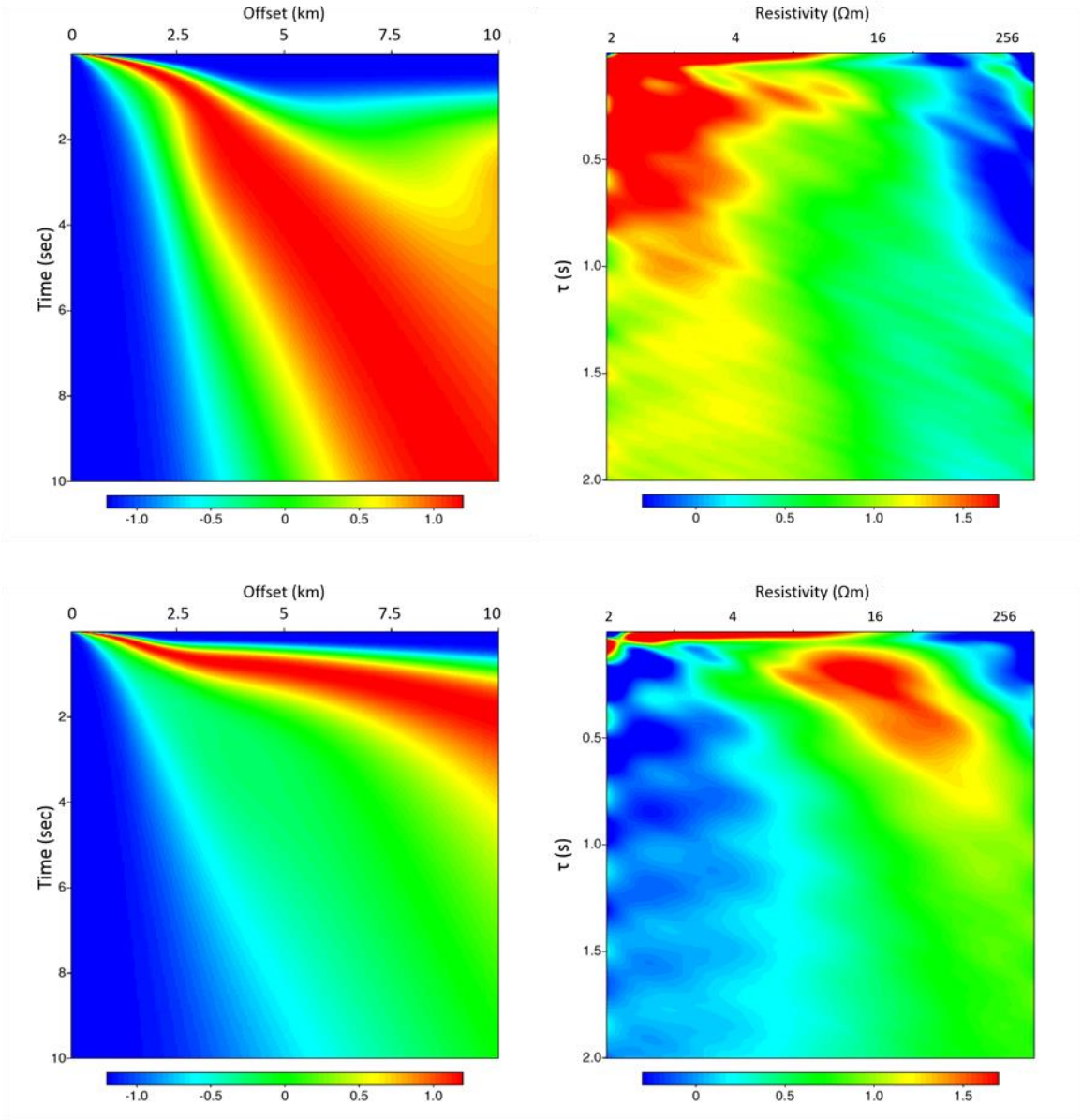

a) Base Model – 1 km thick sediments

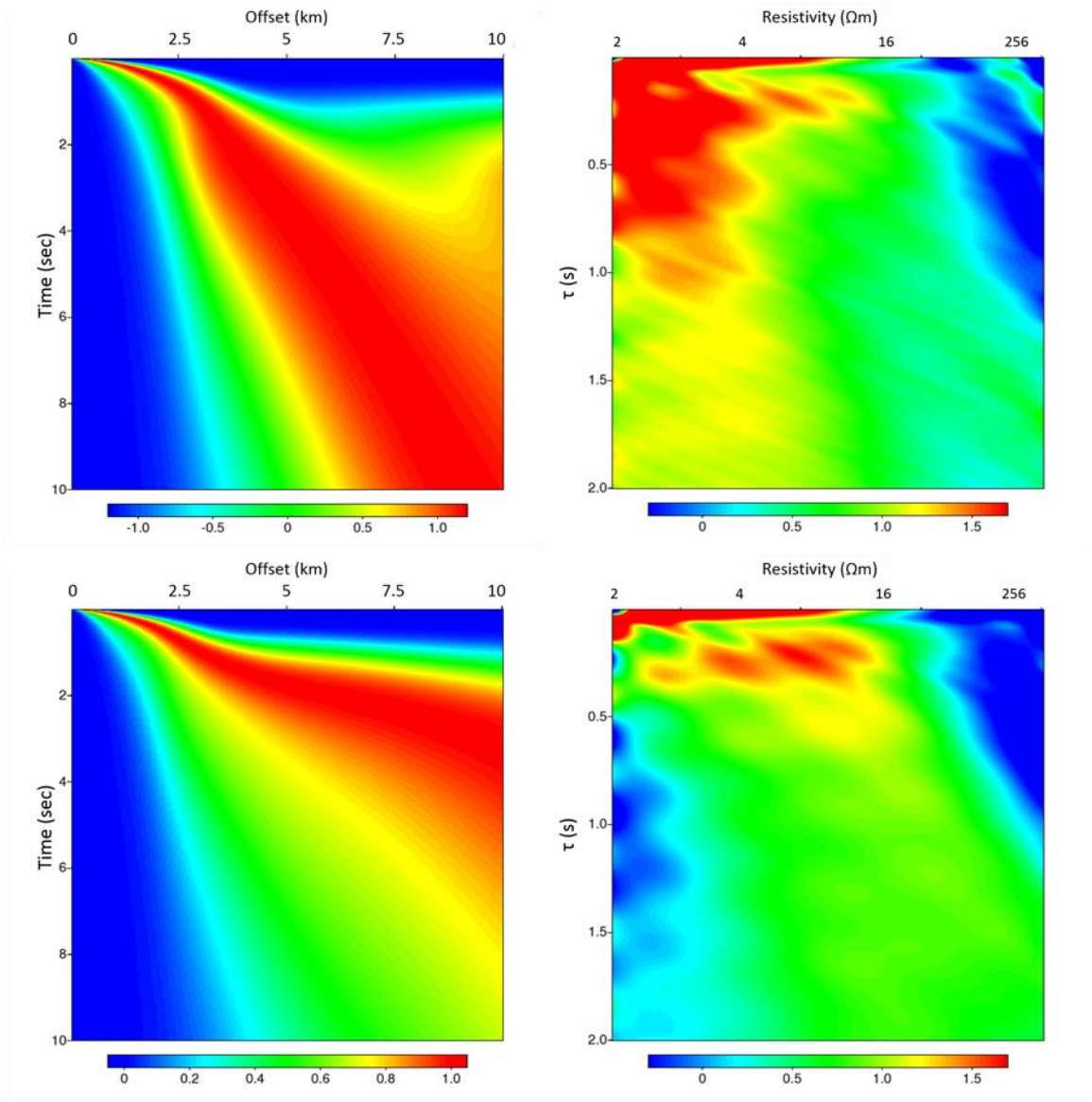

b) 1.5 km thick sediments

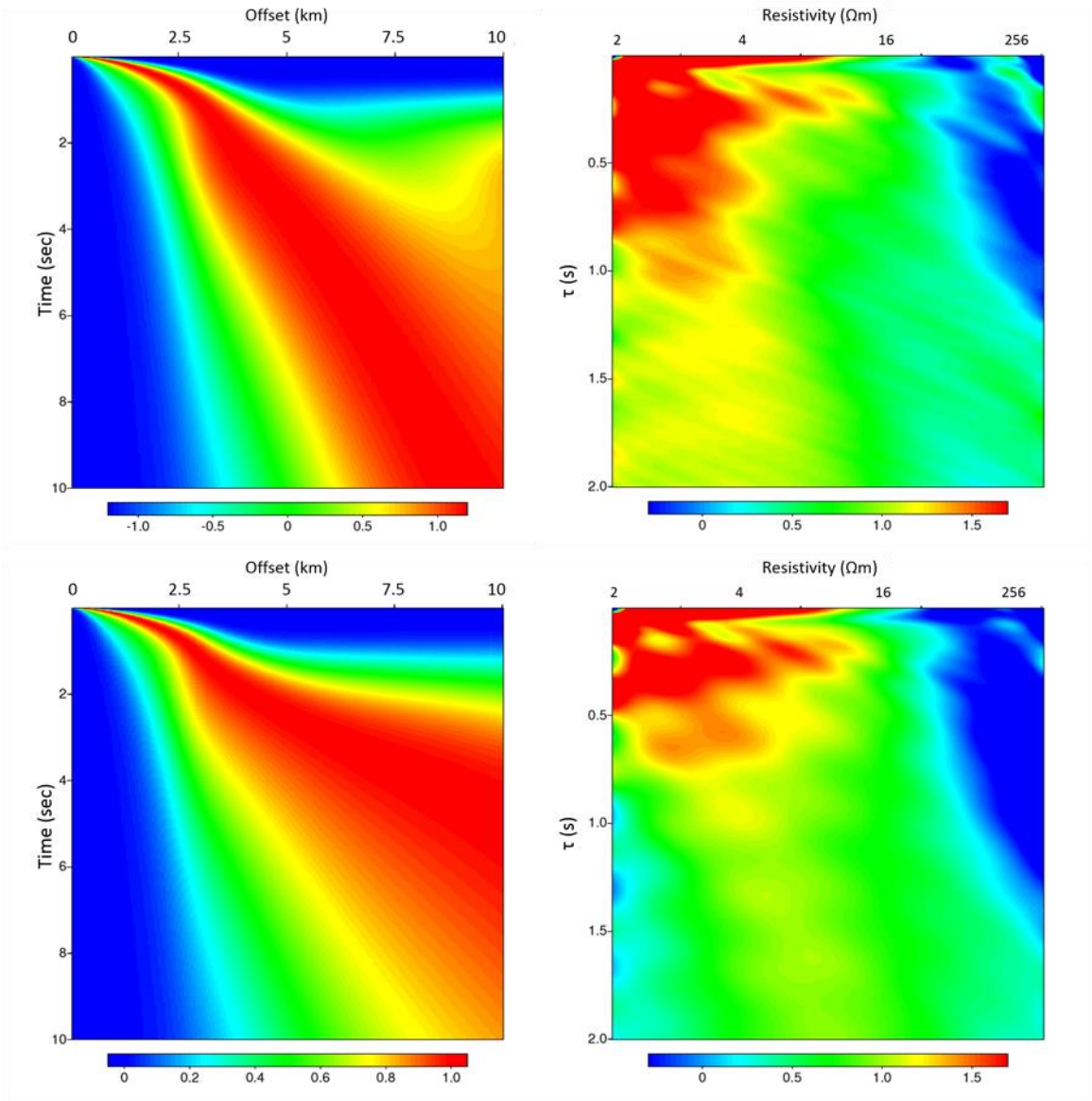

c) 2 km thick sediment

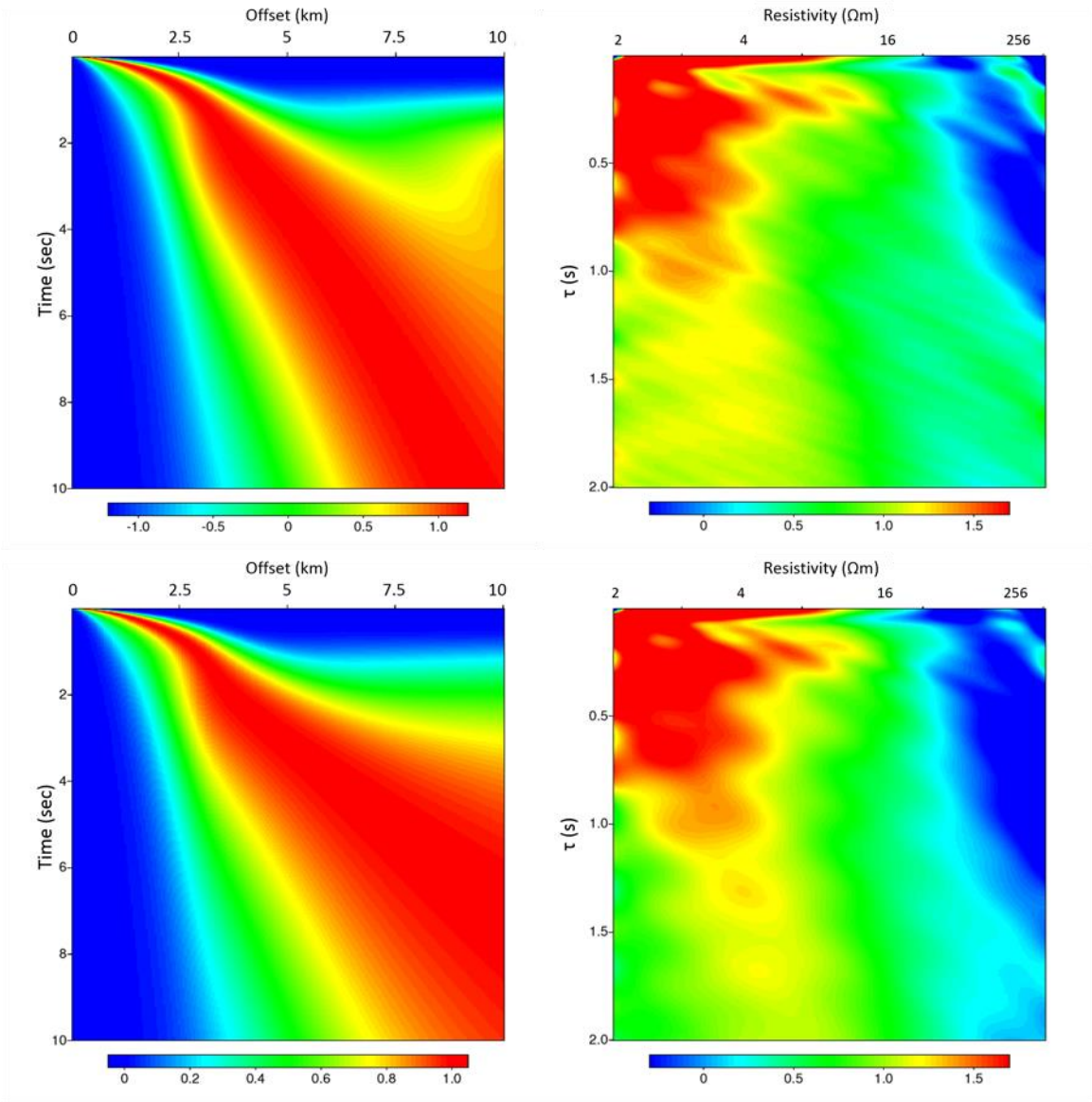

d) 2.5 km thick sediment

(For each image set: top left – normalized inline horizontal electric field amplitude for Canonical Model w/o reservoir, top right – EM-Radon for Canonical model w/o reservoir; bottom left – normalized inline horizontal electric field amplitude for Canonical Model, bottom right – EM-Radon for Canonical Model [normalized volts/meter for all images].)

Figure 7.1.1: EM-Radon plots for various thicknesses of sediment overburden

7.2 Sensitivity to thickness of reservoir

Figure 7.2.1a (Canonical Model) where the reservoir is 100 m thick, is to be compared to Figure 7.2.1b where the model is modified such that the reservoir is 50 m thick, and to Figure 7.2.1c where the reservoir is 25 m thick. Ability to identify the reservoir and its resistivity is somewhat preserved to 50 m but appears to degrade thereafter.

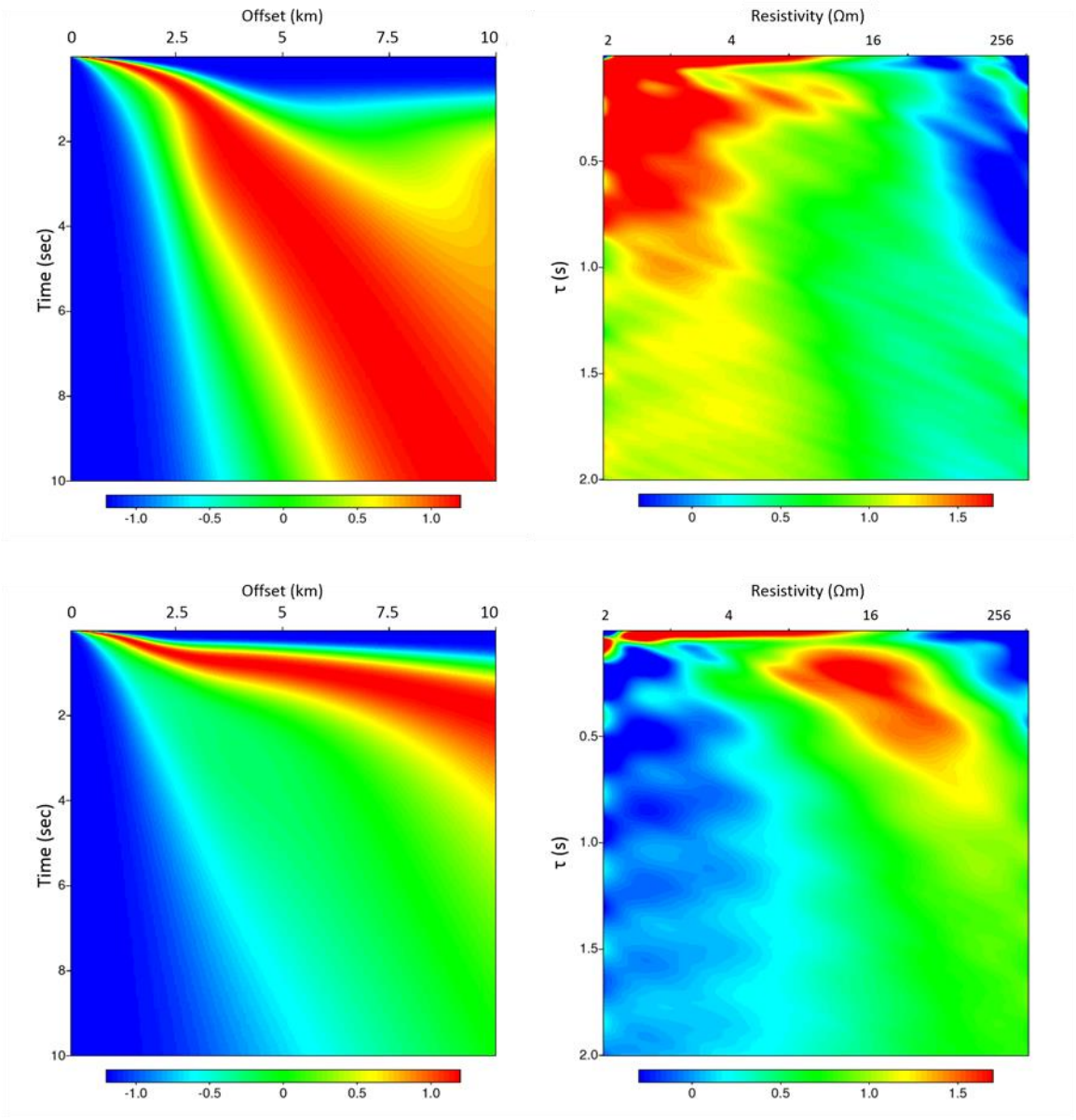

a) Base Model - 100 m thick reservoir

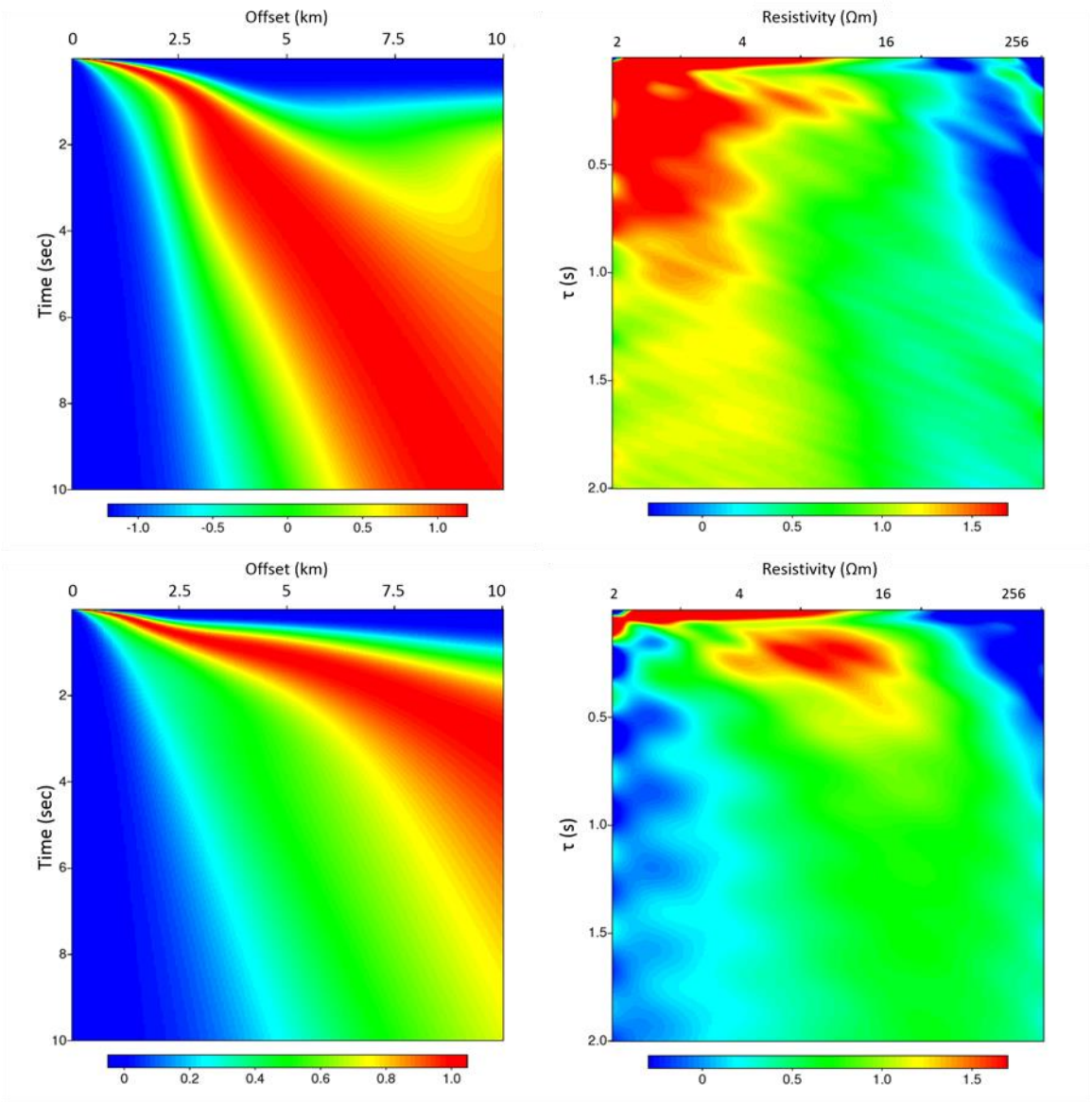

b) 50 m thick reservoir

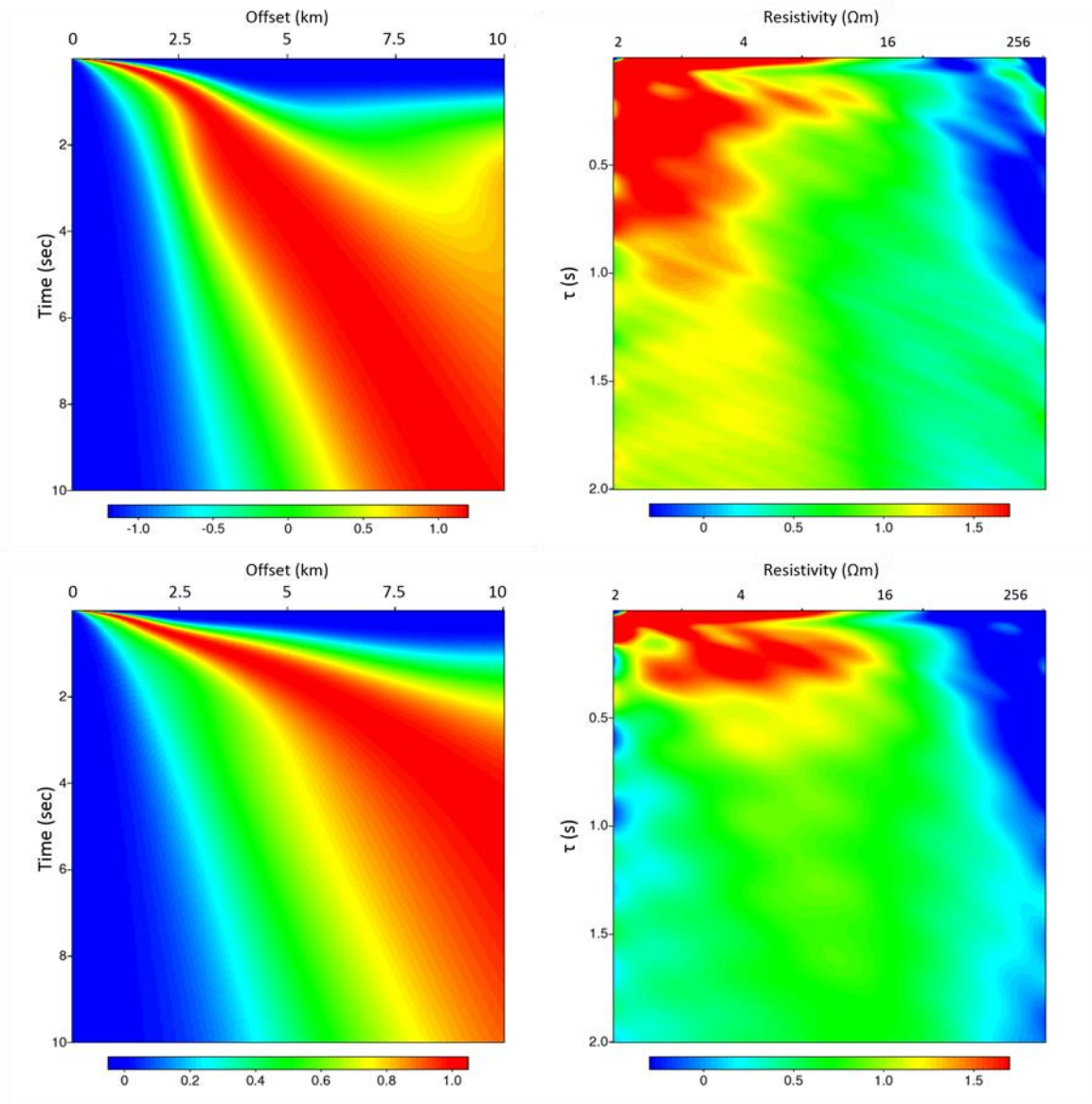

c) 25 m thick reservoir

(For each image set: top left – normalized inline horizontal electric field amplitude for Canonical Model w/o reservoir, top right – EM-Radon for Canonical model w/o reservoir; bottom left – normalized inline horizontal electric field amplitude for Canonical Model, bottom right – EM-Radon for Canonical Model [normalized volts/meter for all images].)

Figure 7.2.1: EM-Radon plots for various reservoir thicknesses

7.3 Sensitivity to resistivity of reservoir

Figure 7.3.1a (Canonical Model) with a 100 Ωm reservoir, is to be compared to Figure 7.3.1b where model is modified such that the resistivity is 75 Ωm, to Figure 7.3.1c where the resistivity is 50 Ωm, and to Figure 7.3.1d where the resistivity is 25 Ωm. Reservoir resistivity is smeared but it clearly reflects the decreasing trend in the simulated models.

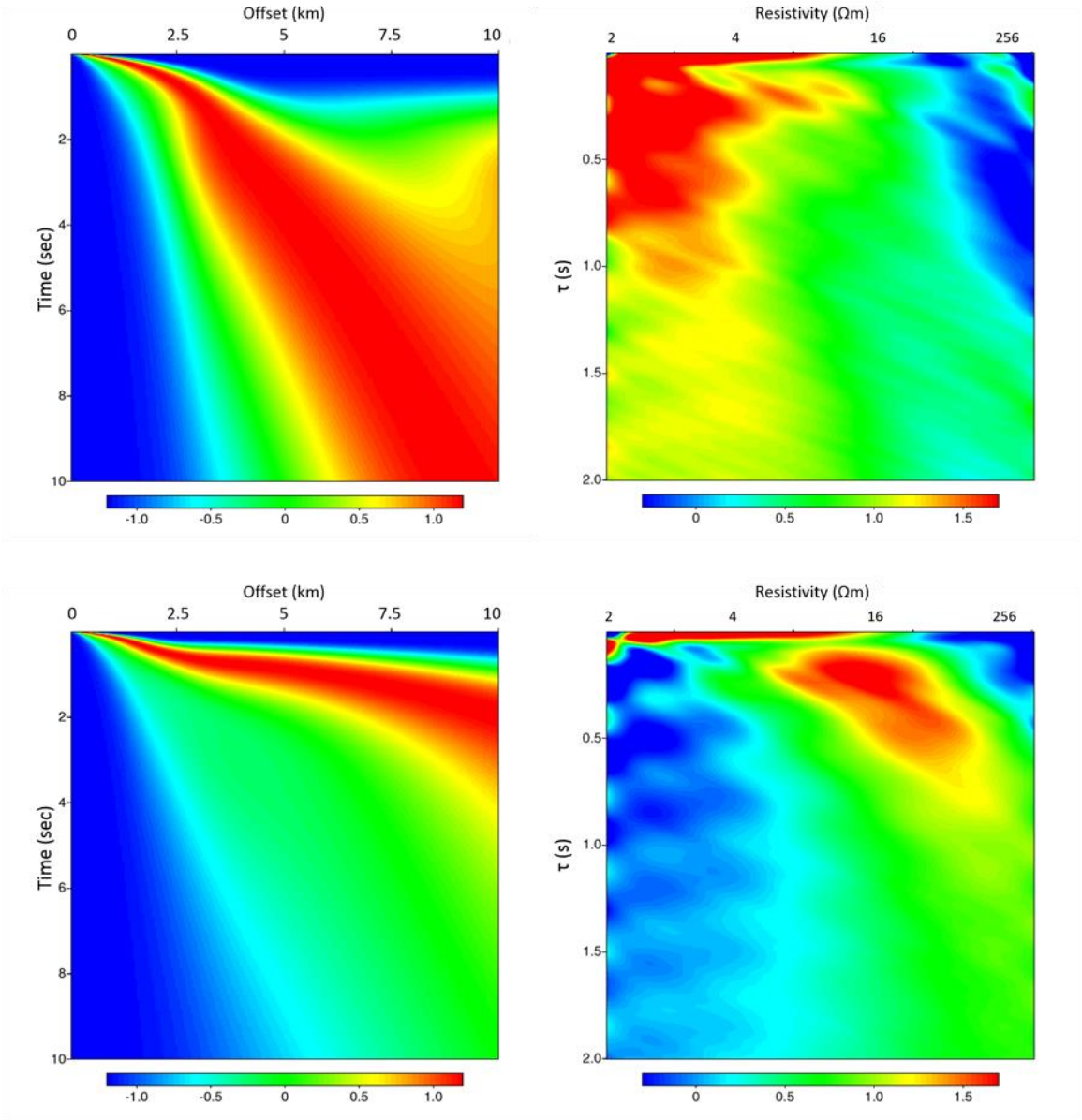

a) Base Model – 100 Ωm reservoir

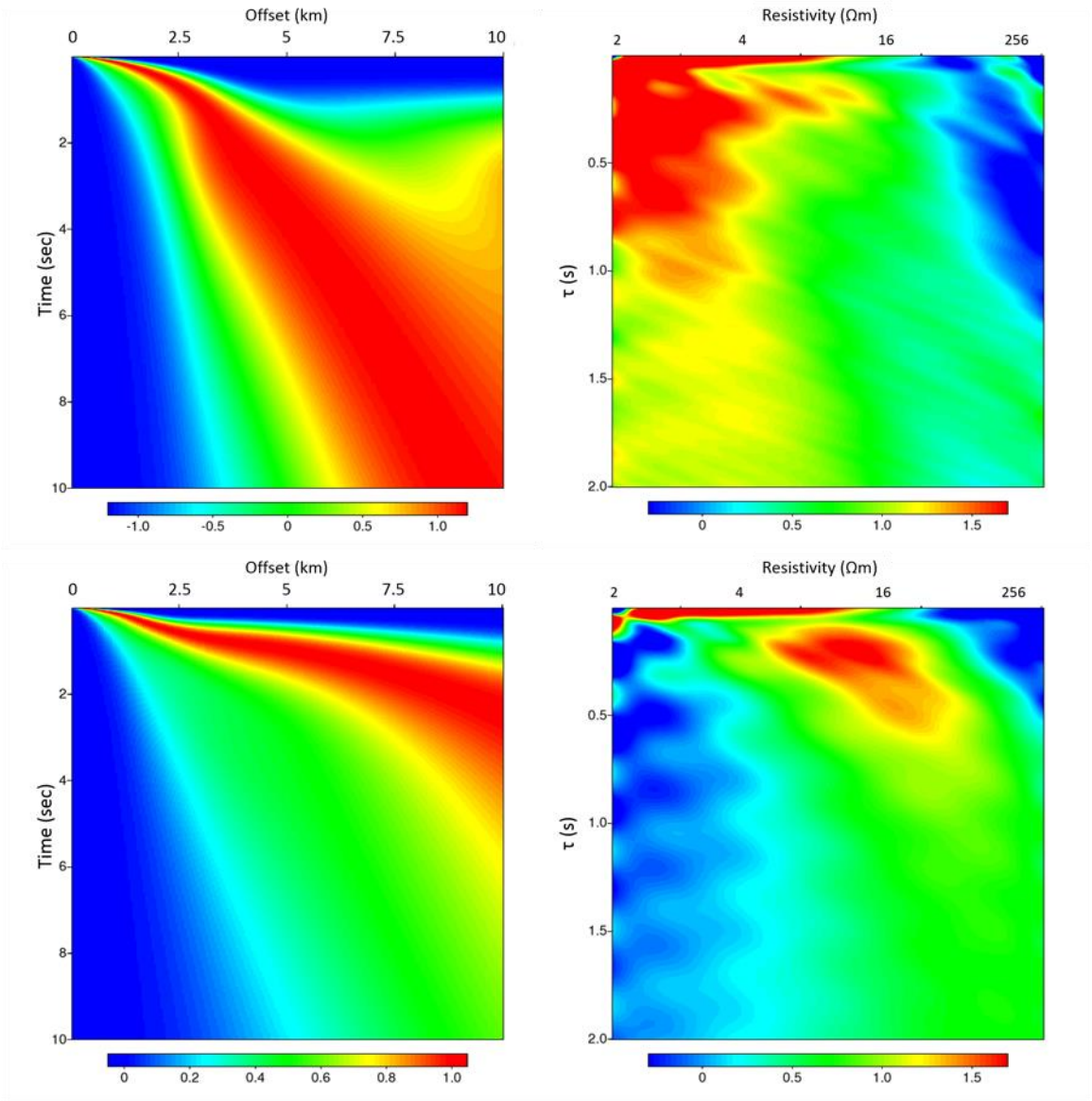

b) 75 Ωm reservoir

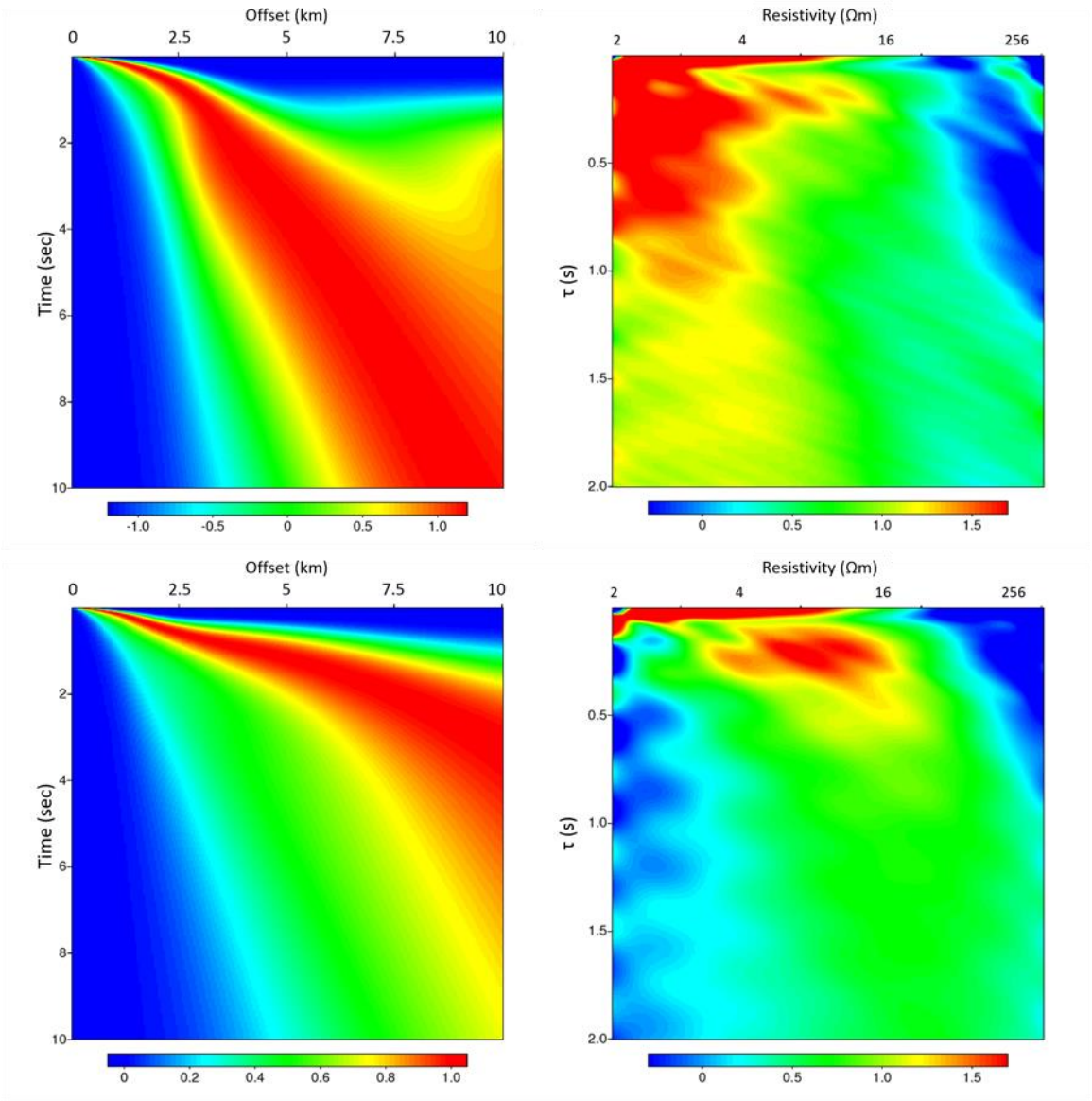

c) 50 Ωm reservoir

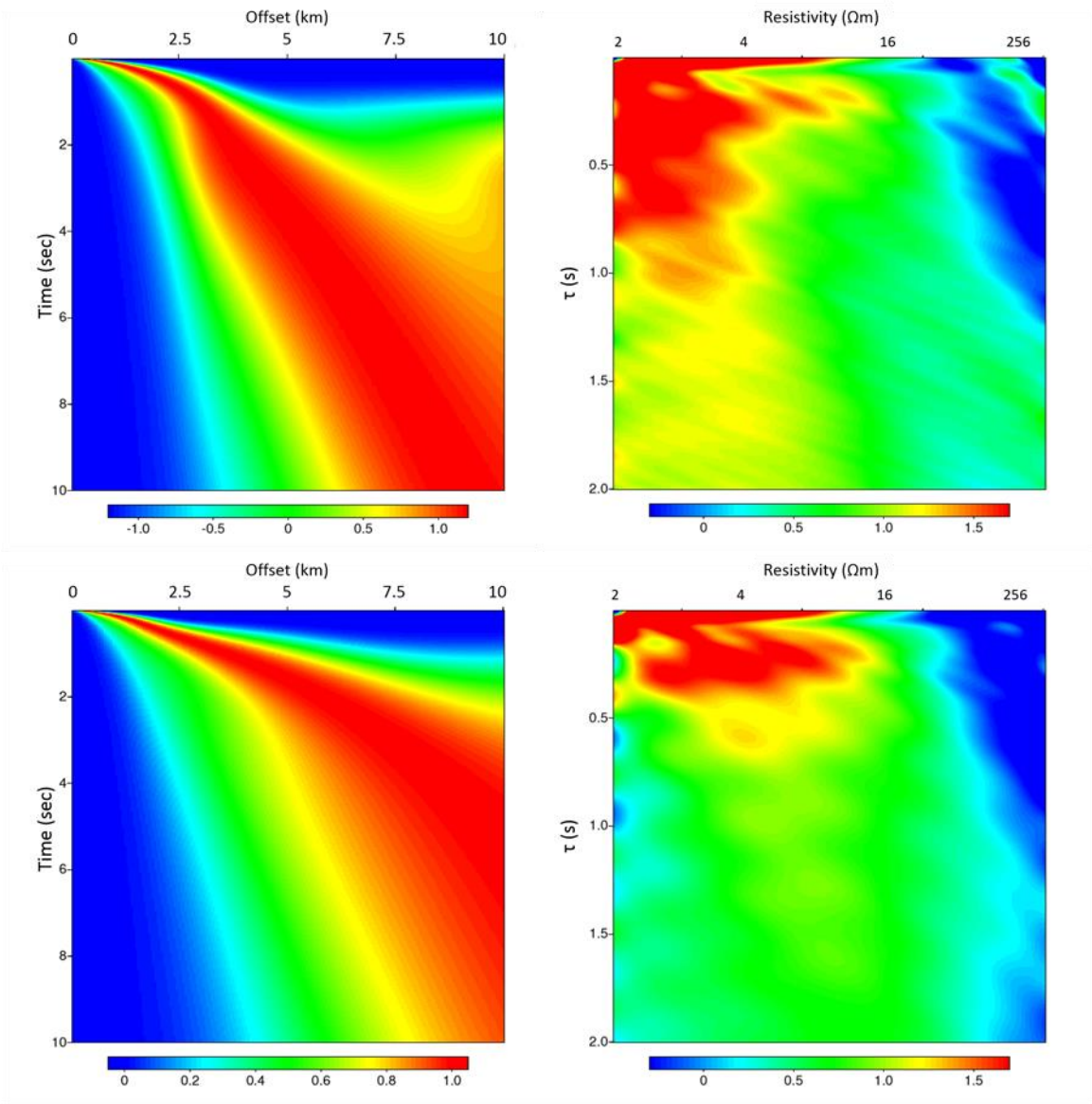

d) 25 Ωm reservoir

(For each image set: top left – normalized inline horizontal electric field amplitude for Canonical Model w/o reservoir, top right – EM-Radon for Canonical model w/o reservoir; bottom left – normalized inline horizontal electric field amplitude for Canonical Model, bottom right – EM-Radon for Canonical Model [normalized volts/meter for all images].)

Figure 7.3.1: EM-Radon plots for various reservoir resistivities

8 EM-Radon and T-equivalence

8.1 T-equivalence tests

It is well-known (*cf. e.g.*, Constable and Weiss, 2006) in the CSEM community that (for a resistive layer that is thin relative to its depth measured from the surface) DC resistivity sounding resolves only the resistivity-thickness *product.* This is commonly known as "T-equivalence", defined by $T = \rho \Delta d$, where Δd is the thickness of the resistive layer. Constable and Weiss (2006) show that, for the Canonical Model studied in this thesis, strict T-equivalence breaks down for frequencies above 0.1 Hz. For the impulse responses in this thesis, Figure (3.1.1) above shows that energy remains above 0.1 Hz at all offsets. Consequently, one might wonder whether the EM-Radon transform will exhibit true T-equivalence.

This section presents EM-Radon transforms for Canonical Model variations that preserve T-equivalence at T = $10^4\,\Omega m^2$. To facilitate comparison, in all three cases, the reservoir lies below a 1 km sediment overburden, rather than (for example) at the same average reservoir depth. Figure 8.1a shows transforms for the base Canonical Model where ρ is 100 Ωm, Δd is 100 m (T = $10^4\,\Omega m^2$), and the reservoir lies from 1 km to 1.1 km below the seabed. For Figure 8.1b ρ is 50 Ωm, Δd is 200 m (T = $10^4\,\Omega m^2$), and reservoir lies from 1 km to 1.2 km below the seabed. For Figure 8.1c ρ is 125 Ωm, Δd is 80 m (T = $10^4\,\Omega m^2$), and reservoir lies from 1 km to 1.08 km below the seabed. As suggested by Constable and Weiss (2006), the EM-Radon transform results are very similar in all three cases, so, near T-equivalence is observed.

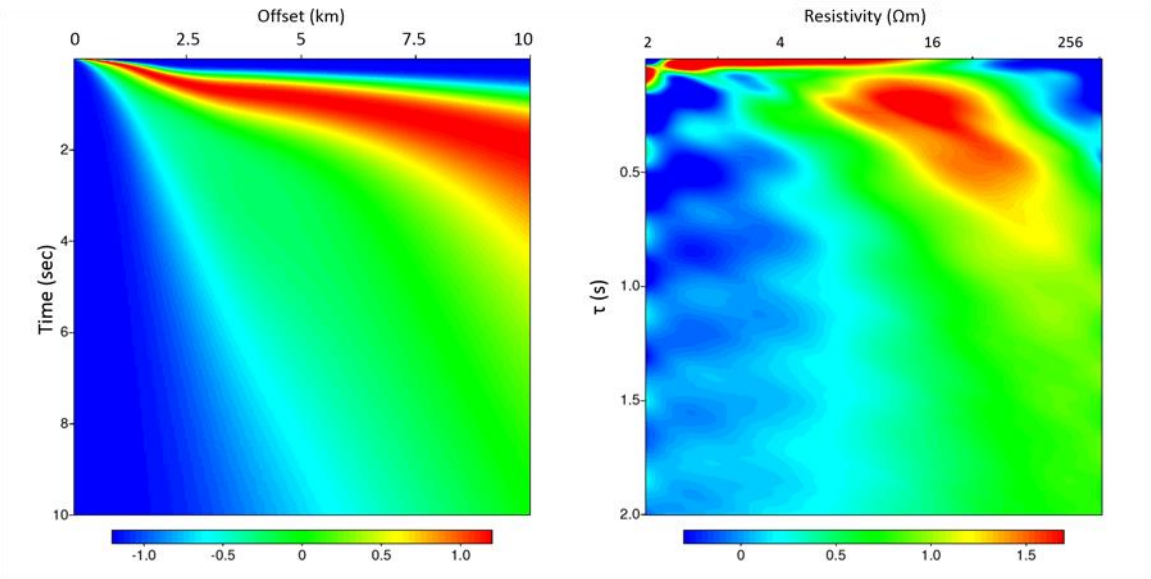

a) Base Model – 100 Ωm by 100 m thick reservoir lying 1 km to 1.1 km below the seabed

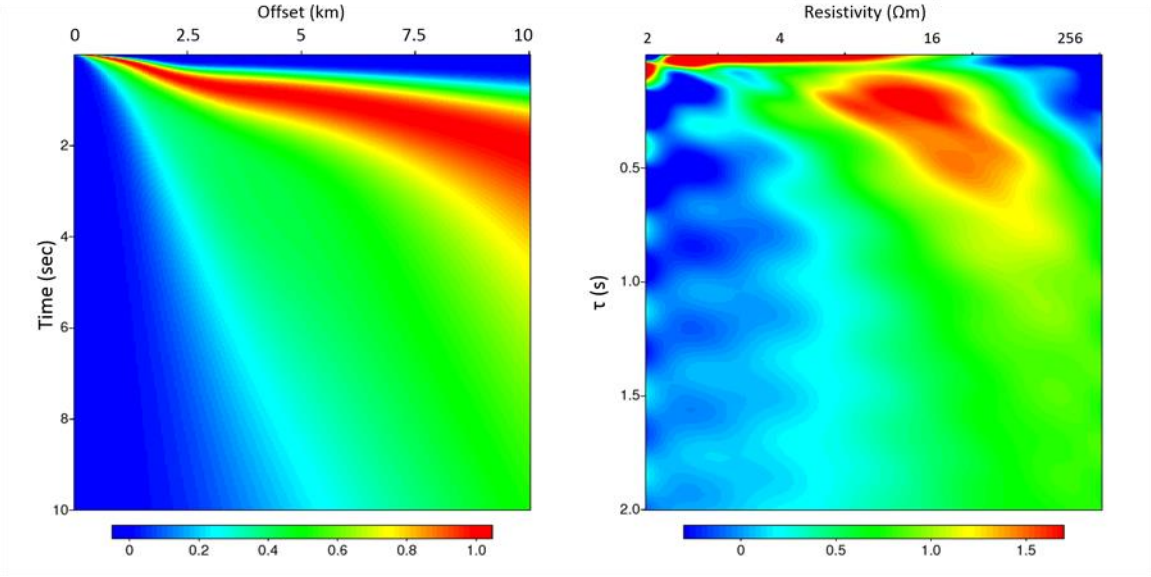

b) 50 Ωm by 200 m thick reservoir lying 1 km to 1.2 km below the seabed

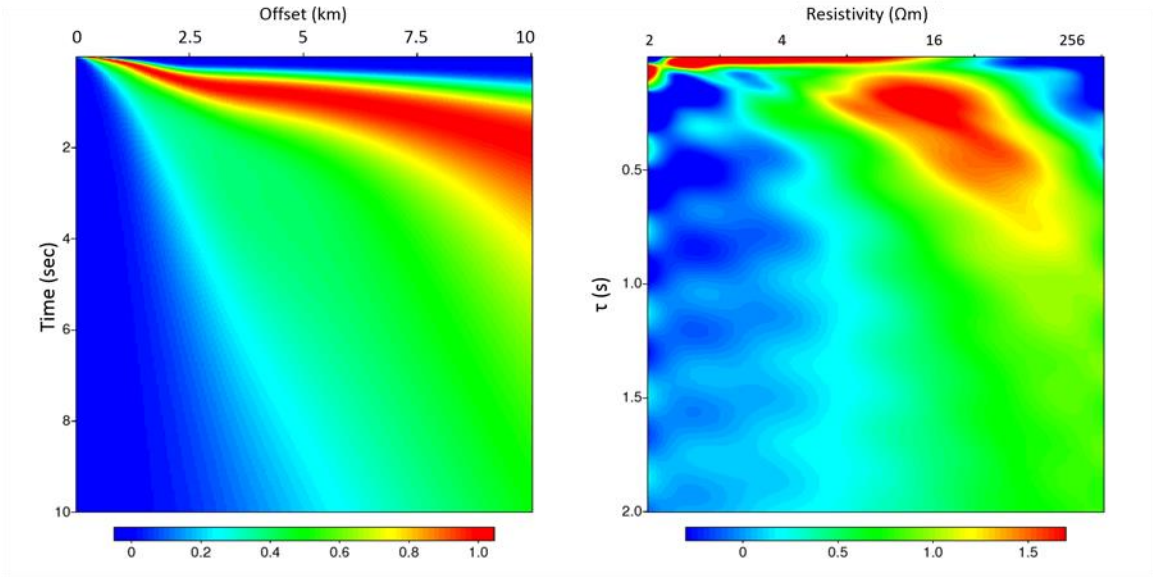

c) 125 Ωm by 80 m thick reservoir lying from 1 km to 1.08 km below the seabed

(For each image set: left – normalized inline horizontal electric field amplitude for Canonical Model, right – EM-Radon for Canonical Model [normalized volts/meter for all images].)

Figure 8.1.1: EM-Radon T-equivalence plots

Swidinsky and Edwards (2009) show that T-equivalence is a natural theoretical consequence of 2-D boundary conditions. In Appendix C.1, below, it is shown that their argument is consistent with the importance of lateral waves in CSEM.

On the other hand, T-equivalence requires that moveout of the reservoir lateral wave be a function of reservoir thickness as well as resistivity. This further stretches the concept of "lateral wave" in this thesis. In Appendix C.2, below, phase gradients nonetheless illustrate a high degree of moveout linearity in the Canonical Model.

It follows that all of the previous EM-Radon plots showing inferred "resistivity" should be understood more precisely as showing "T-equivalent resistivity", rather than actual, in-situ resistivity.

Furthermore, T-equivalence is seen to be an approximate extrinsic measure of hydrocarbon presence. Archie's equation (Archie, 1942) enables an estimate for a reservoir's Oil In Place (OIP) per acre:

$$\frac{OIP}{acre} = \left\{1 - \sqrt[n]{\frac{\phi^{-m}\rho_w}{\rho}}\right\}\phi\Delta d = \left\{1 - \sqrt[n]{\frac{\phi^{-m}\rho_w}{\rho}}\right\}\frac{\phi}{\rho}T \qquad (8.1.1)$$

where ϕ is porosity, ρ_w is brine resistivity, R is formation resistivity, m and n are empirical constants. All of Archie's parameters are intrinsic to the wellbore in which they are measured, and are routinely extrapolated over reservoir dimensions to estimate reservoir value. Because T-equivalence does not allow estimating these intrinsic parameters, it provides only an approximate indication of OIP.

9 Conclusion

9.1 Suggestions for future work

Most importantly: all work has been done on 1-D synthetic data for isotropic media. It would be useful to try these techniques on 2.5-D synthetic data that have been offered by Kerry Key from Scripps Institute. This would allow creating images that could be overlaid on seismic cross-sections. Subsequently, 3D models should be computed and tested, prior to any field work.

More study of the effects of aliasing in the (τ, p) domain would be useful to understand time and offset sampling requirements to achieve desired resistivity resolution with EM-Radon.

For this Canonical Model, EM-Radon appears to be responding to transverse resistance. Further study could determine how this comes about.

The simple normalization chosen has been effective in demonstrating that ISEM data is amenable to seismic-style processing. However, the data normalization has affected the results, by coloring offset-dependence. As regards the Fourier frequency transform of the original un-normalized data, the transform of the normalized data will be scaled by $s(x)$ according to the Addition theorem (Bracewell, 1978). As regards the Fourier wavenumber transform of the original data, the transform of the normalized data will be the convolution of $s(\omega)$ with the original data transform according to the Convolution theorem (Bracewell, 1978). It is possible that improvements could accrue from taking these effects into account.

It may be possible to define a "figure of merit" such as semblance (Neidell and Taner, 1971) to simplify choosing the best resistivity moveout correction.

It would be interesting to try combinations of Radon transform filtering for frequency-independent moveout (air wave, and environmental noise), with EM-Radon transform filtering for resistivity (reservoir, and sediment waves, etc.).

Spectral decomposition is one of the few seismic processing techniques designed to handle dispersion. Preliminary research into its use for this problem is the subject of current research with Professor Castagna and his associate Dr. Arnold Oyem.

The opportunity also exists to relax the isotropy assumption by generating 1-D simulations for VTI resistivity anisotropy using code made available by the SEG in connection with a recent Geophysics article by Hunziker *et al.* (2015).

Professor Jackson has suggested a processing technique that identifies wavenumbers present in (t, x) data. The generalized pencil of functions (Sarkar *et al.*, 1995) is used in electrical engineering for this purpose.

Closed-form solutions for homogeneous layered media derived via the spectral domain method Scott (1988) might yield insight when compared with those presented in Ward *et al.* (1987).

The ultimate test, of course, would be to create an image of real-world data.

9.2 Conclusion

This thesis has shown that synthetic 1-D EM data generated for a Canonical Model and using simulation software well-accepted by the geophysical EM community can be processed by seismic algorithms commonly used in the geophysical seismic community, yielding estimates of T-equivalent subsurface resistivity without formal mathematical inversion. Further, simple modification to some of these algorithms, to account for EM dispersion, appears to

enhance their effectiveness substantially. This validates an argument made over the years by Thomsen *et al.* (2007, 2009), Strack *et al.* (2008), and Thomsen (2014), and can hopefully serve as a bridge, and provide avenues for cross-fertilization, between these two branches of the geophysical community.

10 References

Aki, K., and P.G. Richards, 2009, Quantitative Seismology, second edition: University Science Books, www.uscibooks.com.

Anderson, J.E., 1993, Parabolic and linear 2-D τ-p transforms using the generalized radon transform: in May 11-14, 1993 Project Review, Consortium Project on Seismic Inverse Methods for Complex Structures, CWP-137, Center for Wave Phenomena internal report, 109-120.

Archie, G.E., 1942, The electrical resistivity log as an aid in determining some reservoir characteristics: **Transactions of the American Institute of Mineralogical Metallurgy, Petroleum Engineering**, **146**, 54-62.

Balanis, C.A., 1989, Advanced Engineering Electromagnetics: John Wiley & Sons, Inc., Hoboken, NJ.

Bracewell, R. N., 1978, The Fourier Transform and its Applications: McGraw-Hill, Inc., New York.

Connell, D., and K. Key, 2013, A numerical comparison of time and frequency-domain marine electromagnetic methods for hydrocarbon exploration in shallow water: **Geophysical Prospecting, 61**, 187-199.

Constable, S., and C.J. Weiss, 2006, Mapping thin resistors and hydrocarbons with marine EM methods: Insights from 1D modeling: **Geophysics**, **71**, no. 2, G43-G51.

Forel, D., T. Benz, and W.D. Pennington, 2005, Seismic Data Processing with Seismic Un*x, a 2D Seismic Data Processing Primer: Course Notes Series No. 12, L.M. Gochioco, Editor, Society of Exploration Geophysicists.

Foster, D.J., and C.C. Mosher, 1992, Suppression of multiple reflections using the Radon transform: **Geophysics, 57**, no. 3, 386-395.

Futterman, W.I., 1962, Dispersive Body Waves: **Journal of Geophysical Research, 67,** No. 13, 5279-5291.

Harrington, R.F., 2001, Time-Harmonic Electromagnetic Fields: IEEE Press reprint, originally John Wiley & Sons, Inc., New York.

Houck, R.T., A. Ciucivara, and S. Hornbostel, 2013, Probabilistic Interpretation of CSEM Resistivity: **Society of Exploration Geophysicists Annual Meeting Expanded Abstracts**, **83.**

Hunziker, J., J. Thorbecke, and E. Slob, 2015, The electromagnetic response in a layered vertical transverse isotropic medium: A new look at an old problem: **Geophysics, 80**, no. 1, F1-F18.

Jackson, J.D., 1999, Classical Electrodynamics – Third edition: John Wiley & Sons, Inc., Hoboken, NJ.

Keller, G.V., 1987, Rock and Mineral Properties, *in* Electromagnetic Methods in Applied Geophysics: Society of Exploration Geophysicists, 52-129.

Key, K., 2009, 1D inversion of multicomponent, multifrequency marine CSEM data: Methodology and synthetic studies for resolving thin resistive layers: **Geophysics, 74,** no. 2, F9-F20.

Key, K., 2012, Is the fast Hankel transform faster than quadrature?: **Geophysics, 77,** no. 3, F21-F30. [Software available at http://software.seg.org/2012/0003]

Liu, H.-P., D.L. Anderson, and H. Kanamori, 1976, Velocity dispersion due to anelasticity; implications for seismology and mantle composition: **Geophysical Journal of the Royal Astronomical Society**, **47**, 41-58.

Mavko, G., T. Mukerji, and J. Dvorkin, 2011, The rock physics handbook: tools for seismic analysis of porous media – Second edition: Cambridge University Press, New York.

Mittet, R., and J.P. Morten, 2012, Detection and imaging sensitivity of the marine CSEM method: **Geophysics, 77**, no. 6, E411-E425.

Morozov, I.B., 2011, Anelastic acoustic impedance and the correspondence principle: **Geophysical Prospecting**, **59**, 24–34.

Neese, J.W., and L.A. Thomsen, 2014a, System and Method for Processing Electromagnetic Survey Data, U.S. Provisional Patent Application No. 62066126 by the University of Houston.

Neese, J.W., and L.A. Thomsen, 2014b, Seismic processing of numerical EM data: SEG Technical Program Expanded Abstracts 2014: pp. 870-874. [http://dx.doi.org/10.1190/segam2014-1238.1]

Neese, J.W., and L.A. Thomsen, 2015, Robustness of the EM-Radon transform, abstract submitted to Madrid 2015: 77th EAGE Conference & Exhibition.

Neidell, N.S., and M.T. Taner, 1971, Semblance and other coherency measures for multichannel data: **Geophysics, 36,** no. 3, 482-497.

Palacky, G.J., 1987, Resistivity Characteristics of Geologic Targets, *in* Electromagnetic Methods in Applied Geophysics: Society of Exploration Geophysicists, 52-129.

Pawar, S.D., P. Murugavel, D. M. Lal (2009), Effect of relative humidity and sea level pressure on electrical conductivity of air over Indian Ocean: **Journal of Geophysical Research**, **114**: D02205.

Sarkar, T.K., and O. Pereira, Using the Matrix Pencil Method to Estimate the Parameters of a Sum of Complex Exponentials: **IEEE Antennas and Propagation Magazine**, Vol. 37, No. 1, 48-55.

Scott, C., 1989, The Spectral Domain Method in Electromagnetics: Artech House, Norwood, MA.

Stockwell, J.W., and J.K. Cohen, 2008, The *New* SU User's Manual Version 4.0: Center for Wave Phenomena, Colorado School of Mines. [Software and Manual available at http://www.cwp.mines.edu/cwpcodes/]

Strack, Kurt M.; Thomsen, Leon A.; Reuter, H., Method for acquiring transient electro-magnetic survey data, filed 2005, issued April 10, 2007, U.S. Patent 7203599.

Strack, K., N. Allegar, and S. Ellingsrud, 2008, Marine time domain CSEM: an emerging technology: **Society of Exploration Geophysicists Annual Meeting Expanded Abstracts**, **78,** 653-656.

Swidinsky, A., and R.N. Edwards, 2009, The transient electromagnetic response of a resistive sheet: straightforward but not trivial: **Geophysical Journal International**, **179**, 1488–1498.

Thomsen, L., D. Meaux, S. Li, C. Wesiss, A. Sharma, N. Allegar, and K. Strack, 2007, Novel marine electromagnetics: From deep into shallow water: Recent Advances and the Road Ahead: **Society of Exploration Geophysicists Annual Meeting Expanded Abstracts**, **77.**

Thomsen, L.A., N.C. Allegar, J.A. Dellinger, P. Jilek, D.T. Johnson, G. Xia, 2009: System and Method for using Time-Distance Characteristics in Acquisition, Processing, and Imaging of t-CSEM Data, U.S. Patent 7,502,690, 7941273.

Thomsen, L.A., 2014, Electromagnetics and Seismics: the Deep Connections: **Society of Exploration Geophysicists Annual Meeting Expanded Abstracts, 84.**

Turner, G., 1990, Aliasing in the *tau-p* transform and the removal of spatially aliased coherent noise: **Geophysics, 55**, no.11, 1496-1503.

Ward, S.H., and G.W. Hohmann, 1987, Electromagnetic theory for geophysical applications, *in* Electromagnetic Methods in Applied Geophysics: Society of Exploration Geophysicists, 131-312.

Yilmaz, O., 2001, Seismic data analysis: processing, inversion, and interpretation of seismic data: M.R. Cooper, editor, IG Series No.10, Society of Exploration Geophysicists, Tulsa.

11 Appendix A

A.1 EM and anelastic seismic in mathematical terms

The primary connection between EM and anelastic seismology is that the dissipative wave equation describes both of these two physically unrelated phenomena. As a result, the two solutions share the same form for Fourier basis terms. Methods and measures used to describe and interpret the wave equations and Fourier basis terms apply equally to both phenomena. These include wavenumber, phase velocity, quality parameter, wavelength, skin depth, index of refraction, reflection coefficients, critical angles, and so on. This mathematical commonality provides a way to understand and quantify differences and similarities. The differences are important, but the similarities are striking.

In broad 1-D overview, both EM and anelastic seismic wave equations are expressed as variations on the canonical form of Maxwell's equations:

$$\frac{\partial^2 \vec{w}}{\partial x^2} - A\frac{\partial \vec{w}}{\partial t} - B\frac{\partial^2 \vec{w}}{\partial t^2} = 0 \qquad \text{(A.1.1)}$$

In EM, $\vec{w}$ is the intensity of the electric field $\vec{E}$ or of the magnetic field $\vec{H}$, both of which are polarized transverse to x. In anelastic seismology, $\vec{w}$ is the longitudinal "P-wave" displacement (within the wave), with polarization oriented parallel to x, or the transverse "S-wave" displacement, with polarization oriented in the plane normal to x.

Geophysicists have chosen different ways to incorporate attenuation and dispersion into EM and anelastic wave equations, *e.g.*, Keller (1988) and Aki and Richards (2009). As mentioned above, A and B can, in principle, be real- or complex-valued.

For EM, real A and complex B are chosen:

$$A = \mu\sigma$$
$$B = \mu\varepsilon \tag{A.1.2}$$

where the medium permeability μ (Henry/meter), and medium conductivity σ (Siemens/meter) are real, and the medium permittivity ε (Farad/meter) is complex.

$A\frac{\partial \vec{E}}{\partial t} = \mu\sigma\frac{\partial \vec{E}}{\partial t}$ is called the "conduction" term, and $B\frac{\partial^2 \vec{E}}{\partial t^2} = \mu\varepsilon\frac{\partial^2 \vec{E}}{\partial t^2}$ is called the "polarization" or "displacement" term. For surface-based experiments designed to probe deeply into the sedimentary crust, the frequency band is from about .01 Hz to about 10 Hz, due to severe attenuation in most earth media and relatively deep targets. As mentioned above, for most earth media excepting air, and other gasses, the displacement term can be ignored (see Equation (A.3.1), below), leaving only the conduction term. Thus, Equation (A.1.1) degenerates into the diffusion equation:

$$\frac{\partial^2 \vec{E}}{\partial x^2} - \mu\sigma\frac{\partial \vec{E}}{\partial t} = 0 \tag{A.1.3}$$

For anelastic seismology, A is set to zero, and B is the complex-valued "modulus" term:

$$A = 0$$
$$B = \frac{M_c}{\tilde{m}} \tag{A.1.4}$$

where M_c is complex medium modulus (Pascal, or kg/(ms^2)), and $\tilde{m}$ is medium density (kg/m^3) (note that $\rho = 1/\sigma$ is reserved for resistivity in the EM problem). P-wave modulus differs from S-wave modulus. Thus, Equation (A.1.1) can be expressed:

$$\frac{\partial^2 \vec{u}}{\partial x^2} - \frac{M_c}{\tilde{m}}\frac{\partial^2 \vec{u}}{\partial t^2} = 0 \tag{A.1.5}$$

Both Equations (A.1.3) and (A.1.5) admit plane-wave solutions expressed as sums of Fourier basis terms:

$$\vec{w}(x,\omega) = \vec{w}_0(\omega) e^{i(\omega t - k(\omega)x)} \tag{A.1.6}$$

where $\vec{w}_0$ is a complex amplitude defined at a time and space origin, and k is a complex-valued wavenumber . It is convenient to name the real and imaginary parts of k :

$$k(\omega) = \beta(\omega) - i\alpha(\omega) \tag{A.1.7}$$

The explicit minus sign in Equation (A.1.7) ensures that the material parameter α is positive, as required by the 2nd Law of Thermodynamics.

For EM diffusion, we can verify by direct substitution that β^{EM} is equal to α^{EM} :

$$\begin{aligned} \beta^{EM}(\omega) &= \sqrt{\frac{\omega\mu\sigma}{2}} \\ \alpha^{EM}(\omega) &= \sqrt{\frac{\omega\mu\sigma}{2}} \end{aligned} \tag{A.1.8}$$

In the anelastic seismic case, defining:

$$M_c(\omega) = M_{\mathrm{Re}}(\omega) + iM_{\mathrm{Im}}(\omega) \tag{A.1.9}$$

we find that:

$$\beta^{seis}(\omega) = \omega\sqrt{\frac{M_{\mathrm{Re}}(\omega)}{2\tilde{m}}}\left[\sqrt{1+\left(\frac{M_{\mathrm{Im}(\omega)}}{M_{\mathrm{Re}(\omega)}}\right)^2}+1\right]^{\frac{1}{2}}$$
$$\alpha^{seis}(\omega) = \omega\sqrt{\frac{M_{\mathrm{Re}}(\omega)}{2\tilde{m}}}\left[\sqrt{1+\left(\frac{M_{\mathrm{Im}(\omega)}}{M_{\mathrm{Re}(\omega)}}\right)^2}-1\right]^{\frac{1}{2}} \qquad \text{(A.1.10)}$$

As a sanity check, in the perfectly elastic case, M_{Im} is zero so that

$$k^{seis}_{elastic}(\omega) \equiv \beta^{seis}(\omega) = \omega\sqrt{\frac{M_{\mathrm{Re}}(\omega)}{\tilde{m}}} = \omega\sqrt{\frac{M}{\tilde{m}}} \qquad \text{(A.1.11)}$$

is real.

Now we note various measures in common between the two cases:

$$Q(\omega) \equiv \frac{\beta(\omega)}{2\alpha(\omega)} \Rightarrow k(\omega) = \beta(\omega)\left(1-\frac{i}{2Q(\omega)}\right)$$
$$\delta(\omega) = \frac{1}{\alpha(\omega)}$$
$$\lambda(\omega) = \frac{2\pi}{\beta(\omega)} \qquad \text{(A.1.12)}$$
$$v_{phs}(\omega) = \frac{\omega}{\beta(\omega)}$$
$$n(\omega) = \frac{c\beta(\omega)}{\omega}$$

Here, Q is dimensionless quality parameter, δ is skin depth (at which amplitude drops by the fraction e^{-1} to about 37% of its original value), λ is wavelength, v_{phs} is (real) phase velocity, and n is index of refraction.

A.2 Motivation for complex seismic modulus

In elastic seismology, the medium itself is characterized by its frequency-independent phase velocity, and infinite Q_{seis}, as can be seen from Equation (A.1.12):

$$v_{phs}^{seis} = \sqrt{\frac{M}{\tilde{m}}} \tag{A.2.1}$$

The elastic moduli are derived using a linearly elastic form of Hooke's law, which in a homogeneous and isotropic medium can be expressed:

$$\tau = M\xi \tag{A.2.2}$$

where τ is stress (force per unit area), and ξ is strain (deformation due to stress), (Note: the symbol ε (sometimes used to denote elastic strain) is reserved for electrical permittivity, above).

Thomsen (2014) motivates Equation (A.1.5) by allowing v, and therefore M, to be complex, noting that the physical mechanisms behind complex M are poorly understood. As a result, Q_{seis} is normally estimated from the data itself. Equation (A.1.6) can be expressed:

$$\vec{u}\left(x,\omega\right) = \vec{u}_0\left(\omega\right) e^{i\omega\left(t - \frac{x}{v_{phs}(\omega)}\right)} e^{-\omega\left(\frac{x}{2v_{phs}(\omega)Q_{seis}(\omega)}\right)} \tag{A.2.3}$$

A possible physical mechanism for complex-valued M_c is put forth in Liu *et al.* (1976) where Equation (A.2.2) is replaced by a standard linear solid model, in which:

$$\tau + t_F \frac{d\tau}{dt} = M_R\left(\xi + t_D \frac{d\xi}{dt}\right) \tag{A.2.4}$$

where t_F is the stress relaxation time under constant strain, and t_D is the strain relaxation time under constant stress, and M_R is the fully-relaxed modulus. The complex modulus M_c is defined by:

$$M_c(\omega) = \frac{M_R}{a(\omega) - ib(\omega)} \tag{A.2.5}$$

where a and b are functions of t_F and t_D. It is noted by Liu *et al.* (1976) that:

$$Q_{seis}(\omega) = \frac{a(\omega)}{b(\omega)} \tag{A.2.6}$$

M_c is postulated to vary across frequency ranges that correspond to different relaxation mechanism regimes. Liu *et al.* (1976) present Figure A.2.1, where the observed relative constancy of Q_{seis} is reproduced for a solid with twelve relaxation mechanisms.

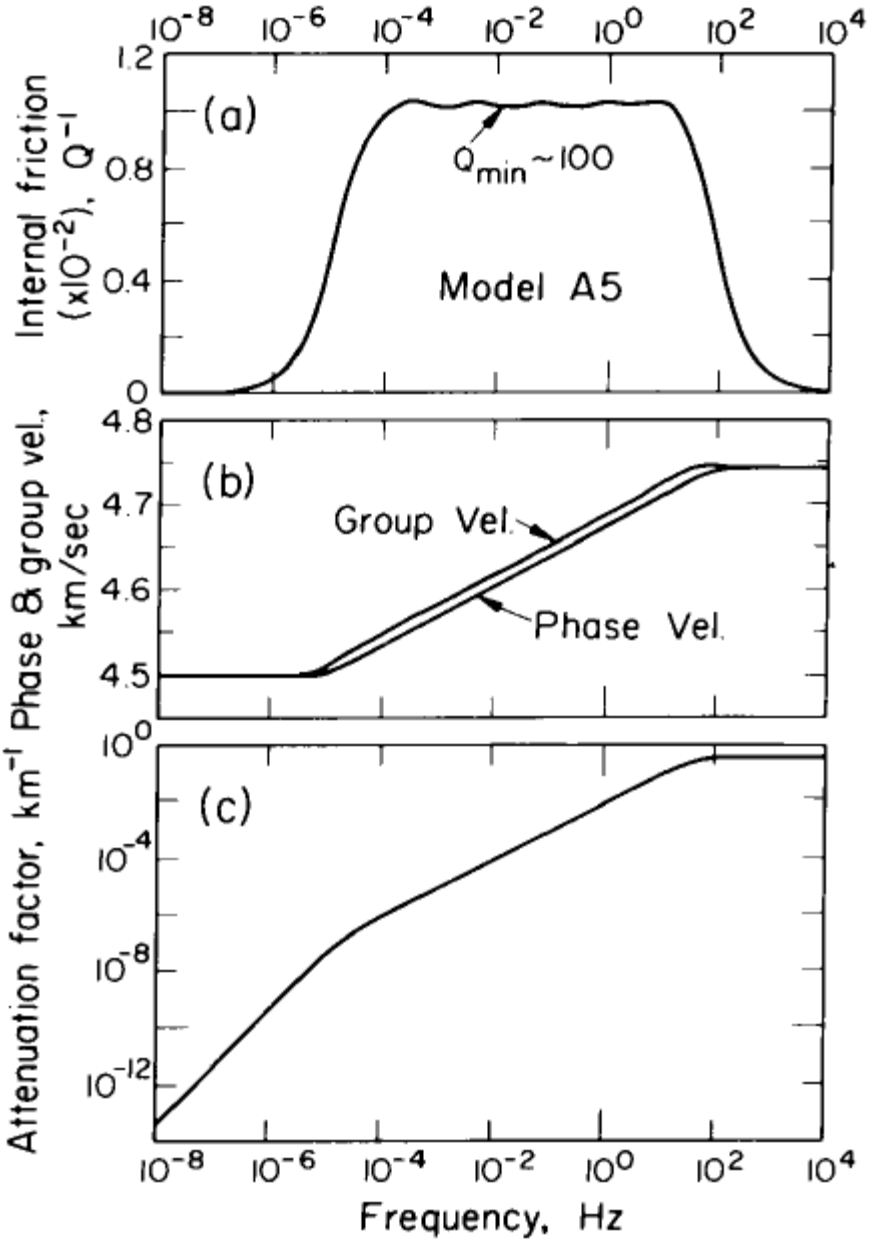

Figure A.1.1: (a) Internal friction coefficient, (b) phase and group velocity dispersion, (c) attenuation factor as a function of frequency, for a solid with twelve relaxation mechanisms, from Liu et al. (1976), Figure 3.

This relatively high value for Q_{seis} over a typical range for seismic frequencies is why, as Thomsen (2014) notes, in exploration geophysics the approximation is commonly made that $Q_{seis} \approx \infty$, and Equation (A.1.5) reduces to:

$$\frac{\partial^2 \vec{u}}{\partial x^2} - \frac{M}{\tilde{m}} \frac{\partial^2 \vec{u}}{\partial t^2} = 0 \tag{A.2.7}$$

A.3 Motivation for ignoring EM displacement current

Thomsen (2014) develops the 1-D EM diffusion equation as a specialization to earth media of Maxwell's wave equation. He writes the 1-D wave equation for the electric field (within a non-magnetic material), retaining the inertial term, as:

$$\frac{\partial^2 \vec{E}}{\partial x^2} - \frac{\mu_0}{\rho} \frac{\partial \vec{E}}{\partial t} - \frac{n^2}{c^2} \frac{\partial^2 \vec{E}}{\partial t^2} = 0 \tag{A.3.1}$$

where c is the speed of light in free space, n is the index of refraction (>1) of the medium, μ_0 is the magnetic permeability of free space (4π x 10^{-7} N/A^2), and ρ is the electrical resistivity of the medium. Note that the inertial term is complex-valued since:

$$\frac{n^2}{c^2} = \varepsilon\mu \cong \varepsilon\mu_0 \tag{A.3.2}$$

and ε is the complex-valued electric permittivity of the medium. Postulated physical mechanisms behind permittivity yield qualitatively satisfactory results, but in the end, as in the seismic case, the complex inertial parameter is measured from the data.

Just as in the seismic case, all solutions to Equation (A.3.1) can be represented as a sum of Fourier basis terms:

$$\begin{aligned} \vec{E}(x,\omega) &= \vec{E}_0(\omega) e^{i\left(\omega t - k^{EM} x\right)} = \vec{E}_0(\omega) e^{i\omega\left(t - \frac{x}{v^{EM}}\right)} \\ &= \vec{E}_0(\omega) e^{i\omega\left(t - \frac{x}{v_{phs}^{EM}}\right)} e^{-\omega\left(\frac{x}{2v_{phs}^{EM} Q_{EM}}\right)} \end{aligned} \tag{A.3.3}$$

This expression solves Equation (A.3.1) if and only if wavenumber k^{EM} satisfies:

$$k^{EM}(\omega) = \omega \frac{n}{c}\left(1 + i\frac{\mu_0}{\omega\rho}\left(\frac{c}{n}\right)^2\right)^{\frac{1}{2}} \tag{A.3.4}$$

Thus, complex phase velocity v^{EM} can be expressed:

$$v^{EM} = \frac{\omega}{k^{EM}} = \frac{c}{n}\left(1 + i\frac{\mu_0}{\omega\rho}\left(\frac{c}{n}\right)^2\right)^{-\frac{1}{2}} \tag{A.3.5}$$

Thomsen (2014) notes that the imaginary term in Equation (A.3.5) dominates the real term at low frequencies (the conduction regime), while the real term dominates at high frequencies (the displacement regime). This is illustrated in Figure A.3.1, for parameters n and ρ suitable for sediments:

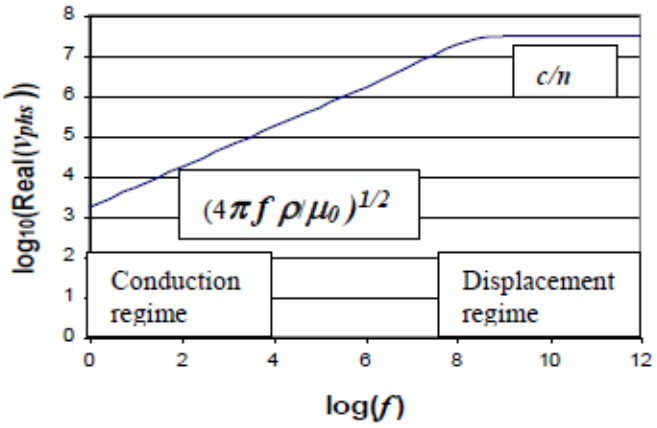

Figure A.3.1: v^{EM}_{phs} conduction and displacement regimes, with n =10 and ρ =1 Ωm, Thomsen (2014) Figure 1.

Finally, Thomsen (2014) notes that no matter what frequencies are created by the source, only the low frequencies penetrate deeply into the subsurface**.** Therefore, the conduction regime applies:

$$v_{phs}^{EM}(\omega) \cong \sqrt{\frac{2\rho\omega}{\mu_0}} \tag{A.3.6}$$

thus justifying Equation (A.1.3).

In the modeling described above, we apply this equation in the air, as well as in the sediments. It is easy to show that, for air, the "knee" in the graph above occurs at very low frequencies, well below the frequencies required for deep penetration. Consequently, *in spite* of the high resistivity (10^{12} Ωm) ascribed to it, for air the displacement regime applies. The modeling, therefore, is not strictly proper for air, but the inaccuracy is minor *due to* its high resistivity.

The value of CSEM data for hydrocarbon exploration stems from the fact that v_{phs}^{EM} depends on the resistivity ρ, which is anomalously high for hydrocarbon-rich rocks (this is the basis for the utility of resistivity logging). Hence, CSEM has the potential to be a "direct detector" of hydrocarbons.

12 Appendix B

B.1 Quality factors

An overriding theme is that seismic wavenumbers lie close to the real axis in the complex wavenumber plane, while EM wavenumbers lie along the 45° line in that plane (Figure B.1.1). This is reflected in Q values. For Earth media Q_{seis}^{P} and Q_{seis}^{S} are material parameters which generally exceed 30 (Futterman, 1962) and are relatively frequency-independent over the seismic frequency band. As shown above, Q_{EM} is *always* ½; it is a property of the diffusion equation, not the material.

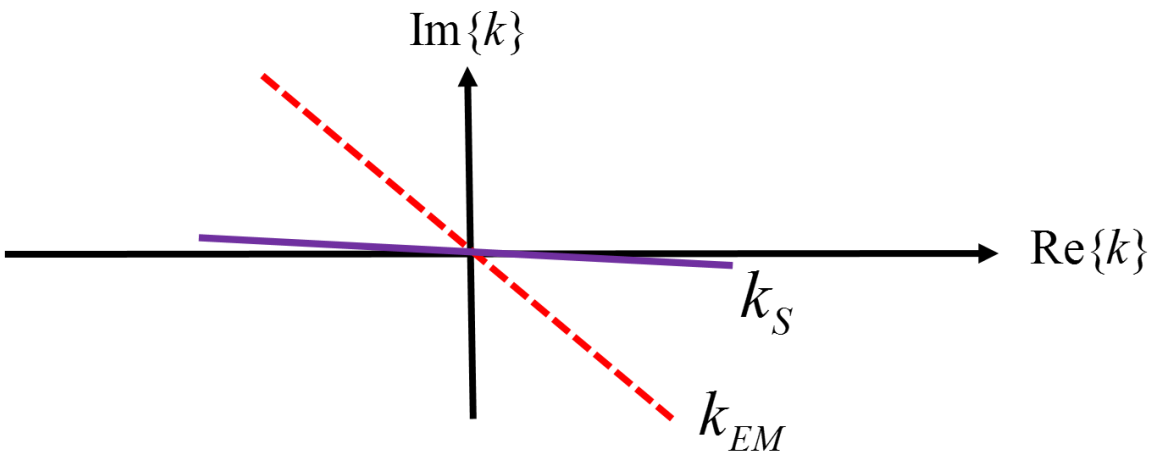

Figure B.1.1: A comparison of anelastic seismic and EM wavenumbers

B.2 Phase velocities

Low-frequency EM and seismic phase velocities are comparable in magnitude but possess very different degrees of dispersion, so much so that dispersion is normally ignored in standard seismic processing. In both cases, phase velocity v_{phs} is:

$$v_{phs}(\omega) = \frac{\omega}{\mathrm{Re}\{k(\omega)\}} \tag{B.2.1}$$

For the EM case, phase velocity is highly dispersive and depends on the square root of frequency:

$$v_{phs}^{EM}(\omega) \cong \sqrt{\frac{2\rho\omega}{\mu_0}} \tag{B.2.2}$$

For the seismic case, phase velocities vary only mildly with frequency, *e.g.*, less than a 2% increase with a 100-fold increase in frequency (Aki and Richards, 2009):

$$v_{phs}^{P}(\omega) \cong \sqrt{\frac{M^P}{\tilde{m}}}\left(1+\frac{1}{\pi Q^P}\log\left(\frac{\omega}{\omega_0}\right)\right) \tag{B.2.3}$$

$$v_{phs}^{S}(\omega) \cong \sqrt{\frac{M^S}{\tilde{m}}}\left(1+\frac{1}{\pi Q^S}\log\left(\frac{\omega}{\omega_0}\right)\right) \tag{B.2.4}$$

where ω_0 is a reference frequency, M^P is P-wave modulus, M^S is S-wave modulus, and $\tilde{m}$ is mass density. This mild velocity dispersion is generally ignored, yielding:

$$v_{phs}^{P} \cong \sqrt{\frac{M^P}{\tilde{m}}} \tag{B.2.5}$$

$$v_{phs}^{S} \cong \sqrt{\frac{M^S}{\tilde{m}}} \tag{B.2.6}$$

Seismic phase velocities typical to sedimentary basins from Mavko *et al.* (2011) are presented in Table B.2.1.

(Velocities in km/s)	v_{phs}^{P}			v_{phs}^{S}		
Chalk	1.53	to	4.30	1.59	to	2.51
Dolomite	3.41	to	7.02	2.01	to	3.64
Sandstones	3.13	to	5.52	1.73	to	3.60
Tight-gas sandstones	3.81	to	5.57	2.59	to	3.50
Limestone	3.39	to	5.79	1.67	to	3.04
High-porosity sandstones	3.46	to	4.79	1.95	to	2.66
Poorly consolidated sandstones	2.43	to	3.14	1.21	to	1.66

Table B.2.1: Examples of typical seismic phase velocities (from Table A.1, Mavko et al. (2011))

EM phase velocities, computed for a range of resistivities and frequencies are presented in Table B.2.2.

	$v_{phs}^{EM}(\omega)$ in km/sec			
Resistivity (Ωm)	@0.01 Hz	@ 0.1 Hz	@ 1.0 Hz	@10.0 Hz
1	0.2	0.7	2.2	7.1
10	0.7	2.2	7.1	22.4
100	2.2	7.1	22.4	70.7
1000	7.1	22.4	70.7	223.6

Table B.2.2: Examples of EM phase velocities at various frequencies and resistivities

These velocities must be put into the context of the resistivity ranges of various earth materials, as presented in Palacky (1987) and reproduced in Table B.2.3. As noted by Palacky (1987), for sedimentary rocks the range of resistivities is very broad and is often highly dependent on the volume and arrangement of porosity and on the salinity of brine contained therein (see Archie, 1942).

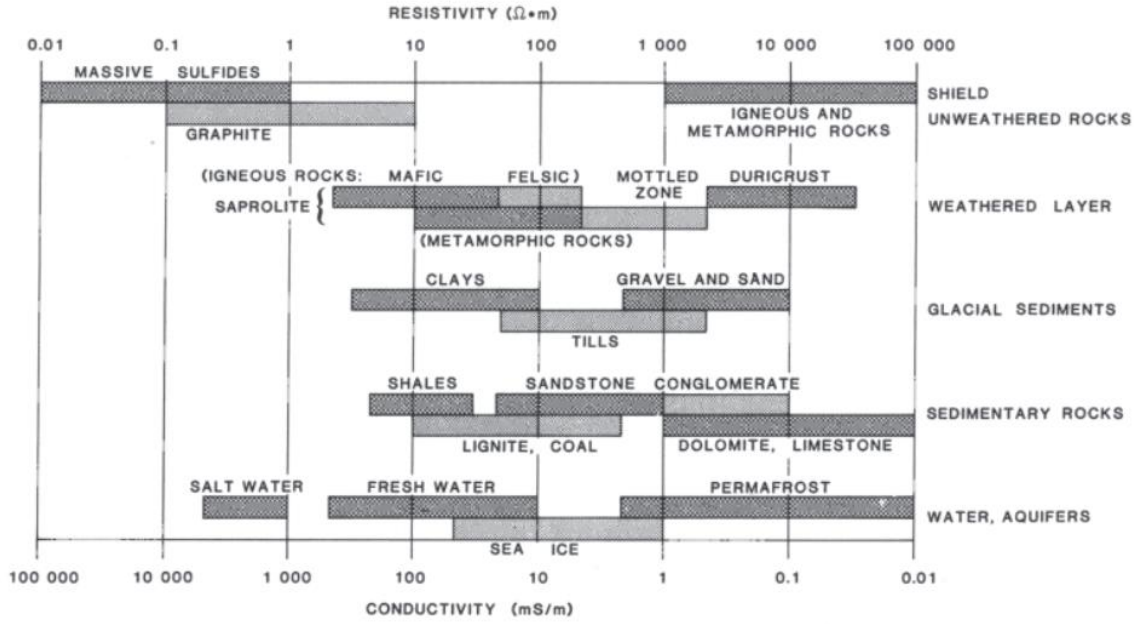

Table B.2.3: Typical ranges of resistivities of earth materials (Fig. 2: Palacky, 1987)

It is worth noting, here, that phase velocities in EM can be more than an order of magnitude greater than those typical in seismology.

B.3 Skin depths

The difference in seismic and EM phase velocities results in much smaller EM skin depths. For both cases, skin depth δ is:

$$\delta(\omega) = \frac{-1}{\mathrm{Im}\{k(\omega)\}} = \frac{2v_{phs}(\omega)Q}{\omega} \tag{B.3.1}$$

In the seismic case, with Q_{seis} virtually constant over seismic frequencies, and seismic v_{phs} only mildly dispersive, we can write:

$$\delta^P_{seis}(\omega) \cong 2\sqrt{\frac{M^P}{\tilde{m}}}\left(\frac{Q^P_{seis}}{\omega} + \frac{1}{\pi\omega}\log\left(\frac{\omega}{\omega_0}\right)\right) \cong \frac{2Q^P_{seis}}{\omega}v^P_{phs} \tag{B.3.2}$$

$$\delta_{seis}^{S}(\omega) \cong 2\sqrt{\frac{M^{S}}{\tilde{m}}}\left(\frac{Q_{seis}^{S}}{\omega}+\frac{1}{\pi\omega}\log\left(\frac{\omega}{\omega_0}\right)\right) \cong \frac{2Q_{seis}^{S}}{\omega}v_{phs}^{S} \tag{B.3.3}$$

For example, if we use $Q_{seis}=200$ and 30 Hz, skin depth ranges from 3 km to 11 km for P-waves, and from 2.5 km to 7 km for S-waves:

$$\delta_{seis}^{P} \cong 2v_{phs}^{P} \tag{B.3.4}$$

$$\delta_{seis}^{S} \cong 2v_{phs}^{S} \tag{B.3.5}$$

In the EM case:

$$\delta_{EM}(\omega)=\frac{v_{phs}^{EM}}{\omega}=\sqrt{\frac{2\rho}{\mu_0\omega}} \tag{B.3.6}$$

At 1 Hz the skin depth ranges from 350 m at 1 Ωm to 10 km at 1000 Ωm.

B.4 Reflection and transmission coefficients

For incident plane waves impinging normally on a planar interface separating two half-spaces, in both cases the reflection coefficient $R(\omega)$ and the transmission coefficient $T(\omega)$ are functions of the impedances above and below the interface:

$$R(\omega)=\frac{Z_2(\omega)-Z_1(\omega)}{Z_2(\omega)+Z_1(\omega)} \tag{B.4.1}$$

$$T(\omega)=\frac{2Z_2(\omega)}{Z_2(\omega)+Z_1(\omega)}=1+R(\omega) \tag{B.4.2}$$

In the seismic case (Morozov, 2011):

$$Z_{seis}^{P}(\omega) = -iM^{P}k(\omega) = -i\omega\tilde{m}v_{phs}^{P}(\omega)\left(1+\frac{i}{2Q_{seis}^{P}(\omega)}\right) \tag{B.4.3}$$

$$Z_{seis}^{S}(\omega) = -iM^{S}k(\omega) = -i\omega\tilde{m}v_{phs}^{S}(\omega)\left(1+\frac{i}{2Q_{seis}^{S}(\omega)}\right) \tag{B.4.4}$$

As mentioned above, Q_{seis}^{P} and Q_{seis}^{S} generally exceed 30, and phase velocities are approximately frequency-independent, so:

$$Z_{seis}^{P} \cong -i\omega\tilde{m}v_{phs}^{P} \tag{B.4.5}$$

$$Z_{seis}^{S} \cong -i\omega\tilde{m}v_{phs}^{S} \tag{B.4.6}$$

$$R_{seis}^{P} \cong \frac{\tilde{m}_2 v_{phs,2}^{P} - \tilde{m}_1 v_{phs,1}^{P}}{\tilde{m}_2 v_{phs,2}^{P} + \tilde{m}_1 v_{phs,1}^{P}} \tag{B.4.7}$$

$$R_{seis}^{S} \cong \frac{\tilde{m}_2 v_{phs,2}^{S} - \tilde{m}_1 v_{phs,1}^{S}}{\tilde{m}_2 v_{phs,2}^{S} + \tilde{m}_1 v_{phs,1}^{S}} \tag{B.4.8}$$

which is real-valued and independent of frequency. Please note that this definition of impedance differs from the definition customary in the seismic literature by the factor $-i\omega$. However, as we see in Equations (B.4.7) and (B.4.8), above, this does not affect the reflection coefficients.

In the EM case, following Harrington (2001) for plane wave characteristic (intrinsic) impedance, and specializing to low-frequency dispersion using Equation (B.2.2):

$$Z_{EM}(\omega) \cong \rho k^{*}{}_{EM}(\omega) = \sqrt{\frac{\omega\mu_0\rho}{2}}(1+i) \tag{B.4.9}$$

$$R_{EM} \cong \frac{\sqrt{\rho_2} - \sqrt{\rho_1}}{\sqrt{\rho_2} + \sqrt{\rho_1}} \tag{B.4.10}$$

which is also real-valued and independent of frequency.

In the seismic case, borrowing from Mavko *et al.* (2011), rock impedances vary between that of poorly consolidated sandstone (min. 4.89e6 kg/m^{2}s) and that of limestone (max. 1.43e7 kg/m^{2}s). Seismic processing is designed to handle the relatively small (10%) reflection coefficients typical in sandstone/shale sequences; however, processing can be problematic when limestone, salt, or basalt produce reflection coefficients as high as 0.95 in magnitude. Seismic reflectivity is, in principle, frequency-dependent as well, because of the multiple reflecting layers lying close together in the subsurface.

For EM, we are looking for anomalously high resistivity contrasts associated with hydrocarbons, so high EM reflection coefficients are prospective. The contrast between resistivity in a typical shale (1 Ωm) and a typical sandstone with porosity containing a desirable oil fraction (perhaps 100 Ωm) produces an 82% reflection coefficient. However, in a typical sedimentary basin, problematic EM reflection coefficients of the same or greater size can also be produced by fresh water lenses, coal seams, limestones, and basalt intrusions. EM reflectivity is frequency-independent, unless these problematic lithologies occur in problematic geometries.

B.5 Critical angles

Snell's Law and the critical angle θ_{crit} are expressed in terms of a layer's index of refraction n_i or wavenumber k_i:

$$\frac{\sin(\theta_1)}{\sin(\theta_2)} = \frac{n_2(\omega)}{n_1(\omega)} = \frac{k_2(\omega)}{k_1(\omega)} \tag{B.5.1}$$

$$\theta_{crit}(\omega) = \sin^{-1}\left(\frac{n_2(\omega)}{n_1(\omega)}\right) = \sin^{-1}\left(\frac{k_2(\omega)}{k_1(\omega)}\right) \quad \text{(B.5.2)}$$

Citing Mavko *et al.* (2011), P-wave phase velocities vary between that of poorly consolidated sandstone (min. 2.43 km/s) and that of limestone (max. 5.79 km/s), so critical angles will seldom be less than 25°, and are usually much larger. For EM, allowing resistivity to vary by 2 orders of magnitude (as in the modeling below) produces a critical angle of 7°. Consequently, critically and post-critically refracted waves are much more likely in EM than in seismology.

13 Appendix C

C.1 Lateral waves and T-equivalence

It is well-accepted in the CSEM community that, from the point of view of surface receivers, deep reflectors appear like horizontal resistive sheets (Constable and Weiss (2006)). Reflection amplitudes associated with these sheets are governed by T, defined as reflector layer thickness multiplied by reflector resistivity. This can be viewed as confirmation that angles of incidence are beyond critical, and we are observing lateral wave behavior.

Swidinsky and Edwards (2009) show that T-equivalence is a natural theoretical consequence for 2-D boundary conditions. The authors consider a layer of thickness Δ and conductivity σ, with upper and lower surface depths d_1 and d_2, respectively. The authors make a first-order Taylor approximation (in Δ) for the change in electric and magnetic field components from depth d_1 to d_2. They then insert implied expressions for the field derivatives with respect to depth into Maxwell's equations for TE sources (where the vertical electric field component is zero) and for TM sources (where the vertical magnetic field component is zero). For the present TM case, the authors produce the following boundary conditions in terms of E and H (*cf.* Appendix A.1) (using our sign convention):

$$
\begin{aligned}
&H_y\big|_{d_2} = H_y\big|_{d_1} - S\,E_x\big|_{d_1} \\
&H_x = H_z = 0 \\
&E_x\big|_{d_2} = E_x\big|_{d_1} + i\omega\mu_0\Delta\,H_y\big|_{d_1} + T\left.\frac{\partial^2 H_y}{\partial x^2}\right|_{d_1} \\
&E_z\big|_{d_2} = E_z\big|_{d_1} + T\left.\frac{\partial^2 H_y}{\partial x \partial z}\right|_{d_1} \\
&E_y = 0
\end{aligned}
\qquad \text{(C.1.1)}
$$

where S and T are defined by:

$$S \equiv \sigma\Delta$$
$$T \equiv \frac{\Delta}{\sigma} = \rho\Delta \tag{C.1.2}$$

The authors argue that, for a thin resistive sheet, ($S \to 0$), and for skin depth large compared with the source-receiver separation ($\omega\mu_0\Delta \ll T/L^2$ where L is the source-receiver separation) the TM boundary conditions simplify to:

$$H_y\big|_{d_2} = H_y\big|_{d_1}$$
$$E_x\big|_{d_2} = E_x\big|_{d_1} + T\left.\frac{\partial^2 H_y}{\partial x^2}\right|_{d_1} \tag{C.1.3}$$
$$E_z\big|_{d_2} = E_z\big|_{d_1} + T\left.\frac{\partial^2 H_y}{\partial x \partial z}\right|_{d_1}$$

The authors conclude, since Equation (C.1.3) contains only the product $T = \rho\Delta$, that the TM mode boundary conditions are consistent with T-equivalence. Other experiments, *e.g.* with receiver not polarized inline with receiver dipoles, would lead to different conclusions.

How does this relate to the 1-D "lateral" waves in this thesis? In the present TM case $E_x = 0$ at critical incidence angles and beyond; hence, E_z is governed by its T-equivalent boundary condition in Equation (C.1.3).

C.2 Numerical evidence of linear lateral wave moveout

A frequency-domain implementation of 1D diffusion code called "WHAM" is freely available on the website of Marine EM laboratory at Scripps Institution of Oceanography http://marineemlab.ucsd.edu . Like the MATLAB code used to generate Sections 2.4 and 2.5 time-domain simulations, the WHAM code follows Key (2009). The time-domain MATLAB

solutions are assembled via Fourier superposition of 60 frequency-domain solutions over 4 decades of frequency running from 0.01 Hz to 100 Hz. Note that when the solutions are within numerical noise, their contribution is set to zero.

In this section, WHAM frequency-domain solutions generated at the five decade frequencies are examined for evidence supporting the importance of critically-incident waves travelling laterally at the phase velocity of the higher resistivity medium at the ocean-sediment, sediment-reservoir, and air-ocean interfaces. Positive evidence is presented by overlaying lines with slopes appropriate to the three phase gradients onto plots of phase versus offset in these simulations (Table C.2.1).

$$\frac{360\,f}{v_{phs}(f)}\ (°/\text{km})$$

Decade frequencies (Hz)	Sediment	Reservoir			Air*
@ resistivity (Ωm) →	1	50	100	125	very high
0.01 Hz	11.38	1.61	1.14	1.02	~flat
0.1 Hz	36.00	5.09	3.60	3.22	~flat
1 Hz	113.84	16.10	11.40	10.18	~flat
10 Hz	360.00	50.91	36.00	32.20	~flat
100 Hz	1138.42	161.00	113.84	101.82	~flat

Table C.2.1: Phase gradient of critically-incident waves travelling laterally at three interfaces (note that the phase of the air wave should not depend on frequency).*

Figures C.2.1 through C.2.5 show the WHAM phase plots with these phase gradients overlaid. Note that the plots are of field components produced for the Canonical Model for offsets to 20 km. For our purposes, this important component is the red Inline E field. The overlaid slopes are quite close in the 0.01 Hz, 0.1 Hz, and 1 Hz plots suggesting that for short

offsets the sediment lateral wave dominates, for medium offsets the reservoir lateral wave dominates, and for long offsets the air lateral wave dominates. That they are not exact may indicate the influence of post-critical incidence angles and of finite layer thicknesses. In the 10 Hz plot, the sediment lateral wave is confirmed but the scale on the WHAM plot does not go high enough to see the other two lateral waves. In the 100 Hz plot, numerical noise appears to dominate; curiously, at far offsets there is the suggestion of a flat air lateral wave section.

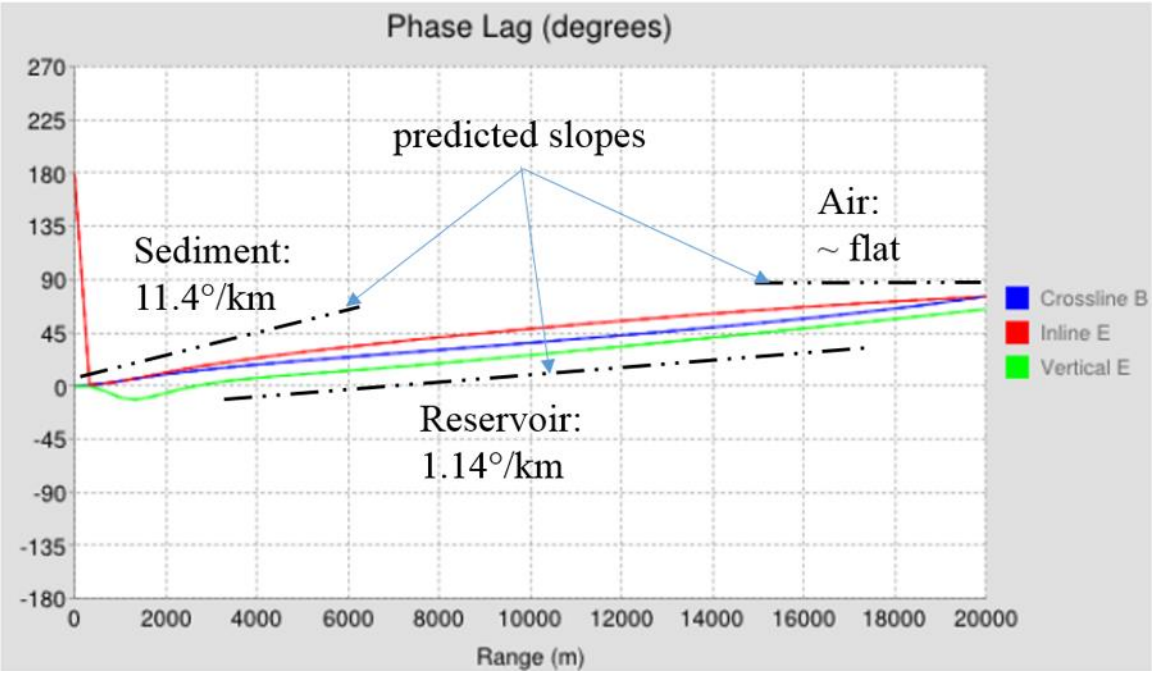

Figure C.2.1: WHAM offset gradient of electric field phase for Canonical Model at 0.01 Hz [note that the left axis is the phase lag in degrees].

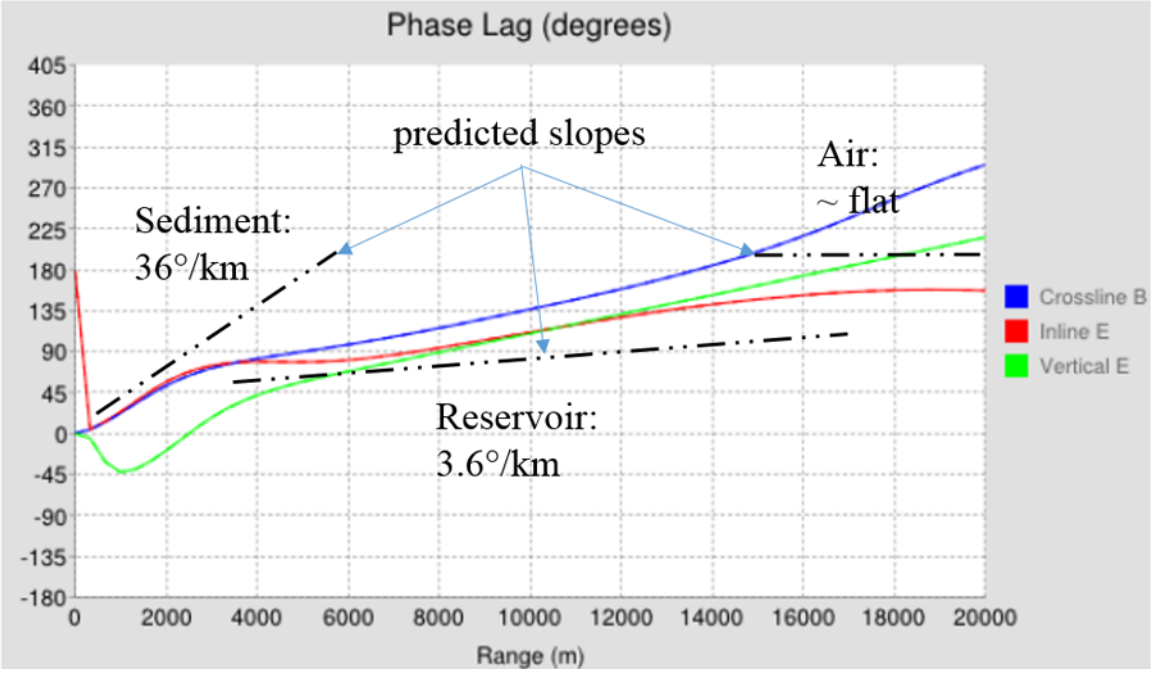

Figure C.2.2: WHAM offset gradient of electric field phase for Canonical Model at 0.1 Hz [note that the left axis is the phase lag in degrees].

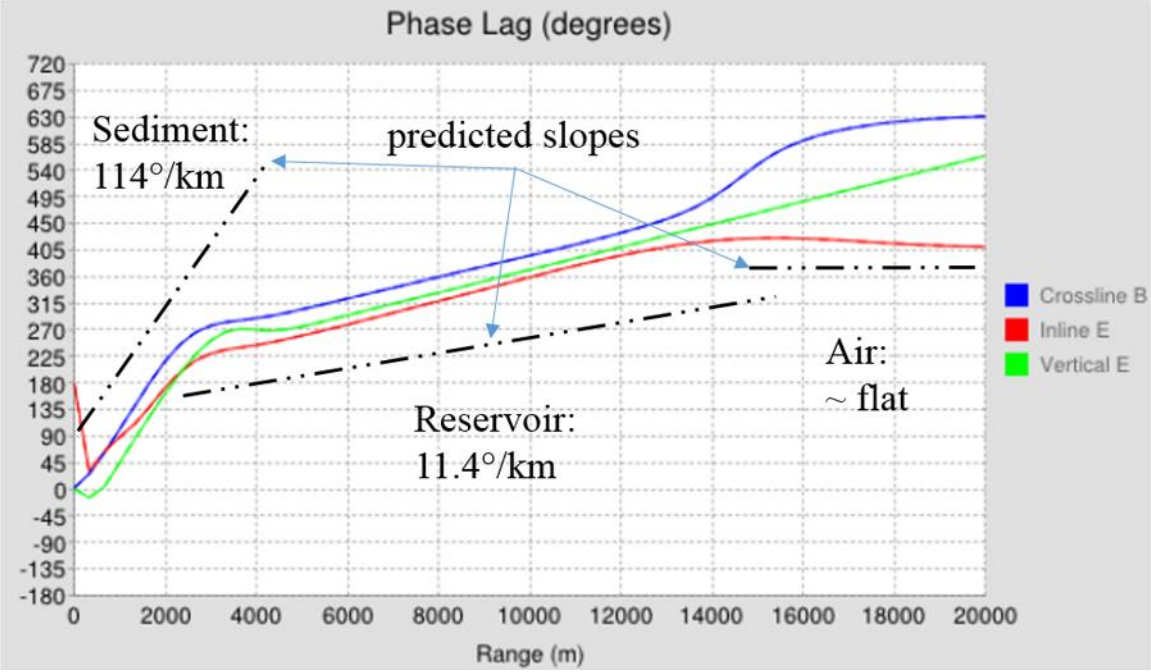

Figure C.2.3: WHAM offset gradient of electric field phase for Canonical Model at 1 Hz [note that the left axis is the phase lag in degrees].

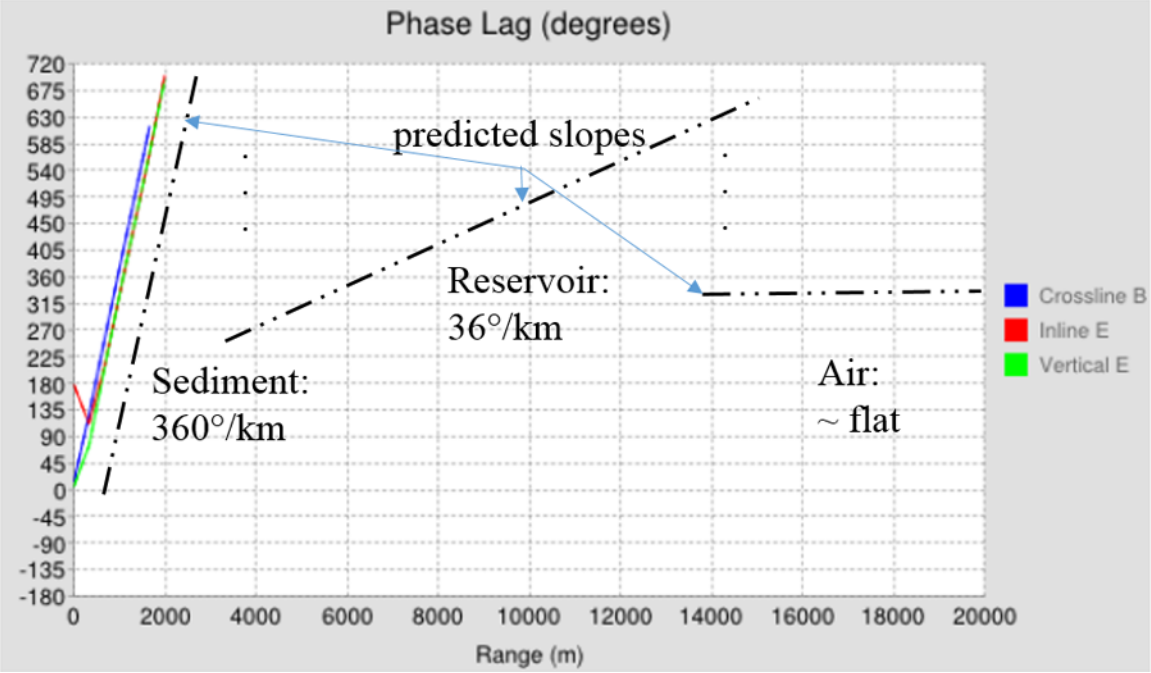

Figure C.2.4: WHAM offset gradient of electric field phase for Canonical Model at 10 Hz [note that the left axis is the phase lag in degrees].

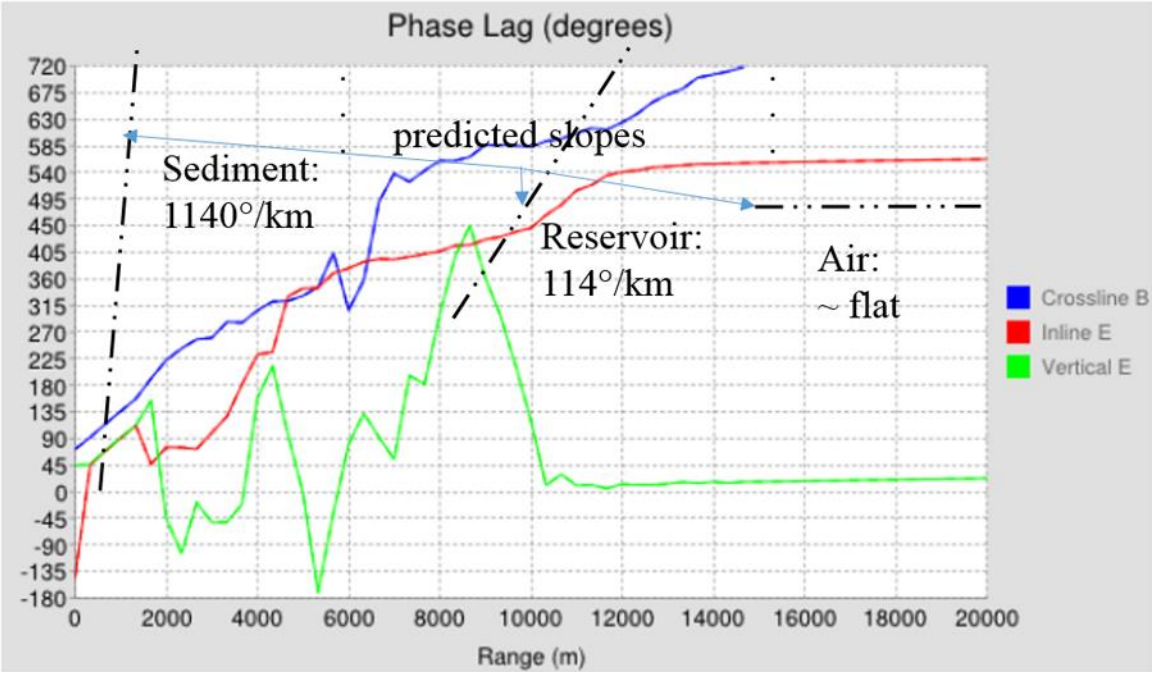

Figure C.2.5: WHAM offset gradient of electric field phase for Canonical Model at 100 Hz [note that the left axis is the phase lag in degrees].

C.3 Numerical evidence of linear moveout with T-equivalence

WHAM comparison plots are presented for the T-equivalent models from Section 8 where T is held constant at 10,000 Ωm^2. As in the preceding section, lines with critical angle lateral wave phase slope gradients are overlaid on plots of phase versus offset for single-frequency model simulations. Here, we focus on simulations at 1 Hz.

Figure C.3.1 compares the Canonical Model, where ρ is 100 Ωm, Δd is 100 m, and the reservoir lies from 1 km to 1.1 km below the seabed, to a T-equivalent model, where ρ is 50 Ωm, Δd is 200 m, and the reservoir lies from 1 km to 1.2 km below the seabed. For both models, the pure 50 Ωm reservoir lateral wave phase slope gradient is closer to that observed in the simulations than that for the pure 100 Ωm reservoir lateral wave.

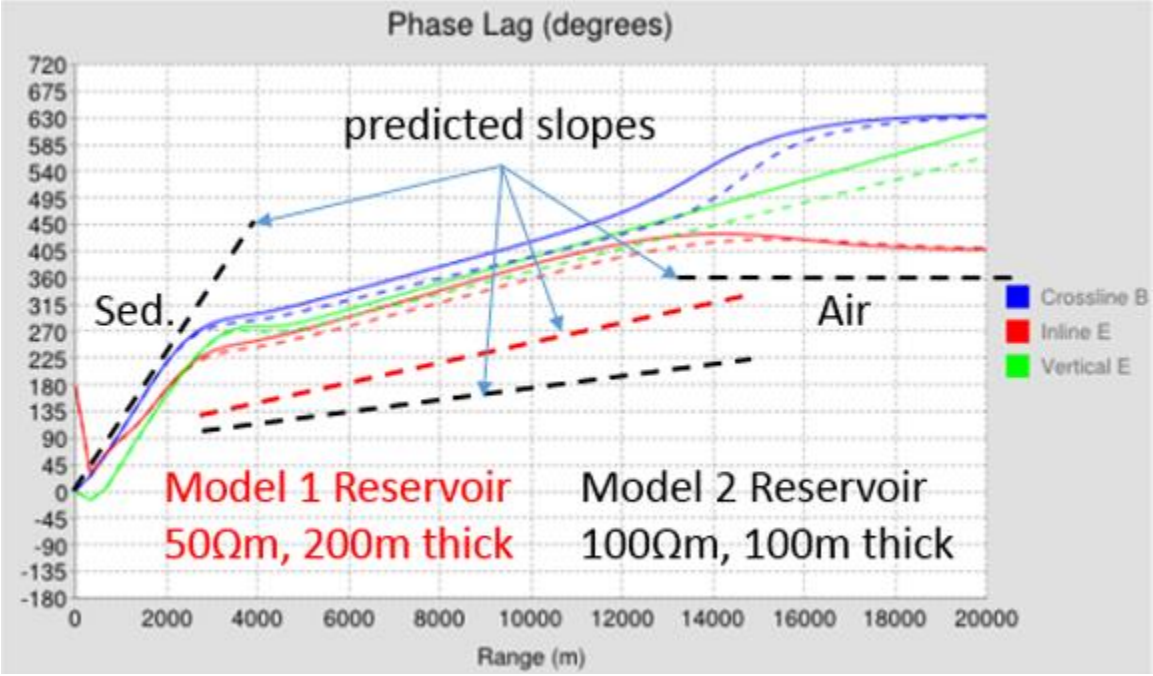

Figure C.3.1: WHAM 1 Hz offset gradient of electric field phase for Canonical Model and T-equivalent model with 50 Ωm, 200 m thickness, and the reservoir lies from 1 km to 1.2 km below the seabed [note that the left axis is the phase lag in degrees].

Figure C.3.2 compares the Canonical Model to a T-equivalent model where ρ is 125 Ωm, Δd is 80 m, and the reservoir lies from 1 km to 1.08 km below the seabed. In this case, neither the pure 100 Ωm reservoir lateral wave phase slope gradient nor that for the pure 125 Ωm reservoir lateral wave is closer to that observed in the simulations.

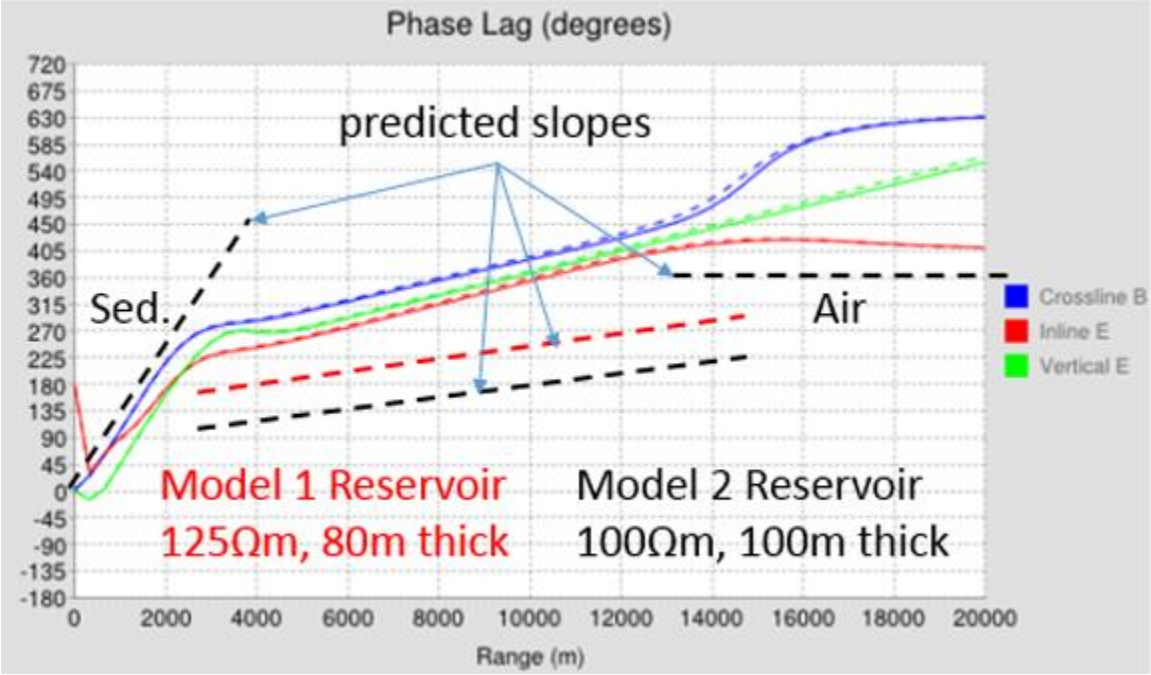

Figure C.3.2: WHAM 1 Hz offset gradient of electric field phase for Canonical Model and T-equivalent model with 125 Ωm, 80 m thickness, and the reservoir lies from 1 km to 1.2 km below the seabed [note that the left axis is the phase lag in degrees].

While the T-equivalent models are remarkably similar, they are not identical, and their subtle differences may yield clues to differentiating between them.

14 Appendix D

D.1 Radon transform sampling considerations

Our temporal sampling at 2 ms produces a 250 Hz Nyquist frequency. This would appear to be overkill given the rapid loss of frequency content with depth.

Our spatial sampling at 50 m produces a 100 m Nyquist wavelength. This corresponds to a 1 km/s phase velocity at 10 Hz, and a 1 m/s phase velocity at .01 Hz. Again, this seems more than adequate for this problem.

The reader may be less familiar with requirements to avoid aliasing in the $\tau - p$ transform. Turner (1990) points out that insufficient spatial sampling causes events to plot at multiple p values in the $\tau - p$ domain, dependent on temporal frequency.

In order to allow unaliased reconstruction with the range of slants, for time-domain processing (Turner, 1990):

$$\Delta p < \frac{1}{x_r f_{\max}} \tag{D.1.1}$$

where Δp is the p spacing, x_r is the range of offset values, and $f_{\max} \leq f_{Nyquist}$. Thus, in our EM case, taking effective $f_{\max}$ to be 10 Hz, the p spacing must be less than 0.01 s/km.

In this context, spatial aliasing refers to the multiple p values that can be attributed to a signal due to insufficient sampling. In order to avoid this problem (Turner, 1990):

$$\Delta x \leq \frac{1}{p_r f_{\max}} \rightarrow p_r \leq \frac{1}{\Delta x f_{\max}} \tag{D.1.2}$$

where p_r is the range of slowness chosen. In our case, p_r must be less than 2 s/km.

D.2 EM-Radon transform sampling considerations

The Turner (1990) anti-aliasing criteria for p, for EM data can be recast in terms of resistivity. Equation (D.1.1) becomes:

$$\delta\sqrt{\frac{1}{\rho}} < \sqrt{\frac{4\pi}{\mu_0}}\frac{1}{x_r\sqrt{f_{\max}}} \tag{D.2.1}$$

and (D.1.2) becomes:

$$\left(\sqrt{\frac{1}{\rho}}\right)_r \le \sqrt{\frac{4\pi}{\mu_0}}\frac{1}{\Delta x\sqrt{f_{\max}}} \tag{D.2.2}$$

Inverting and squaring, we have, respectively:

$$\delta\rho > \frac{\mu_0 x_r^{\,2} f_{\max}}{4\pi} \tag{D.2.3}$$

$$\rho_r \ge \frac{\mu_0 (\Delta x)^2 f_{\max}}{4\pi} \tag{D.2.4}$$

In our case, for $f_{\max}$ = 10 Hz, $\delta\rho$ must exceed 100 Ωm, and ρ_r must be equal to or greater than 0.00025 Ωm. The requirement on ρ_r is not restrictive, but using the current parameters, there is little resolution between resistivity at 60 Ωm and 256 Ωm. This issue represents an opportunity for further study.